Design and Experimental Studies of a Nanofluid Direct Absorption Solar Collector

by
Lisbeth Espedal

Master of Science in Process Technology
Specialisation in Multiphase Systems

Department of Physics and Technology
University of Bergen

June 2020

Abstract

Utilising solar energy could be an essential contribution to the Earth's rising demand for sustainable energy sources. However, conventional solar collectors are limited by low heat conversion efficiency, which makes the use of solar energy expensive and challenging. Numerous studies conducted in the last decade show that nanoparticles can enhance the optical and thermophysical properties of working fluids in solar collectors. These findings have led to the development of a more promising and competitive device called a Direct Absorption Solar Collector (DASC).

There is still a shortage of larger-scaled experimental studies concerning nanofluid DASCs. In this thesis, the principle of volumetric absorption is therefore studied by proposing and constructing a DASC setup suited for the utilisation of nanofluids. The performance of the DASC was investigated with 0.05wt.% carbon black nanofluid by varying flow rate and tilt angle of the collector in the field of gravity.

The volumetric heat generation efficiency of the nanofluid DASC increased with rising flow rates through the system. The collector also achieved the highest efficiency when oriented with a 0° tilt angle. This can be credited to the enhanced Rayleigh Bérnard convection effects within the nanofluid. Contrary to previous empirical data, the DASC achieved higher efficiency with water as working fluid compared to the nanofluid in all cases. This was credited to a insufficient particle concentration in the nanofluid due to particle deposition in the system, as well as nanofluid instability. Additionally, difficulties with leakages and bubbles in the DASC were experienced. These issues were more prominent during the DASC experiments with nanofluid, than for the water. Thus, the efficiency of the nanofluid DASC is expected to be higher in real life conditions than what was achieved in these experiments.

SLS analysis revealed that multiple batches of the same nanofluid can be mixed and still maintain an excellent level of stability. However, repeated heating showed to have a destructive effect on nanofluid stability, due to destabilisation of the SDS surfactant at DASC operating temperatures (~ 52°C). Finally, the generation of foam in the nanofluid was experienced, and a solution to this issue was proposed and tested. The results from this study, both expected and unexpected, underscores the importance of practical studies of the utilisation of nanofluids in DASCs.

Acknowledgments

First and foremost, I offer my sincerest gratitude to my supervisors Prof. Pawel Kosinski and Prof. Boris V. Balakin for their help, guidance, and feedback throughout my master thesis.

I would like to thank Engineer Charles Sebastiampillai and his colleagues at the mechanical workshop at the Department of Physics and Technology. Their help and expertise in developing and constructing the experimental setup have been crucial. Halvard Thon also deserves recognition for his help with the Malvern Mastersizer 2000 and general guidance in thesis writing. I would also show my gratitude to OCTIO AS / Gravitude AS for letting me continue my experiments at their office while the university campus was temporarily closed down.

My most profound appreciation goes to my boyfriend, Andreas Fosso Dale, for the help and support throughout this period. I would also like to express my heartfelt gratitude to my father, Trond Arne Espedal, for his genuine interest and invaluable guidance in this project. Last but equally important, I would like to thank the rest of my family and friends for their love and patience. A special thanks goes to Runa By Bardsgård, Marthe Braut, Ivar Ravndal, and the rest of my fellow master students in the 'multiphase'-office for making my last year of studies memorable.

Nomenclature

Abbreviations

CB Carbon Black

CFD Computational Fluid Dynamics

DASC Direct Absorption Solar Collector

EG Ethylene Glycol

HVL Western Norway University of Applied Sciences

IEA International Energy Agency

IR Infrared

NF Nanofluid

NP Nanoparticle

PMMA Polymetylmetakrylat

PSD Particle Size Distribution

PTFE Polytetrafluoroethylene

SC Surface collector

SD Standard Deviation

SDBS Sodium Eodecylbenzene Sulfonate

SDS Sodium Dodecyl Sulfate

SEM Scanning Electron Microscope

SLS Static Light Scattering

STE Solar Thermal Energy

TEM Transmission Electron Microscopy

UiB University of Bergen

UV Ultraviolet

Greek Letters

α	Volume Fraction	
δ_t	Thickness of thermal boundary layer	[m]
η	Efficiency	
λ	Wavelength	[m]
μ	Dynamic viscosity	[Pa·s]
ρ	Density	[kg/m^3]

Latin Letters

$\dot{m}$	Mass flow	[kg/s]
$\dot{Q}$	Heat	[J/s]
c	Molar concentration	[mol/L]
c_p	Specific heat	[J/kg·K]
h	Coefficient of heat transfer	[W/m^2·K]
I	Radiative heat flux	[W/m^2]
k_c	Thermal conductivity	[W/m·K]
l	Length or thickness	[m]
m	Mass	[kg]
Nu	Nusselt number	
p	Pressure	[Pa]
Pr	Prandtl number	
Q	Volumetric flow rate	[m^3/s]
R	Thermal resistance	[K·m/W]
Re	Reynolds number	
S	Area	[m^2]
T	Temperature	[K,°C]
u	Velocity	[m/s]
x, y, z	Spatial coordinates	[m]

Physical constants

σ	Stefan-Boltzmann constant	$5.670367 \cdot 10^{-8}$ [W/m^2·K^4]

Subscripts

abs	Absorbed
c	Continuous phase
co	Conduction
cv	Convection
d	Dispersed phase
$emit$	Emitted
$H.Ex$	Heat exchanger
p	Constant pressure
rad	Radiation

Table of Contents

List of Figures

List of Tables

Chapter 1

Introduction

1.1 Motivation

One of the great contemporary global challenges is the pursuit to cover the world's growing energy demand while also reducing the environmental impact of current and future growth. The world energy demand surged by a historically high value of 2.3% in 2018, and the International Energy Agency (IEA) [1] predicts that it will continue to increase annually by 1.3% until 2040. Climate issues have received growing attention, and in March 2019, over a million students from 125 countries [2], organised in *School strike for the climate* where they protested against decades of passivity from political leaders towards the ever-growing menace of global warming.

Increased focus on the dangers of climate change combined with ever-increasing scrutinisation towards politicians has in recent years started to yield results. Ambitious goals to adapt to existing problems caused by climate change, but also to combat further climate degradation, permeates the contemporary political discourse. One such effort is The Paris Agreement [3], which is the first universal, legally binding global climate change protocol. It aims to strengthen the coordinated response to the threat of climate change by limiting the long-term rise in global average temperature to 'well below 2°C ... and pursuing efforts to limit [it] to 1.5°C'. Conversely, the pending climate conference in Glasgow 2021 is set to renew the goals of the 2015 Paris conference, while further restricting the current climate gas emissions.

The rising demand in both advanced- and emerging market economies for energy services presents a historic opportunity to introduce new sustainable solutions to future and contemporary dilemmas. Fast-growing populations and accelerated economic expansion are strongly linked to high production rates and corresponding use of energy [4], [5]. Almost 2 billion people, or a third of the world's population, lack access to adequate, affordable, clean, and convenient energy services such as electricity [6], [7]. A significant number of those people exclusively depends on solid- or fossil fuels for cooking and heating. Under combustion, solid- and fossil fuels may emit both greenhouse gases and air pollutants, such as carbon dioxide and sulfur oxides. These are harmful to both local public health and the

global environment. If renewable energy, energy efficiency, and clean conventional technologies becomes more widely available, benefits can be harvested in the form of economic and social development, as well as for future environmental protection. The development of new energy technology and progress in terms of efficiency of already existing green technology is therefore paramount to the green transformation.

For the time being, solar irradiation is one of the most promising source of permanent and inexhaustible energy supply. Massive quantities of solar energy are generated at and diffused in all directions in space from the surface of the Sun. An estimated peak of $1.3843 \cdot 10^{16}$ kWh solar irradiation intercepts on the Earth surface annually, a quantity that is over three times larger than the sum of the total global energy consumption [7]. Whilst we cannot utilise the Sun's full potential, it remains the most promising source of energy to date. Figure 1.1 shows a forecast by the IEA of the world energy consumption by source; the most prominent feature being the unmistakable spike in projected utilisation of solar energy.

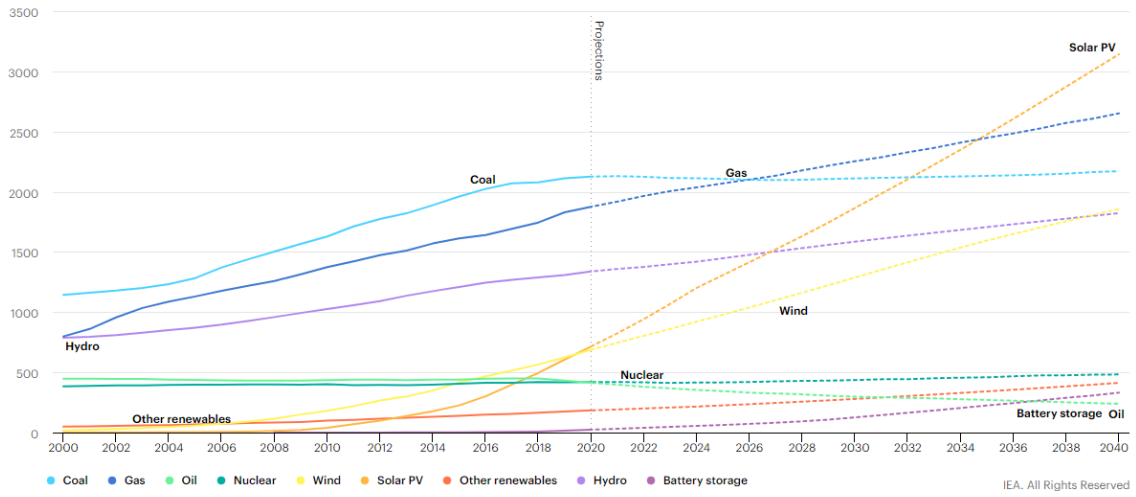

Figure 1.1: Forecast of world energy consumption by source, year 2000 to 2040 [8].

Presently, the two primary methods of harnessing and utilising solar energy are: (i) solar photovoltaic cells (SPV), and (ii) solar thermal energy (STE). The first, and currently most abundant of the two, SPV, or solar cells, are made of semiconductor materials and can be found in a variety of applications such as satellites, portable power supplies, and remote illumination systems. When incident photons (sunlight) strikes a solar cell, the electrons in the cell becomes agitated to a point where they break away from its atom and move freely. As the free electrons flow through the cell, they constitute an electrical current. A substantial benefit of SPV's is that they produce electricity directly, thus eliminating intermediate steps which cause energy loss, such as heat-transfer fluids and steam-turbines. The most pressing issue for commercial SPV systems is their indisputable low efficiency which is limited by two significant factors. Primarily, their electrical resistance that grows with their temperature. Secondly, current solar cells are only capable of utilising a small portion of the incoming solar spectrum. Due to the reasons mentioned above, the solar cells

are only capable of converting up to 30% of the available solar energy into useful electricity [9]. Other critical drawbacks of the SPV systems are the costly production process and the problematic recycling process at the end of their lifetime due to the utilisation of toxic metals such as lead and cadmium.

STE technology, on the other hand, relies mainly on indirect absorption of the incoming thermal radiation from the Sun. Conventional solar thermal collectors, such as flat-plate collectors and evacuated tube collectors, utilise a selective surface absorber with favourable characteristics such as high solar absorbance and low thermal emittance [10]. As incoming sunlight hits the surface absorber, the carrier fluid is heated through thermal energy convection and conduction. STE power plants employ various techniques to harvest the Sun's energy into heat sources, such as hot water or steam to drive turbines generating electricity. Concurrently, commercial SPV technology is a solid competitor to the solar concentrator plants whose efficiency is around 30%, but the capital cost is somewhat higher.

A critical factor that limits the efficiency of a conventional solar collector is the high temperature of the surface absorber in comparison to the carrier fluid. A promising alternative design was proposed in 1975 by Minardi and Chuang [11]. Their idea was to simplify the current versions of solar thermal collectors and to increase the efficiency through direct capture of sunlight by the fluid volume, which serves both as a solar energy absorber and heat carrier (volumetric absorption). The novel solar collector design is recognised as the predecessor to what later became the concept of a direct absorption solar collector (DASC), which is illustrated in Figure 1.2. The volumetric absorption approach in DASC is very beneficial when harnessing solar energy because a uniform temperature distribution within the working fluid is created. Consequently, the detrimental overheating of the surface is eliminated. Thus, the thermal loss from the collector to the surroundings is reduced significantly [10], [12].

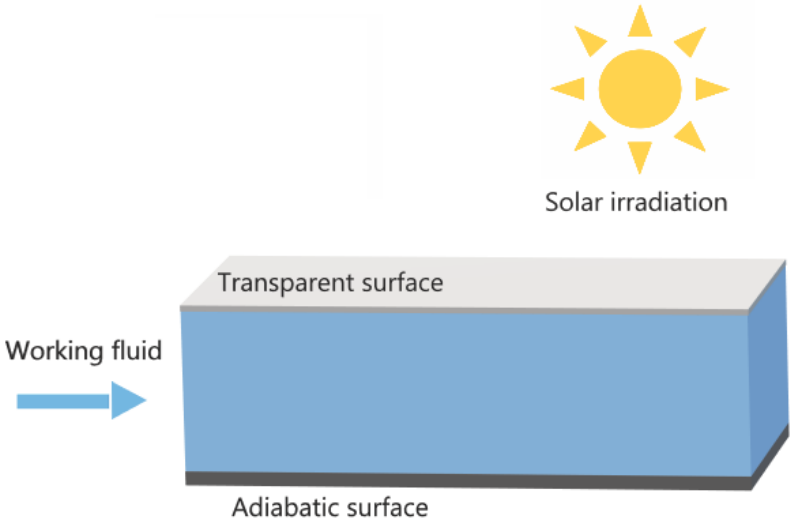

Figure 1.2: Schematic of a direct absorption solar collector.

Nanofluids (NF) is a novel type of heat transfer fluids containing stable suspended nano-sized particles in a base fluid such as water. The dispersed nanoparticles (NP) exhibit high absorption capability for solar radiation, as well as high thermal conductivity [13], [14]. Compared to conventional working fluids, the optical and thermal properties of a nanofluid has the potential to enhance the heat transfer process significantly and thus the performance of a solar collector. Figure 1.3 illustrates the difference in thermal resistance between a surface absorber and a nanofluid DASC. The latter has a higher thermal efficiency due to the elimination of thermal resistance between the working fluid and surface absorber: $R'_{abs} < R_{abs} + (R_{co} + R_{cv})$. R_{co} and R_{cv} represents the energy conversion resistance between the surface absorber and the working fluid for a surface solar collector. There is a great deal of research concerning the subject of enhanced flat-plate solar collectors, and several experimental studies show that efficiency can be improved by as much as $\sim$ 20-55% by adding nanoparticles to the working fluid [15]–[17]. A nanofluid DASC, however, is found to further enhance the efficiency by 10%, compared to the efficiency of a nanofluid flat-plate collector [18], [19].

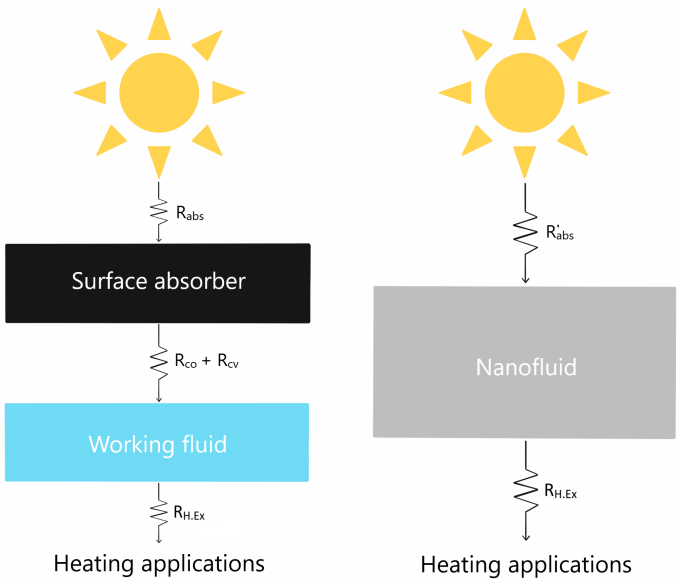

Figure 1.3: Thermal resistance of a surface solar collector compared to a nanofluid DASC. R_i is the thermal resistance by i at each step. Inspired by Taylor et al. [20]

Even though the topic of nanofluids has become widely investigated in theory, there is still a need for more larger-scaled experimental research of the applicability of nanofluids in DASCs before potential commercialisation is possible. The anticipated increase in efficiency must be further validated before it can compete against conventional technology in the global market. In this study, the goal is to consider the concept of a DASC with nanofluid for capturing and storing solar energy. The objective is to investigate the efficiency of the DASC with varying parameters. The results are also compared to the performance of water in the same DASC design, as well as with a surface collector (SC).

1.2 Literature review

In this section, some contemporary research concerning the utilisation of nanofluids in a DASCs is presented. Additionally, relevant work on DASC parameter optimisation and carbon black nanofluid properties is reviewed.

The aforementioned work by Minardi and Chuang [11] was pioneering when it came to the utilisation of nanofluids in solar collectors. They created a "black" liquid flat-plate solar collector where the incoming solar radiation was absorbed directly by the liquid flowing through transparent channels. They proposed that the central agent for success was the black liquid itself. Several types of particles were considered as a possible addition to the working liquid, such as carbon black and antimony sulphide (Sb_2S_3), due to favourable particle characteristics in terms of absorptivity, emissivity, chemical stability, and cost. They concluded that their newly developed solar collector showed promising results in comparison to the performance of conventional types of flat-plate solar collectors.

Otanicar et al. [21] investigated, through experimental and numerical analysis, how the performance of a micro-scale DASC is affected when adding various nanoparticles (carbon nanotubes, graphite, and silver) to water. Figure 1.4 shows the variation of steady-state DASC efficiency with the nanoparticle volume fraction for different materials. During the nanoparticle experiments, a reflective aluminium tape coated the bottom surface of the solar collector. Two experiments with pure water were also conducted for comparison: one with reflective aluminium tape on the collector bottom surface, and one with matte black paint. The matte black paint resulted in a significantly higher efficiency for the solar collector, compared to the reflective bottom surface. This can be seen in Figure 1.4. Moreover, the experimental and numerical results for the nanofluid showed that the solar collector efficiency rapidly increased when adding small quantities of nanoparticles to the pure base fluid. However, when the volume fraction reached approximately 0.5%, the efficiency started to level off and even slightly decrease with continual increases in the volume fraction of nanoparticles. Finally, Otanicar et al. found that the most significant difference in steady-state efficiency for the nanofluids occurs when halving the size of silver nanoparticles from 40 to 20 nm, where they observed a 6% efficiency improvement.

Filho et al. [22] studied the effect of using silver/water nanofluid in a DASC located under direct sunlight on a rooftop. The nanofluid was prepared in a high-pressure homogenizer before the experiments, to advance the suspension stability. Their results show that the silver nanoparticles have excellent photothermal conversion capability, even at exceedingly low concentrations, and that nanofluid DASCs can achieve significantly higher bulk temperature compared to other working fluids such as water. At the peak temperature, they also observed an enhancement in stored thermal energy by 52%, 93% and 144% for a particle concentration of 1.62, 3.25 and 6.5 ppm, respectively.

An experimental and numerical study of nanofluid optical properties by Taylor et al. [19] highlights the importance of carefully choosing and preparing a nanofluid for a specific application. If the concentration of nanoparticles is very high, a thin surface layer might absorb all the incoming radiation. This reduces the collector efficiency since more thermal energy is lost to the surroundings. On the other hand, an insufficient concentration is

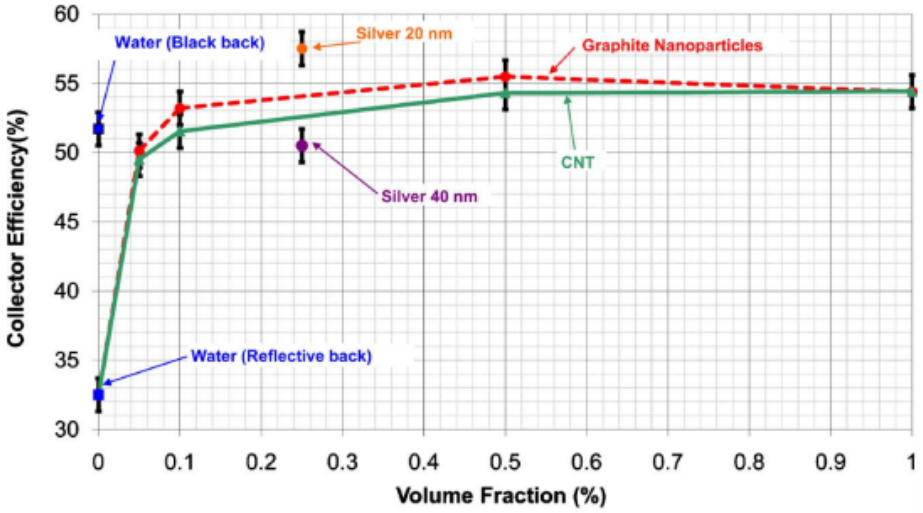

Figure 1.4: Experimental efficiency results for the steady-state microsolar thermal collector [21].

not capable of absorbing all the incoming radiation. As a result, the optical properties of the nanofluid must be carefully regulated when the aim is to enhance a solar collector. Their article also reveals that absorption of radiation is mainly caused by the nanoparticles at shorter wavelengths, and by the base fluid at longer wavelengths. Furthermore, their results showed a 10% efficiency improvement, both theoretically and experimentally, when comparing a nanofluid-based solar thermal system to a conventional one. The main purpose of their research was to find potential nanofluid candidates that would increase the efficiency of a solar collector. Ultimately, they presented several nanofluids (graphite, aluminium, copper, silver and gold) that in a given volume fraction can be expected to absorb $> 95\%$ of all the standard solar spectrum at the Earth's surface for a 10 cm fluid depth/film thickness. Finally, they concluded that aluminium and graphite nanofluids are the most likely to be used in real direct absorption solar collectors, since their behaviour can be predicted accurately and that the pricing is somewhat more cost-effective compared to the other nanofluids.

In a study concerning carbon black photothermal properties, Han et al. [13] found that the temperature of CB nanofluids increased more quickly compared to pure water when subjected to the same irradiation over time. Figure 1.5a shows the temperatures of CB nanofluid for different concentrations and pure water as a function of the solar irradiation time, while Figure 1.5b shows the temperature enhancement of CB nanofluids to pure water at the same irradiation time. For instance, from Figure 1.5a, within 42 min, the 6.6 vol.% CB nanofluid temperature increased from 24.4°C to 38.4°C, while that of the pure water only increased to 31.2°C. It can be mentioned that a 6.6vol.% may be a too high concentration for most DASCs, where the nanofluids usually only have trace amounts of nanoparticles added. Moreover, Han et al. credited the enhanced solar energy absorption to excellent optical properties and high thermal conductivity of CB nanofluids. Addition-

ally, the results in both Figure 1.5a and 1.5b point to a strong correlation between higher temperatures and increasing nanoparticle volume fraction. As a result, Han et al. reasoned that the solar adsorption ability improved with the volume fraction in the experimental range.

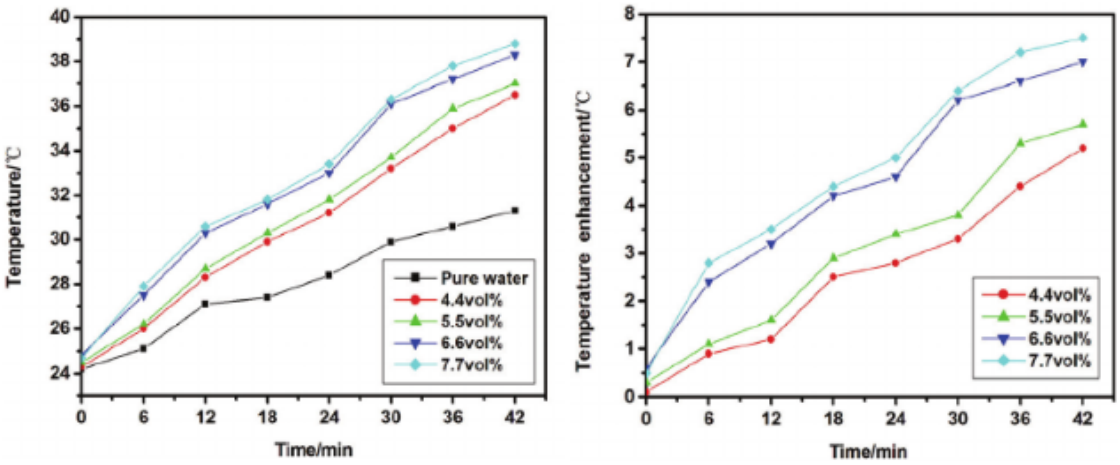

(a) Temperature as a function of time.

(b) Temperature enhancement as a function of time.

Figure 1.5: Photothermal properties of CB nanofluids [13].

Otanicar and Golden [23] evaluated the economic and environmental impacts of a nanofluid DASC in comparison to conventional solar collectors using the life-cycle assessment methodology. Their results showed that with the current cost of nanoparticles, the DASC had a somewhat prolonged payback period. However, at the end of its life-time, the DASC had the same economic saving as a conventional solar collector. A price drop is expected as nanoparticles become more widely used and produced, which should result in further savings with a nanofluid DASC. Finally, they concluded that a DASC offers a 9% lower embodied energy and a 3% higher pollution offset during its life-cycle compared to a conventional solar collector.

Tyagi and Phelan [18] theoretically investigated the practicality of using a DASC and compared its performance to that of a typical flat-plate collector. The absorbing medium was a nanofluid consisting of dispersed aluminium nanoparticles in water. They developed a method for a two-dimensional heat transfer analysis in which direct sunlight was incident on a thin flowing film of nanofluid. The energy balance equation and heat transfer equation were solved numerically to evaluate the temperature profile and intensity distribution within the nanofluid. Their results show that the presence of nanoparticles increases the absorption of incident radiation by more than nine times over that of pure water. The authors concluded that a nanofluid DASC could be expected to have up to 10% higher efficiency than that of a flat-plate collector under similar operating conditions.

Several experimental and numerical studies have been conducted to optimise the DASC design for maximising collector performance. Lenert and Wang [24] performed a combined modelling and experimental study to optimise the efficiency of a cylindrical liquid-based

volumetric solar collector. They found that the collector efficiency increased with increasing solar intensity and with nanofluid film thickness. Also, they advised that nanofluids with optimised properties could have significant potential as absorbers for concentrating solar power systems since the efficiency of such a system is anticipated to exceed 35% when coupled to a power conversion cycle. Further work within this field has been conducted by Sharaf et al. [25]. They investigated the subject of an optimal collector height in addition to the effect of different types of bottom surfaces. They found that regardless of particle loading and bottom surface type, DASCs with thinner nanofluid films always had lower efficiency compared to collectors with thicker nanofluid films. For relatively low particle loadings, the bottom surface type (reflective, transparent or absorptive) affected the DASC performance significantly. However, beyond a critical nanoparticle volume fraction, the performance became independent of its optical boundary characteristics since only a smaller amount of radiation reaches and interacts with the bottom surface. The critical value was found to be lower for a nanofluid film thickness of 10 mm than for a film thickness of 0.5 mm, which highlights the significant role of nanofluid optical properties on DASC performance.

An alternative DASC design, with V-shaped ribs on the bottom surface, was experimentally studied by Karami et al. [26]. This method of applying artificial roughness to the bottom surface sought to improve the DASC efficiency by altering the flow pattern inside the DASC. Their DASC design was also compared to the outdoor thermal performance of a conventional solar collector, both tilted at 35° to receive maximum solar energy. The energy and exergy efficiencies of graphene oxide nanofluid were found for varying nanoparticle volume fraction, flow rate and rib geometry (forward and backward rib). They concluded that utilising both the nanofluid and rib caused an enhancement in the energy and exergy performance. Finally, increasing the flow velocity was also found to enhance the effect of the ribs, thus increasing the collector efficiency.

Recently, a radiation and energic analysis of nanofluid based DASCs have been conducted numerically and validated experimentally by Eggers et al. [27]. They confirmed that volumetric absorption of radiation lowers the outer absorber temperature and thus reduces the thermal loss. Additionally, their study of flow velocities revealed that lower thermal loss could be achieved using a volumetric absorber. Usually, decreasing flow velocity is often associated with higher thermal loss. For this design, however, moderate flow velocities were beneficial for both absorption purposes, as well as for reducing the pressure loss and pumping power. In contrast, for a surface absorber system, the flow velocity must be high to cool the absorber wall from the inside, which reduces thermal loss to the surroundings. They observed that higher Reynolds numbers, and therefore increased turbulence, promote the equalisation of the temperature along the absorber cross-section while enhancing the heat transfer towards the wall. While higher Reynolds number gave slightly lower heat loss, the opposite resulted in the onset of layering of the temperature by natural convection effects in the surface absorber. Though, for the volumetric absorber, the fluid heated more homogeneously. Finally, a key result from their evaluation of simulated radiation field includes that a high nanoparticle volume fraction does not automatically improve the optical efficiency of a volumetric solar absorber. Whereas the radiation transmission

lowers the optical performance for small volume fractions of nanoparticles, scattering decays the performance at high volume fractions. As scattering has a significant impact on the optical efficiency of a solar thermal absorber, they stress that this effect must not be neglected, especially for realistic particle size distributions.

Balakin et al. [28] presented a Eulerian-Eulerian two-phase CFD-model of the cylindrical direct absorption solar collector with nanofluid, which is capable of reproducing motion and heat transfer in each separate phase (continuous and dispersed). They confirmed the model with two independent experimental datasheets from a third party, providing a satisfactory result. The authors altered the concentration and size of nanoparticles, as well as the geometry and inclination of the collector. By optimising DASC parameters, they were able to gain a 10% improvement in DASC efficiency. Furthermore, 30% increase in performance was noted when considering the process of thermomagnetic convection in the collector using a magnetic nanofluid. Another interesting observation is shown in Figure 1.6, where the collector efficiency is plotted against the angle between g and the collector centreline. The plot shows that the collector efficiency drops from 53% down to 28% when tilting the DASC 90° relative to the horizontal. Balakin et al. report this outcome as a result of the reduction in the size of convective patterns. When the tilt angle turns the threshold value at 90°, the collector efficiency curve shift and starts to rise and the efficiency increases until the 180° tilt angle is reached. However, at this point, the DASC achieved lower heat generation efficiency, compared to a 0° tilt angle, due to thermal loss.

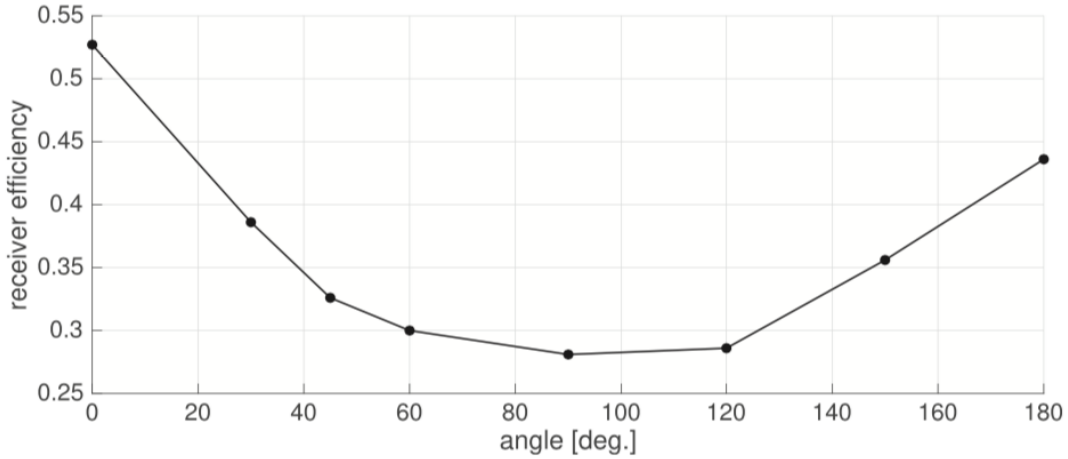

Figure 1.6: Thermal efficiency as a function of DASC orientation [28].

A recent experimental study by Wang et al. [29] further investigated the topic of reverse illumination to enhance the photothermal conversion of nanofluids in DASCs. Reverse illumination, as illustrated in Figure 1.7, causes an upward floating force leading to macroscopic convection of the nanofluid, a phenomenon termed Rayleigh-Bénard convection. Convection dominates the heat transfer rather than conduction, which reduces the temperature gradient inside the nanofluid, as well as heat loss to the surroundings. They proposed a method which significantly increased the photothermal conversion efficiency of

the system from 26% to 51.9% for an illumination time of 10 000 s. Wang et al. stated that for a reverse illumination DASC system, the Rayleigh-Bénard convection was found to alleviate the aggregation and sedimentation of nanoparticles, which leads to a higher effective mass concentration and thereby a higher ability to absorb solar energy. Less nanoparticle aggregation and sedimentation also indicate enhanced nanofluid stability. However, it should be noted that Wang et al. focused only on the heat collection process. The nanofluid was kept stationary in the solar collector and did not flow through the collector as it would have in a functional DASC system.

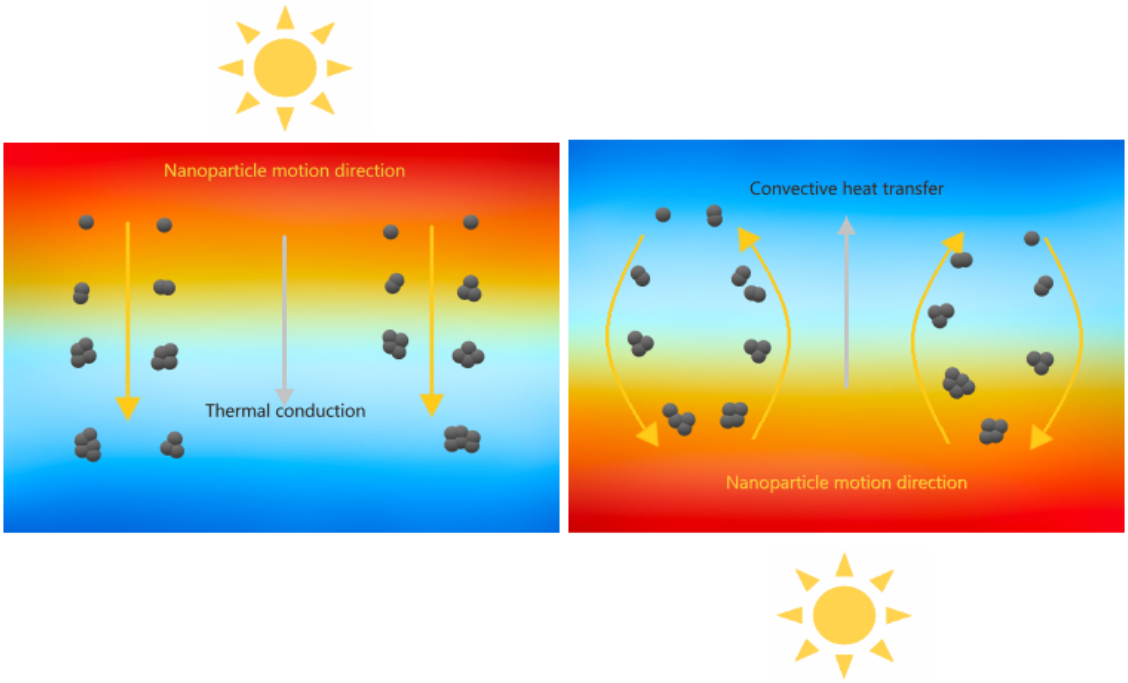

Figure 1.7: Photothermal conversion mechanism of a DASC to the left and a reverse illuminated DASC to the right. Inspired by Wang et al. [29].

In summary, nanofluids show excellent potential for increasing the efficiency and performance of solar collectors. However, most of these results are based on small-scale laboratory solar collectors or numerical and analytical investigations. This preliminary experimental study aims to extend that concept to a full-scale nanofluid DASC for harvesting solar energy. A DASC design is proposed, constructed, and tested under laboratory conditions with varying parameters. The purpose is to develop a functional DASC that later can be tested under non-regulated conditions with a solar concentrator. A complete summary of the specific objects for this work is presented in Chapter 1.3.

1.3 Specific objectives

1. Develop and construct a DASC design.
2. Investigate the surface collector efficiency with the following parameters:
   - Varying the flow rate of water in the range $Q = [0.48, 2.3]$ L/min
   - Orientation of the water column in the field of gravity. Tilt angles 0°, 15°, 45°, and 180° are investigated.
3. Investigate the DASC efficiency with the following parameters:
   - Varying the flow rate of nanofluid and water in the range $Q = [1, 4]$ L/min
   - Orientation of the nanofluid and water column in the field of gravity. Tilt angles 0°, 15°, 45°, and 180° are investigated.
4. Study and evaluate the nanofluid stability for application in the DASC.

Chapter 2

General Theory

This chapter provides the necessary theoretical background to understand the concept of the nanofluid DASC that is studied in this thesis. In the first section, the subject of nanoparticles and nanofluids is introduced and discussed. The next section contains a presentation of the thermal physics basics. This thorough part elucidates heat transfer mechanisms related to DASC performance, as well as a brief introduction to the relevant theory of nanofluid rheology and optical properties. Lastly, the approach to calculating the experimental efficiency of the DASC is elaborated.

2.1 Nanofluid basics

2.1.1 Fundamental understanding

For the past decade, rapid development in nanotechnology has presented numerous cases for the scientists and technologists to research. The concept of a nanofluid is one of the exceptional outcomes of the advancement in nanotechnology, and it has started to become recognised for its unique heat transfer abilities compared to conventional working fluids such as water. As mentioned earlier in Chapter 1.1, a nanofluid can be defined as a stable suspension of nanoparticles in a base fluid [10], where the average nanoparticle size is usually less than 100 nm. Figure 2.1 shows CB nanoparticles with 10^5 magnification.

The purpose of using particles of nano-size is to increase the particle-surface contact area with the surrounding fluid. For solar thermal purposes, an increased contact area is shown to improve the efficiency of which the particles absorb and transmit incoming thermal radiation to the surrounding fluid [31], thus increasing the overall system efficiency. Figure 2.2 illustrates the heat flow and heat exchange between the base fluid and the nanoparticles in a nanofluid-based solar thermal system. The smaller sizing of the particles can be a significant advantage for a multiphase working system. In a system where nanofluids flow without disturbance, a fluid containing larger particles (mm and μm) may clog channels due to agglomeration and clustering. However, a potential drawback of nanofluids is increased viscosity compared to base fluids. From an application perspective, the vis-

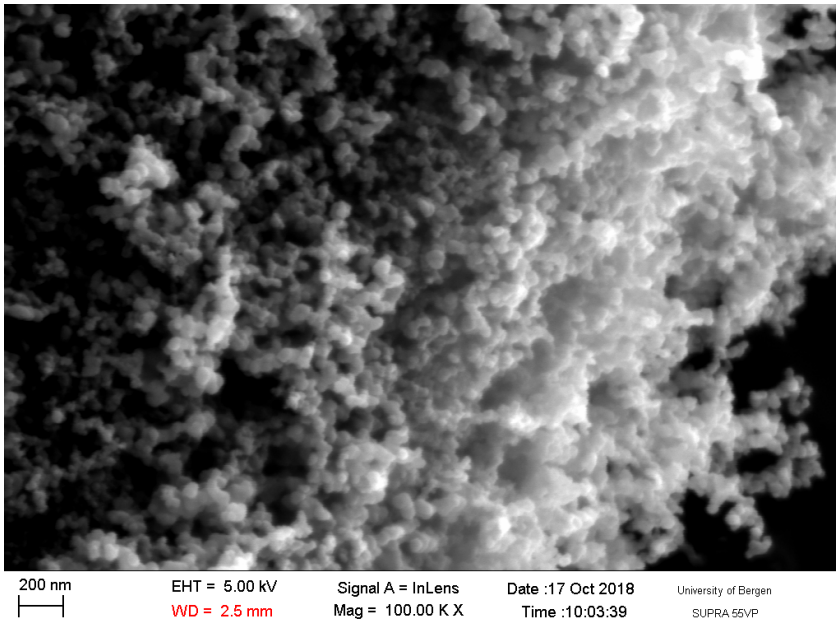

Figure 2.1: SEM image of CB nanoparticles. Reprinted with permission [30].

cosity affects fluid dynamics, and increased pumping power is required for high viscosity circulation or fluid systems.

Generally, the synthesis of nanofluid can be classified in two different ways: single-step- or two-step approach. The single-step approach is when the process of manufacturing and dispersion of nanoparticles takes place directly in the base fluid. Even though the single-batch process involves many stages, the sequence is so rapid that the produced nanoparticles do not have time to be exposed to unwanted environments or to form agglomerates before stabilisation. However, there is a risk of development of impurities due to incomplete chemical reactions inside a nanofluid. Nevertheless, the one-step approach allows for the synthesised nanofluid properties, such as particle geometry and narrow particle size distribution, to be custom made for its application purposes [30]. This process, however, is costly and requires specific materials, equipment and expertise.

In contrast, with the two-step approach, the dry nanoparticle powder is manufactured first and subsequently dispersed into the base fluid. A considerable disadvantage with this approach is that agglomerates easily form in dry nanoparticle powder. Thus, equipment such as ultrasonic baths, magnetic stirrers, and high-pressure homogenisers are essential for dispersing the nanoparticles and for breaking up loosely held *soft* agglomerates. The larger and more well-formed *hard* agglomerates, however, have shown to be resistant to both shear stress and sonication [32]. Despite the apparent disadvantages, the two-step approach is sufficient for most purposes as it is associated with a lower cost and a wide selection of different nanoparticle powders available from producers.

When selecting a nanoparticle material for a specific heat transfer application, many factors need to be considered, such as chemical stability, thermophysical properties, toxicity,

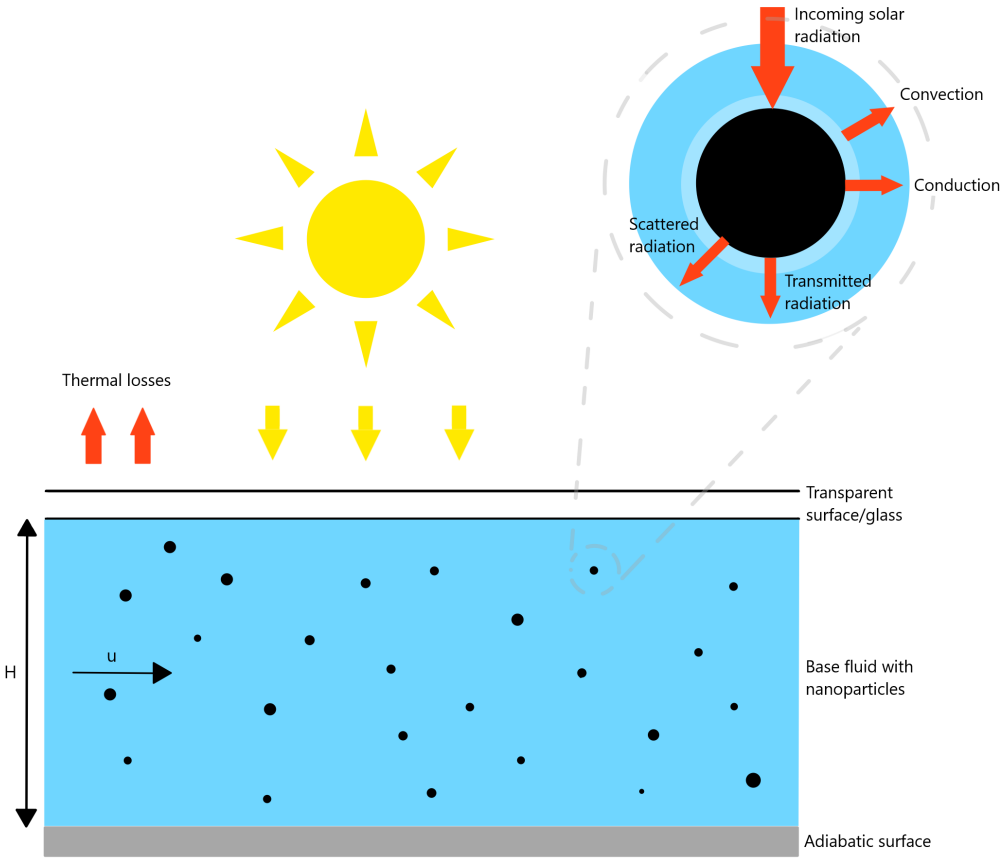

Figure 2.2: Schematic of the heat flow in a nanofluid-based direct absorption collector.

availability, compatibility with the base fluid and cost [33]. Fortunately, numerous options for nanoparticle material and base fluid provide a wide range of applications for nanofluids. Frequently studied nanoparticles include - but are not limited to - copper (Cu), gold (Au), silver (Ag), iron (Fe), copper(II)oxide (CuO), aluminium oxide (Al_2O_3), and carbon-based materials (e.g. graphite, carbon nanotubes, and carbon black) [10], [34], [35]. Commonly used base fluids are water (H_2O), ethylene glycol (EG), EG - H_2O mixtures, and oils [33]. The choice usually depends on heat transfer properties and the specific application of the nanofluid.

The enhanced optical properties of a nanofluid compared to its base fluid are shown to considerably improve the photothermal conversion efficiency, which determines the ability to convert solar irradiation to thermal energy [13]. Therefore, the optical properties (such as absorption, transmittance, scattering, and extinction coefficient) must be regulated carefully, or a nanofluid could be detrimental to the efficiency of a solar collector. Many factors affect the optical properties of a nanofluid, like particle size and shape, film thickness, and volume fraction [36]. If the nanoparticle volume fraction is too high, all

the incoming sunlight is absorbed in a thin surface layer rather than volumetrically in the bulk fluid. As a consequence, the DASC approaches indirect absorption behaviour, similar to a surface collector, which is associated with increased thermal loss to the surroundings. On the other hand, if the volume fraction of nanoparticles is too low, the nanofluid is not capable of absorbing all the incident solar radiation [19].

Carbon black is considered to be one of the very few substances to have absorption characteristics close to that of a black body, which in theory absorbs all incoming radiation [37]. Carbon black nanofluids have shown to have an excellent absorption in the whole wavelength ranging from 200 to 2500 nm [13], which includes the entire spectrum of visible light and portions of ultraviolet (UV) and infrared (IR) light. As a result, carbon black nanofluids have a high potential for utilisation in solar collectors due to beneficial optical properties.

It must be mentioned that regardless of the increased growth of production of nanoparticles and their promising industrial applications, issues relating to toxicity and environmental risks are noteworthy. For example, several researchers [38]–[40] claim that carbon-based nanofluids are potentially cytotoxic and harmful to the environment. On the other hand, two recent reviews of nanomaterials by Lead et al. [41] and Jeevanandam et al. [42] suggest that the general environmental risk of nanoparticles is limited and that the particles, in general, are not intrinsically hazardous. Nevertheless, both reviews conclude that there is a lack of substantial data and knowledge concerning this issue, and there is still need for future research on the potential hazards for ecosystems, possible bioaccumulation, but also related to human exposure.

2.1.2 Stability

Nanofluid long-term stability, stability during working conditions, and stability after thousands of thermal cycles require attention before the commercialisation of nanofluids [43]. From a practical point of view, agglomeration, clustering and sedimentation due to instability can cause two major problems. The first problem results from the decline of photothermal and thermal properties of the nanofluid, whereas the second from the potential build-up of sediments in the solar collector. Circulating sediments can cause tube wall erosion and accumulating sediments reduce flow velocity in channels [44]. A prerequisite for optimising nanofluid thermal properties is a preparation method (as discussed in Chapter 2.1.1), which makes the nanofluid both stable and durable after fabrication.

The high surface energy of the nanoparticles makes the forming of agglomerates often unavoidable. Sedimentation, clustering, and aggregation have shown to affect suspension characteristics such as declining thermal conductivity, viscosity and increasing specific heat of the fluid [45]. The formation of solid particle agglomerates or clusters is a result of van der Waals forces, electrostatic effects and liquid bridges, or a combination of these [46]. Nanoparticles interact energetically in the base fluid through van der Waals interactions as a result of the large surface area and continuous particle-particle collisions caused by random Brownian motion. If excessive amounts of energy are dissipated in the collision, there might not be enough energy available for the particles to rebound; agglomerates

form and may settle at the bottom due to gravity. In contrast to the attractive van der Waals forces, the electrical double layer force separates the particles from each other by steric and electrostatic repulsive mechanisms. Thus, a stable nanoparticle suspension is obtained when the electrical double layer force surpasses the aforementioned attractive forces [43].

A straightforward and economical method for enhancing nanofluid stability is the addition of a dispersant (e.g. surfactants). By chemically altering the surface characteristics of a system, the surfactants effectively prevent the formation of agglomerates. Surfactants are amphiphilic molecules that consist of a hydrophobic tail portion (e.g. long-chain hydrocarbons) and a hydrophilic head group. They are generally classified based on their polar head. If no charge is present, they are called non-ionic. If the head group has a negative or positive charge, they are named anionic or cationic, respectively. A zwitterionic surfactant contains both positive and negative groups. The different types of surfactant have their preferred areas of use and are usually chosen based on the characteristics of the base fluid. Nonetheless, when surfactants are present in a nanofluid, they absorb at the liquid-solid interface and effectively decrease the surface tension of the base fluid. This process promotes the stability and wetting of the dispersed particles [47]. Despite the positive effects of using surfactant in nanofluids, they may also cause several difficulties such as contamination, accelerated degradation and production of foam at high temperatures, and increased thermal resistance [43]. Another severe drawback is that for high-temperature applications, as above 60°C [45], the bonding between the surfactant and the nanoparticles can be damaged, causing the nanofluid to become unstable. Some commonly used surfactants in nanofluids include Sodium Dodecyl Sulfate (SDS), Sodium Dodecylbenzene Sulfonate (SDBS), and Triton X-100.

Manipulating the pH value of the suspension has also proved to enhance the stability of nanofluids, since the suspension stability of an aqueous solution is closely linked to its electrokinetic properties. A well-dispersed suspension can be achieved by promoting high surface potential and thus, strong repulsive forces. The difference in potential between the bulk fluid and the stationary layer of fluid attached to the dispersed nanoparticle is called the zeta potential. Changes in pH have a pronounced effect on the zeta potential and can be used to modify these properties aqueous suspensions [48]. Ghadimi et al. [45] showed that high zeta potential, both positive and negative, represents electrically stable suspension systems, while nanofluids of lower zeta potential induce faster sedimentation of nanoparticles. Finally, it should be noted that optimised pH value for these suspensions varies from one sample to another, depending on types of nanoparticles and other additives added. Conclusively, there are various methods and instruments available for evaluating nanofluid stability, such as UV–Vis spectrophotometer, zeta potential analysis, sediment photograph capturing, scanning electron microscope (SEM), transmission electron microscopy (TEM), and light scattering [49].

2.2 Thermal physics

Within the realm of thermal physics, nanofluids were developed as a concept fluid with exceptionally large effective thermal conductivity, which gave rise to the method of exploiting nanofluids as heat transfer fluids. Consequently, nanofluid properties such as thermal conductivity, k_c, specific heat, c_p, viscosity, μ, and convective heat transfer coefficient, h, are all of great interest.

2.2.1 Heat transfer

Heat transfer is the phenomena where energy and entropy convey from one location to another. There are three fundamental mechanisms of heat transfer that can occur either by themselves or in combination, called conduction, convection and radiation. The heat flow always occurs from a body with higher potential and kinetic energy, in other words, from higher to lower temperatures. This process is consistent with the second law of thermodynamics, which states that all systems have a natural tendency to progress in the direction of increasing entropy; thus heat transfer cannot occur spontaneously from cold to hot as the entropy would then decrease.

2.2.2 Thermal energy of a collector

The following equation gives the heat gain of a working fluid:

$$\dot{Q}_u = \dot{m} C_p (T_{out} - T_{in}), \tag{2.1}$$

where $\dot{m}$ is the mass flow rate for the working fluid in [kg/s], C_p is the *specific heat* of the working fluid in [J/kg·K], T_{out} and T_{in} are the outlet and inlet temperatures in [K].

2.2.2.1 Conductive heat transfer

If a temperature gradient exists in a continuous substance, transfer of thermal energy within the material can occur without bulk motion of the matter [50]. Heat transfer of this kind is called conduction. It is a result of momentum transfer through molecular collisions of adjacent microscopic particles (molecules and atoms) for most liquids and solids. Moreover, for gases, conduction occurs by the random movement of molecules so that heat diffuses from hotter areas to cooler ones. Although conduction takes place in all sorts of matter, it is most significant for highly electrical conductive solids. These generally have a correspondingly high thermal conductivity [51]. For such solids (usually metals) the thermal conduction results from the motion of free electrons. Fourier's law states that the heat flux is proportional to the negative temperature gradient. The total conduction for a one-dimensional flow is given as:

$$\dot{Q}_{co} = -k_c S \frac{dT}{dx}, \tag{2.2}$$

where k_c is the proportionality constant called *thermal conductivity* (a property of the fluid or material), S is surface area, and $\frac{dT}{dx}$ is the temperature gradient over the distance

x normal to the surface. Amongst the various thermophysical properties of a fluid, the thermal conductivity has a more considerable role in heat transfer behaviour. Adding nanoparticles to a base fluid causes a profound increase in the thermal conductivity, which is also proven to have a beneficial effect on the convective heat transfer [52].

Whether an object acts as a thermal conductor or insulator depends on the thermal resistive properties of the material. The thermal resistance (R) is a measure of a material's ability to retard conductive heat transfer through a given thickness, given as:

$$R = \frac{L}{k_c}, \tag{2.3}$$

where L is the material thickness.

2.2.2.2 Convective heat transfer

Convective heat transfer occurs in the presence of fluid motion, where the motion is either forced or natural. Forced convection may be initiated by a mechanical device such as a pump, while differences in density created by a temperature gradient drive the natural convection. Accordingly, mixed convection is when both forced and natural convection drives the fluid motion, which is the case for most fluid flows [53]. Newton's law of cooling establish that the intensity of the heat transfer depends on the temperature difference of the physical systems in question [54]. For convective heat transfer purposes, this implies that the heat flux ($\dot{Q}_{cv}$) is usually proportional to the temperature difference between the surface of a particle and the surrounding fluid, though this premise is only accurate when assuming that the *heat transfer coefficient*, h, is independent of temperature.

$$\dot{Q}_{cv} = hS(T_s - T_f), \tag{2.4}$$

where S is the particle surface area, and $(T_s - T_f)$ is the temperature difference of the surface and the bulk fluid, respectively. Furthermore, the dimensionless Nusselt number characterises the convective heat transfer, and it is regarded as the ratio of convective to conductive heat transfer $Nu = \frac{hL}{k_c}$, where h is the heat transfer coefficient, L is the characteristic length, and k_c is the thermal conductivity. Unlike the thermal conductivity, the heat transfer coefficient is not a property of the particle material. Instead, it depends on the type of interface between the body and the surrounding fluid (solid-liquid or solid-gaseous) and the interface characteristics. Therefore, the heat transfer coefficient is affected by many parameters, such as the fluid flow properties and behaviour (e.g. velocity, viscosity, turbulence) and interface geometry. Also, the addition of nanoparticles to a liquid coolant (i.e. nanofluid) has shown to improve its heat transfer coefficient [55]. The subsequent expression, which includes the Nusselt number, is an approximation for the total convection for a particle-fluid flow:

$$\dot{Q}_{cv} = Nu\pi Dk_c(T_s - T_f), \tag{2.5}$$

where Nu is the Nusselt number, and D is the particle diameter. For a stagnant medium with no convection, the Nusselt number is equivalent to 2. Nonetheless, as the rate of the convective heat transfer increases with the relative fluid velocity to the particle, it is possible to compensate for the forced convection effects by the increased fluid velocity, by using the Ranz-Marshall correlation [56]:

$$Nu = 2 + 0.6 Re_r^{\frac{1}{2}} Pr^{\frac{1}{3}}, \tag{2.6}$$

where Re_r is the relative Reynolds number and Pr is the Prandtl Number $Pr = \frac{\mu c_p}{k_c}$. This correlation is a good fit for data with relative Reynolds number up to approximately $5 \cdot 10^4$ [46].

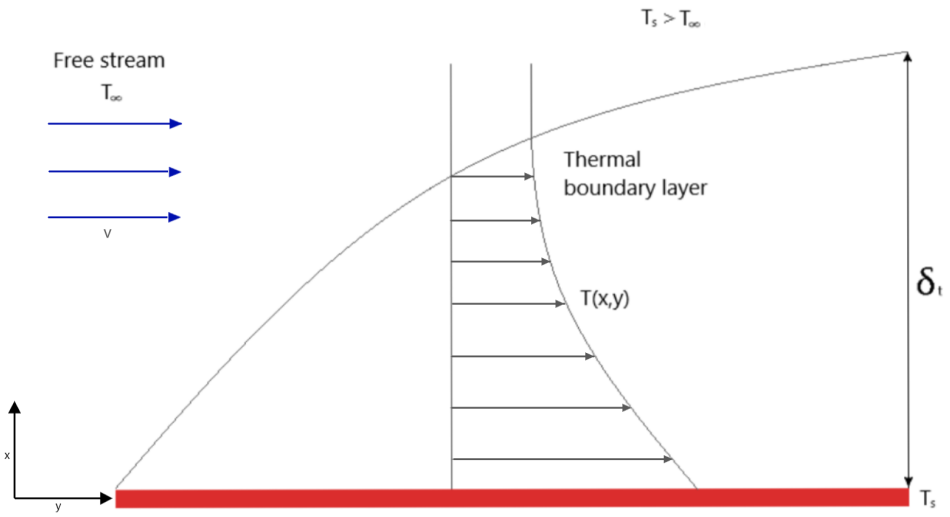

Figure 2.3: Thermal boundary layer on a hot flat-plate surface.

A thermal boundary layer occurs when a fluid at a given temperature flows over a surface with a different temperature. A temperature profile then develops in the flow field that ranges from T_s to T_∞, given as the surface and free stream fluid temperature, respectively. The thermal boundary layer thickness, δ_t, can be defined as the distance from the surface to the point where the temperature is within 1% of the free stream fluid temperature [57]. The thickness of the thermal boundary layer increases in the flow direction because the effects of heat transfer are felt at greater distances from the surface downstream. This is illustrated in Figure 2.3. An estimate of thickness can be done using thermodynamic calculations, including dimensionless groups, such as the Prandtl number and Grashof number. Parameters such as film temperature, volumetric expansion coefficient, and kinematic viscosity must also be known.

2.2.2.3 Radiative heat transfer

All physical substances above a temperature of 0 K in solid, liquid and gaseous states can emit and absorb energy by the process of electromagnetic radiation. Electromagnetic radiation from a body is due to vibrations and rotational movement of its molecules and atoms, which implies that the emission rate of an object increases with its temperature. The emitted radiative energy then propagates as an electromagnetic wave from its source. Contradictory to convection and conduction, where an intervening medium is a process requirement, electromagnetic radiation propagates through both matter and vacuum. Figure 2.4 represents the electromagnetic spectrum, the range of frequencies of electromagnetic radiation and their respective wavelengths.

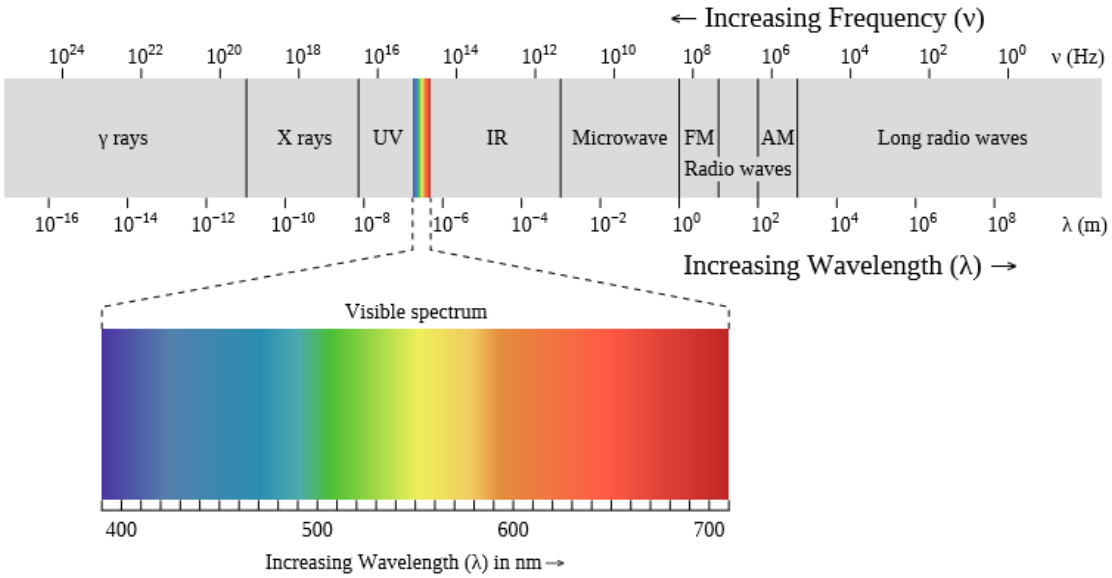

Figure 2.4: Spectrum of electromagnetic radiation with the visible portion highlighted [58].

When an electromagnetic wave hits an object, the wave partially loses its energy and gives rise to electronic and molecular transitions, or lattice vibrations in the receiving body [59]. This concept is named absorption. It causes an energy gain in the receiving body, recognized as rising temperature. Additionally, portions of the incident radiation are reflected or transmitted by the body. The sum of the absorbtivity, reflectivity and transmissivity of a body must always be unity. A surface that absorbs all incident radiation and reflects none is called a black body. The Stefan-Boltzmann [60] law of thermal radiation states that for a black body, the surface energy radiation rate per unit area is equal to the fourth power of its temperature:

$$\dot{q}_{emit} = \epsilon \sigma T_s^4, \tag{2.7}$$

where $\dot{q}_{emit}$ is the energy emission rate from its surface, ϵ is the emissivity ($0 \leq \epsilon \leq 1$), T_s is the surface temperature of the body, and σ is the Stefan-Boltzmann constant. The

emissivity represents how close a surface approximates a black body, where the maximal value $\epsilon = 1$ resembles an idealised black body. For solar energy applications, a body with extraordinary absorptivity is crucial since transmission and reflection of radiation lead to potential energy losses. However, no real physical objects fit the definition of a black body, because all materials reflect some small fraction of incoming radiation that hits their surface. However, certain materials are considered to have near black body properties, like carbon black, platinum black, carborundum, and soot [37]. Assuming that an environment with uniform temperature (T_s) surrounds an particle with a temperature (T_d), the net rate of heat transfer [46] by radiation is:

$$\dot{Q}_{rad} = \epsilon\sigma\pi D^2(T_s^4 - T_d^4), \tag{2.8}$$

where D is the diameter of the particle.

2.3 Nanofluid rheology

Even though a lot of earlier research work has focused on the subject of the enhanced thermal conductivity of nanofluids, the rheological behaviour of fluids is another essential subject that requires attention, due to its crucial influence on heat transfer. A review of nanofluid viscosity by Meyer et al. [61] reports that different nanofluids show varying rheological characteristics ranging from Newtonian to non-Newtonian behaviour. The non-Newtonian properties like shear thinning, shear thickening and thixotropic behaviour were observed. Moreover, a study conducted by Han et al. [13] found that carbon black nanofluids exhibited shear-thinning behaviour. They also marked that the CB nanofluid shear viscosity increased with increasing volume fraction, and decreased with increasing temperature when subjected to a constant shear rate by a controlled stress viscometer.

Many key system parameters such as pumping power and the pressure drop for laminar flows are profoundly affected by the viscosity. In general, nanofluids exhibit a markedly higher viscosity in comparison to their base fluids [62], and it further increases with a rising concentration of nanoparticles. Several studies show that particle size and shape, temperature, particle loading, the addition of surfactants and acidity (pH) have a direct effect on the viscosity of nanofluids [61]. The model developed by Einstein [63] in 1906 is still of great importance, as it is the first available theoretical work on the viscosity of a colloid suspension. He stated this model to be valid for viscous fluids containing spherical particles at a rather small volume fraction ($\alpha \leq 0.02$):

$$\mu_{nf} = \mu_f(1 + [\eta]\alpha), \tag{2.9}$$

where μ_{nf} is the effective viscosity of the nanofluid, μ_f is the dynamic viscosity of the base fluid, $[\eta]$ is the intrinsic viscosity of the suspension, and α is the volume fraction of nanoparticles in the suspension. Equation (2.9) shows that there is a linear increase in viscosity with particle volume concentration nanofluids. The coefficient $[\eta]$ is a function of the particle shape and, potentially, size of the nanoparticles. $[\eta]$ is equal to 2.5 for hard spheres. However, the model assumes that there is an absence of interaction between particles, which is not a valid assumption for colloidal suspensions. Consequently, there have been numerous theoretical models developed in efforts to extend the Einstein model to concentrated and particle-particle interacting suspensions [64]–[67].

2.4 Nanofluid optical properties

Absorbance (A), also known as optical density, is a measure of the quantity of light absorbed by a solution. It differs from absorptivity since it also includes reflection and scattering phenomena in a medium. The logarithmic relationship between the incident radiative heat flux (I_0) to the transmitted radiative heat flux (I) gives the absorbance:

$$A = \log_{10}(\frac{I_0}{I}). \tag{2.10}$$

Beer-Lambert law [68] relates the attenuation of light to the properties of the material. The law states that there is a linear relationship between the absorbance and the concentration of a sample:

$$A = \varepsilon l c, \tag{2.11}$$

where ε is the molar attenuation coefficient or the absorptivity with units [L/mol·cm], l is the optical path length in [cm], and c is the concentration of solute in the solution in [mol/L]. The law holds for most dilute solutions, but it can only be applied when there is a linear relationship, as stated above. The absorbance is measured using spectroscopy, which is a method that measures the attenuation of light by chemical substance.

2.5 Volumetric heat generation efficiency of the DASC

As the incident irradiation transmits vertically through a transparent glass plate on a DASC, the energy is volumetrically absorbed by the suspended nanoparticles. Simultaneously, the base fluid is heated by the absorbed heat from the nanoparticles. Since the top plate is transparent, most of the radiation passes through, which is crucial for the performance of the DASC. As previously stated, the amount of heat the collector generates is determined by the optical and thermal losses [24]. Consequently, the experimental thermal efficiency of a DASC is defined as the ratio of collected thermal energy to the total radiation incident on the collector surface [21], [26]:

$$\eta = \frac{\dot{m} C_p (T_{out} - T_{in})}{G_T S}, \tag{2.12}$$

where the nominator is the heat gain of the working fluid, $\dot{Q}_u$, in [kW], as given in equation (2.1), G_T is the solar irradiance in [W/m^2], and S is the solar collector surface area in [m^2]. Equation (2.12) reveals that when there is a constant incident solar radiation, G_T, and solar collector area, S, the heat gain must increase to maximize the thermal efficiency of a solar collector. Two different expressions can be used for calculating the specific heat, C_p, of nanofluids used as a working fluid under constant pressure [69]:

$$C_{p,nf} = \frac{\rho_{bf} C_{p,bf}(1-\alpha) + \rho_{np} C_{p,np} \alpha}{\rho_{nf}}, \tag{2.13}$$

or

$$C_{p,nf} = (1-\alpha) C_{bf} - \alpha C_{p,np}, \tag{2.14}$$

where ρ_{bf}, ρ_{np} and ρ_{nf} is the base fluid, nanoparticle and nanofluid density respectively, $C_{p,bf}$ and $C_{p,np}$ is the base fluid and nanoparticle specific heat, and α is the volume fraction of the particles in the nanofluid. Khanafer and Vafai [70] showed that the relation in (2.13) is in better agreement with experimental data, than the more straightforward relation in (2.14). Finally, the nanofluid density [69] can be estimated by the following expression :

$$\rho_{nf} = \rho_{bf}(1-\alpha) + \rho_{np}\alpha. \tag{2.15}$$

Chapter 3

Methodology

This chapter contains the characterisation of the DASC design, a description of the development process of the experimental setup at UiB, the nanofluid preparation procedure, as well as a nanofluid stability analysis method. The variables for the experimental efficiency calculation are presented in Table 3.1. The results are found later in Chapter 4.1 and 4.2. Table 3.2 summarises the various instruments and equipment that have been used in this experimental study. Tap water was used as the working fluid for the experiments with a surface solar collector and DASC. Data regarding tap water quality and chemical composition can be found in Appendix A.

Table 3.1: Variables used to calculate experimental efficiency, η, from Equation (2.12)

Variable	Value	Obtained from
$\dot{m}$	kg/s	Turbine flow meter, Table 3.4 and calculations
$C_{p,nf}$	J/kg·K	Table 3.4 and equation (2.15)
ΔT	K	Pt100 elements and PT-104 Data Logger
G_T	2000 W/m^2	LS122 Infrared Power Meter
A (DASC)	0.08475 m^2	Measuring tape, caliper and calculations
A (surface collector)	0.0936 m^2	Measuring tape and calculations

Table 3.2: Summary of instruments and equipment.

Equipment	Manufacturer	Range	Uncertainty
Pt100 elements	Pico Technology	-50 to +250°C	± 0.03°C
PT-104 Data Logger	Pico Technology	-200 to +800°C	± 0.015°C 0.01% of reading
Measuring tape	Biltema	3 m	± 0.001 m
Caliper	Biltema	150 mm	± 0.02 mm
CPA 324S balance	Sartorius	320 g	± 0.1 mg
Precision balance 440	KERN	200 g	± 0.01 g
Digital protractor	Limit	0 to 180°	± 0.3°
FLIR E8 infrared camera	FLIR	-20 to +250°C	2%
LS122 Infrared power meter	Linshang Technology	40 000 W/m^2	10%
Mastersizer 2000	Malvern	-	-
3510 Ultrasonic cleaner	Branson	40 Hz	-
Turbine flow meter	[71]	*	10%
King-4 submersible pump	Resun	80 L/min, 90 W	-
BP 3 Home & Garden pump	Kärcher	55 L/min, 800 W	-
XKJ-1305S Garden pump	Co/Tech	65 L/min, 1300 W	-

*This device was custom made. Additional documentation was not available.

3.1 DASC Design

In this section, the DASC design is presented and discussed. Identical collector geometry is used for both direct solar absorption and for the indirect surface absorption case, which is addressed later. As previously shown, Equation (2.12) states that the volumetric heat generation efficiency is the ratio of collected thermal energy to the total incident radiation on the collector surface. In practice, this means that for a given flow rate, heat capacity, and irradiation strength, the optimal DASC design must bolster maximum solar absorption, hence achieve the largest achievable temperature difference between the collector inlet and outlet. Rectangular e.g. [10], [20]–[22], [26], [27], [72]–[74] and cylindrical DASCs e.g. [24], [29], [75] are arguably the most well-known and investigated geometries. Amidst the different design specifications, the collector depth (nanofluid film thickness) is recognised to have a significant impact on the final collector efficiency [18], [24], [27].

A DASC can be classified by the temperature level under which the collector operates: low-temperature ($\sim$ 65°C), medium-temperature which is normal in a system that concentrates solar energy ($\sim$ 100-200°C), and high-temperature ($>$ 500°C) where steam generation is possible for power generation [76]. The DASC used in this study was targeted for low-temperature operation, which is not expected to exceed 60-80°C, even if used together with a solar concentrator. The solar concentrator in question is located at Western Norway University of Applied Sciences (HVL). The concentrator is of a parabolic 2-axis type, which means that the entire collector moves to align with the position of the Sun over the day. Since this work aimed to develop a DASC that later could be tested with the specific solar concentrator, design specifications such as a weight limit and custom attachments must be taken into account.

The DASC design consists of three main elements: a glass surface, an inner plate structure with baffles, and an external aluminium box with hose connectors. Figure 3.1 shows a schematic illustration of the DASC design. The initial DASC design had a 4 mm regular glass surface. Unfortunately, this type of glass was not capable of sustaining the necessary pressure needed to seal the edges when seated onto the aluminium box, while experiencing pressure in the opposite direction from the baffles. It is worth mentioning that regular glass is prone to crack due to fluid pressure inside the collector, even when successfully mounted. The regular glass was replaced with tempered glass, which allows for more pressure and external tension. A similar solution was also chosen by Karami et al. [72] when experiencing comparable design difficulties. It can be expected that a fraction of incoming radiation reflects when entering a layer of glass. Eggers et al. [27], however, found that there is only a small difference of reflective losses for two layers of glass on a volumetric absorber compared to a black surface absorber.

The plate structure and baffles were made of Polypropylene (PP) plastic, which is a thermoplastic polymer of low density and high heat resistance ($\sim$ 160°C [77]). The baffles can be detached and replaced, which opens up for the possibility to experiment with varying DASC geometries such as depth. Additional baffles can also be attached for future experiments so that the fluid will have longer residence time inside the DASC, hence more time to absorb heat. Nonetheless, the earlier discussed article by Karami et al. [26] includes

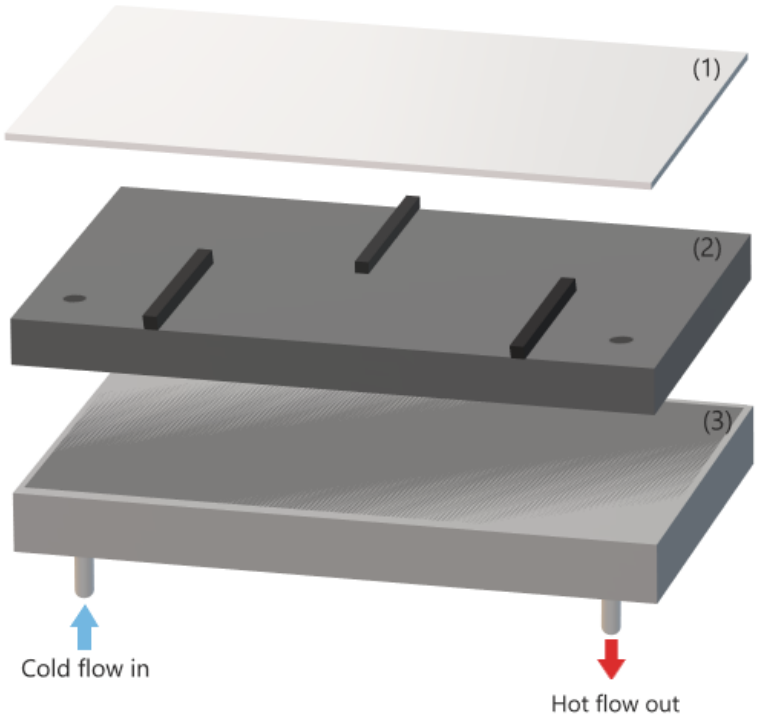

Figure 3.1: Schematic illustration of the DASC design. (1) Glass surface, (2) Inner plate structure with baffles, and (3) External aluminium box with hose connectors.

a convenient summary of analytical and numerical studies concerning low-temperature nanofluid DASCs, where the dimensions of the relevant DASC designs are also listed. A great variety of DASC depths are filed, ranging from 1.2-100 mm, while some experimentally investigated depths are in the range 0.15-15 mm [10], [20], [21]. The depth set for this experimental work was 19 mm.

Matte black paint was used to alter the optical behaviour of the bottom surface of the DASC to become absorptive, and thus reduce the reflection of incident radiation back into the nanofluid to a minimum. Figure 3.2 shows the DASC before it was painted and fully assembled. Sharaf et al. [25] found that it is possible to achieve thermal trapping for the highest temperature layers within the nanofluid for collectors with absorptive bottom surfaces with high emissivity. Thermal trapping is advantageous since it may lead to reduced convection and radiation losses from the glass surface to the ambient environment. The paint was of the high temperature-resistance type ($\sim 600°C$), so the risk of degradation and potential contamination of the nanofluid when heated, was reduced to a minimum.

Table 3.3 shows the relevant dimensions of the collector design. The overall exposed surface is calculated from the dimensions of the inner plate structure. The effective exposed surface area is calculated by subtracting the combined area of the three baffles from the overall exposed surface. For the simulated surface collector experiments, the collector area was considered to be equal to the overall exposed surface.

Table 3.3: DASC specifications.

Specification	Dimension
Collector	(0.39 × 0.23) m
Baffles	(0.02 × 0.1475 × 0.019) m
Overall surface	0.0936m^2
Effective surface	0.0809m^2

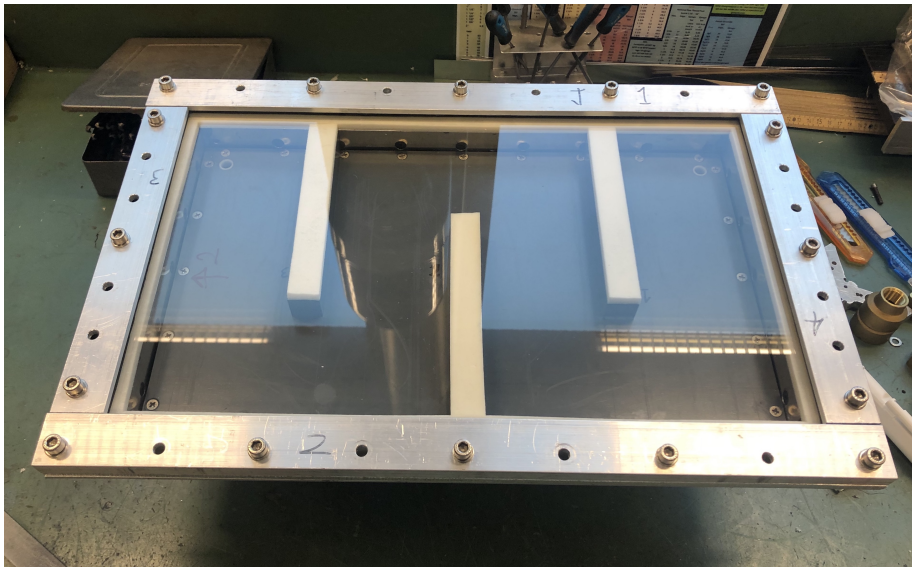

Figure 3.2: DASC design before the bottom surface was painted matte black. The white foam gasket was replaced with a black rubber gasket before operation.

A custom-made bracket was mounted on the rear of the outer aluminium box, illustrated in Figure 3.3, so that the DASC can be easily attached to the solar concentrator for future experiments. The parabolic solar concentrator consists of numerous mirrors directed towards a common focal point where the DASC is thought to be placed during the experiments. Figure 3.4 is a photo displaying the solar concentrator, though the solar collector attached is not this current DASC. The mirrors can easily be removed to adjust the solar irradiation intensity on the DASC.

For the surface solar collector experiments with water, the glass was covered with a layer of duct tape and then painted matte black to mimic a black surface or a surface absorber, which is used on a conventional solar collector. Figure 3.5a and 3.5b show the solar collector with the black surface. The method of using duct tape was chosen due to availability, cost-effectiveness, as well as for easy removal for the experiments with a transparent surface. Moreover, duct tape also contains small amounts of powdered aluminium pigments in order to give the tape its silver colour. As known, aluminium is a metal which has very high thermal conductivity. This is beneficial for the heat transfer process. On the other

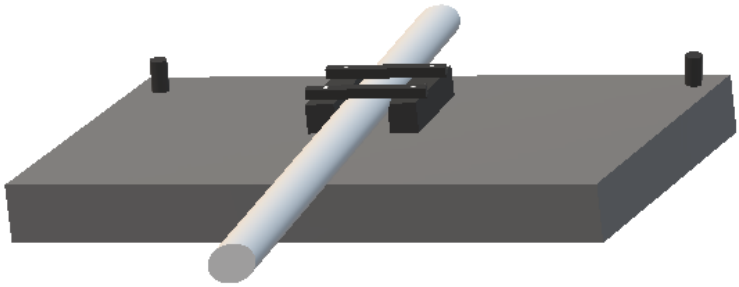

Figure 3.3: Custom made bracket mounted on the rear of the exterior aluminium box for application with the solar concentrator.

Figure 3.4: Photo of the solar concentrator at HVL.

hand, it is uncertain to what degree the duct tape glue allows for heat transfer since its thermal conductivity is not easily characterised. For future experiments, however, this technique could be improved, for instance by pure aluminium tape, black matte foil, or even a selective surface absorber such as TiNOX® Energy [10].

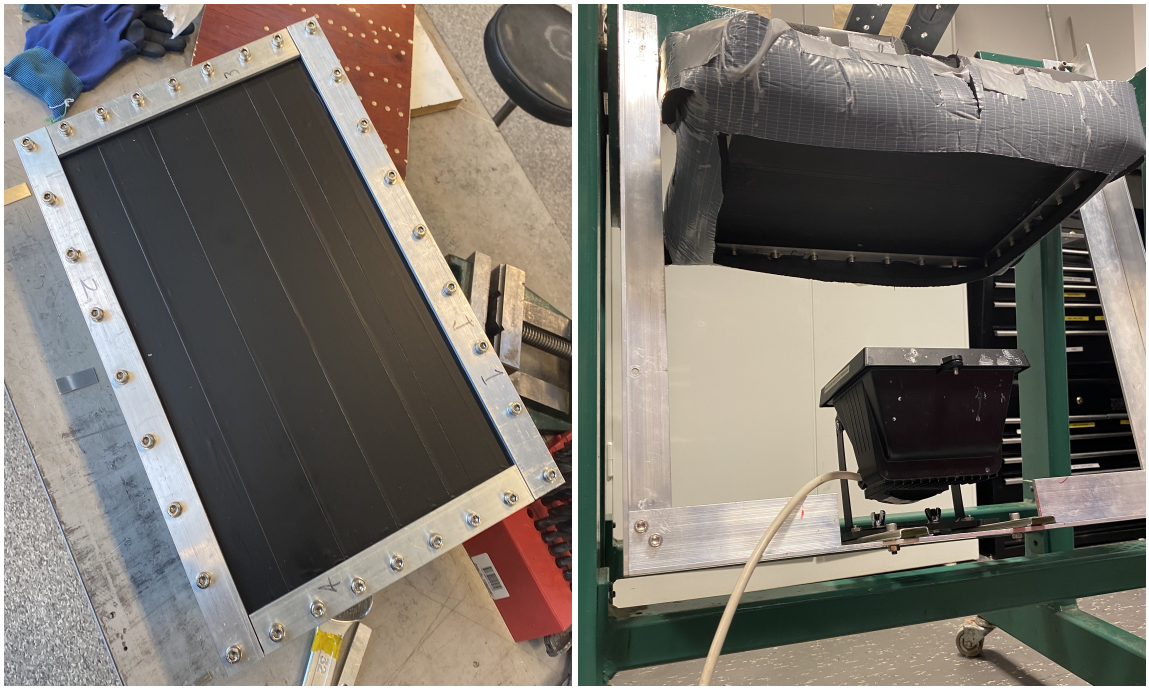

(a) Duct tape with matte black paint.

(b) Isolation covering the aluminium box.

Figure 3.5: Illustration of the black surface on the solar collector.

3.2 Flow through the system

Figure 3.6 shows the process flow diagram for the experimental setup. Four Pt100 sensors monitored the DASC inlet and outlet temperatures, ambient temperature, and bulk fluid temperature in the reservoir tank. The working fluid was circulated from a $\sim$ 12 L reservoir tank made of thermoplastic material (PMMA) through a total of 20 m plastic tube. The 12/10 mm tube was made of Polytetrafluoroethylene (PTFE), a synthetic fluoropolymer which is a hydrophobic material with a very low friction coefficient. The turbine flow meter had a display for manual observation of the volumetric flow rate through the system. The flow rate could be adjusted by a simple flow-control ball valve placed after the pump. Further adjustments of the flow rate could also be made using a bypass line. The entire system was insulated to reduce heat loss. The DASC itself was insulated with sheets of Armaflex class 0 SK isolation with thermal conductivity $k_c = 0.003$ W/mK, and the tube system with 13 mm pipe insulation of polyethylene foam from Biltema.

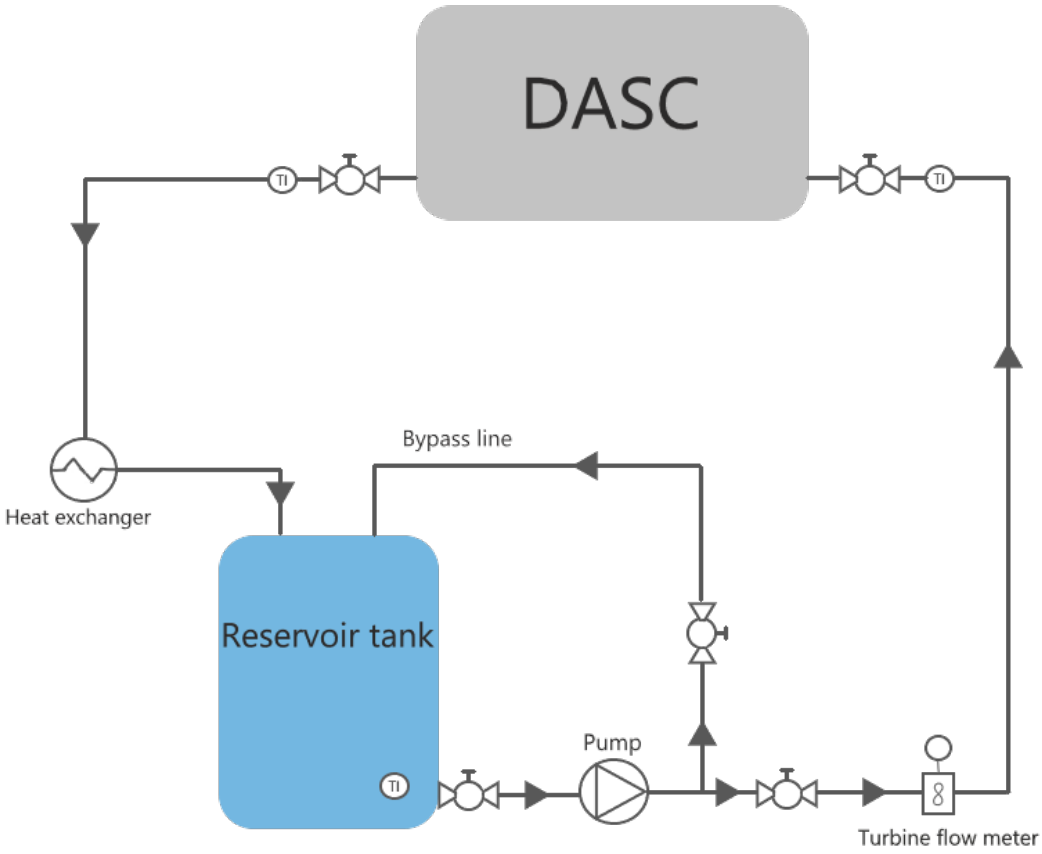

Figure 3.6: Process flow diagram for the experimental setup.

As addressed in Chapter 2.1.2, there is an ongoing discussion regarding the toxicity of nanoparticles, and whether exposure is potentially harmful to humans and the environment. Previous investigation by Thon [30] and Ulset [78] reveal presence of nanoparticles

in vapour from CB nanofluids. Therefore, to prevent the laboratory air from becoming contaminated by nanoparticles, a custom cover for the reservoir tank was made. Furthermore, several small holes were also drilled in the cover and covered with filters to keep pressure from building up in the reservoir tank.

3.2.1 Turbine flow meter and pumps

A turbine flow meter, which is a volume sensing instrument, was used to measure the flow rate through the system. As the working fluid passes through the turbine housing, it causes the freely suspended turbine blades to rotate. The turbine blades are made of a ferromagnetic material such that each blade forms a magnetic circuit together with a permanent magnet and a coil in the meter housing. The voltage induced in the coil has the form of a sine wave whose frequency and amplitude are both proportional to the angular velocity of the blades. The rotor angular velocity, measured in *pulse numbers*, is then proportional to the volumetric flow rate of the fluid passing through the flow meter, which can be calculated for a known cross-sectional area.

It must be noted that turbine flow meters are delicate instruments since the blades and bearings can be damaged by solid particles present in the fluid [79]. Furthermore, the original calibration of the instruments depends on the density of the working fluid, which implies that the flow meter is not calibrated for the use of nanofluids. However, since the amount of nanoparticles in this work is of minuscule concentration, it can be argued that the particles will present an insignificant disturbance to the instrument. Nonetheless, the turbine flow meter used in this work has a given accuracy of 10%. The resolution is 1 pulse per second, which is equivalent to 0.0839 litres per minute for a 10 mm tube. The following equation describes this particular turbine flow meter and is obtained from calibration by the manufacturer [71]:

$$\text{Flow} = \text{pulse\_numbers} \cdot 0.0839 + 0.1033 \tag{3.1}$$

During initial measurements, it was observed that the turbine flow meter frequently presented a fluctuating volume flow rate, usually between two values. In such cases, an average flow rate for the two observed values was used in the efficiency calculations. Many factors can affect the volume flow rate, such as uncertainty and resolution limitation of the flow meter instrument itself, and the working fluid properties such as viscosity and density. The pump operating temperature and pressure, heating effects, as well as possible cavitation can also cause the pump to provide a fluctuating flow rate. Air bubbles in the working fluid can also cause inaccuracy in the flow meter readings. As a measure of prevention, the working fluid was always circulated for a reasonable time ($\sim$ 0.5-1 hour) before starting the measurements, to reduce the number of bubbles in the system.

For the surface collector experiments, a Resun King-4 submersible 90 W pump with a given maximum flow rate of 80 L/min by the manufacturer [80], was used. It was observed, however, that the pump only provided a maximum of 2.37 L/min when circulating the water through this particular DASC system, even with the bypass-line valve fully closed.

As a result, the flow rate could only be varied within a minimal range. A plausible cause is that the narrow piping and fitting diameters (10 mm) were restricting the flow. The water would require a considerable amount of pressure to flow with a higher velocity through the system. The Resun pump motor also dissipated some energy to the water, observed as a slight increase ($\sim$ 0.1°C) of the temperature between the reservoir tank and the DASC inlet.

For the DASC experiments with water, the Resun pump was replaced with a Kärcher BP 3 Home & Garden pump, due to a leakage in the outlet port. Custom made metal fittings for the system is likely to have damaged the more brittle plastic material of the threads and outlet port in the Resun pump. This pump was later used for the cooling system, which is discussed in Chapter 3.2.2, since leakages are naturally not problematic while the pump is submerged.

The more robust Kärcher pump managed to increase the flow rate through the system beyond that of the Resun pump. A threshold flow rate of 4 L/min was set for the experiments. Higher flow rates, such as $\sim$ 5 L/min, increased the pressure to the point where the gasket between the DASC frame and the glass surface started to leak. For future improvement of the DASC design, the current gasket solution needs to be modified to allow for the possibility of performing experiments with higher flow rates. Nevertheless, the bypass-line valve needed to be fully open at all times to keep the flow at an acceptable rate into the system. With the Kärcher pump, the DASC system obtained a steady-state temperature with the surroundings at around $\sim$ 38-39°C. The steady-state temperature is at a constant temperature level where the system is in thermal equilibrium with the surroundings. An illustrative temperature history plot, which shows the steady-state regions, are found in Figure 3.7. This equilibrium temperature accounts for the heat dissipated from the pump into the system, and heat dissipated to the surroundings by the heat exchanger. Other sources of heat loss from the system would be the DASC surface and the part of the aluminium box that is not fully isolated. The DASC operating steady-state temperature (i.e. with solar irradiation) varied between $\sim$ 40-45°C.

Unfortunately, the Kärcher pump was not able to function properly with nanoparticles in the fluid. After 10 min of circulation, the pump stopped. A built-in safety function might have registered a different load than regular water (e.g. a slight increase in viscosity due to the nanoparticles, or the nanoparticles themselves). It must be noted that the detachable filter in the Kärcher pump was removed before nanofluid was used in the system, and the pump was fully operative. Consequently, the Kärcher pump was replaced with a Co/Tech XKJ-1305S garden pump, which operated well with nanofluids in the system. However, since it could provide even higher pressure in the system than the Kärcher pump, the new equilibrium temperature between the system and the surroundings increased to $\sim$ 40-41°C. The higher equilibrium temperature can be a result of the pump motor overheating when trying to force the fluid through a system with very narrow pipings.

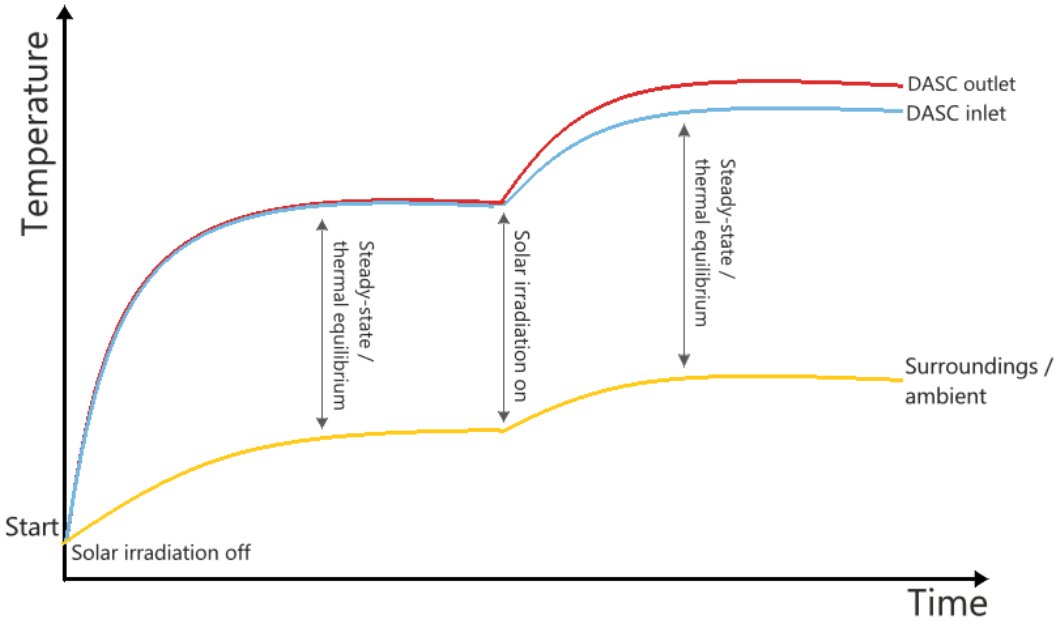

Figure 3.7: Illustrative temperature history plot for the DASC system from start.

3.2.2 Cooling system

As an effort to improve the efficiency of the passive heat exchanger, an external cooling system was assembled. The heat exchanger was placed in a container filled with tap water, which was returned to the laboratory sink by garden hoses and the Resun King-4 submergible pump, illustrated by Figure 3.8. The combination of the high heat capacity of water and the high thermal conductivity of the aluminium radiator (the heat exchanger) made this method exceptionally efficient for dissipating heat from the system.

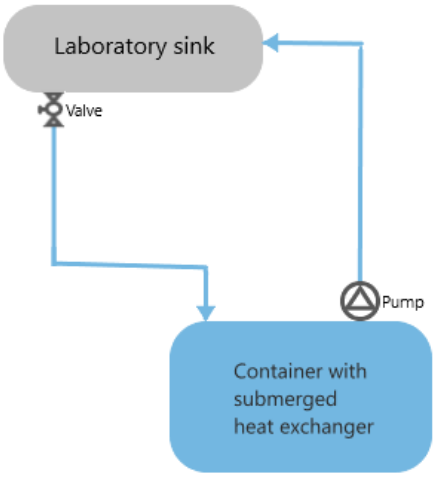

Figure 3.8: Process flow diagram for recirculating cooling system.

In theory, the cooling system would make it possible to set the temperature difference between the system and the surroundings. This is done altering the temperature of the water in the cooling container, thus regulating how much heat is dissipated from the system while keeping the reservoir tank at a constant temperature. As previously stated in Chapter 1.1, both solar collectors and SPV systems, in general, suffer from low efficiency due to the large temperature gradient between the system and the surroundings. Therefore, the ambition was to make it possible to investigate the DASC efficiency with a varying temperature difference between the system and the surroundings. Additionally, if the reservoir tank temperature could be kept at a stable level, it would have been possible to record and compare the heat generation over time, i.e. how fast the system heats up to a certain point, for the different experimental cases.

It was quickly recognised, however, that the temperature of the tap water was not stable enough, and the desired state where the system temperatures maintained a constant level, was difficult to reach. Consequently, it was decided not to use this cooling system. The heat exchanger was rearranged to the initial idea with a fan working to raise the convection efficiency from the heat exchanger to the surroundings. For future experiments, a laboratory-grade thermostatic bath would be more likely to keep the reservoir tank at a constant temperature.

3.2.3 Cleaning of the system

After the baseline experiments with water were completed, the water was removed, and the system was dried thoroughly with compressed air. Later, when the first batch of nanofluid had to be replaced, additional cleaning was required to remove all possible remains of nanoparticles. Firstly, the system was flushed with tap water to clean out the nanofluid. Next, the system was set to circulate water for a day. The water was replaced regularly. The following day, a solution of 40wt.% sterile 70% isopropanol and 60wt.% tap water was circulated for half a day before the system finally was flushed by tap water and dried by compressed air.

Isopropanol is an alcoholic disinfectant frequently used for industrial cleaning purposes. It was chosen as an alternative to the ethanol which has previously shown to be quite capable of cleaning nanoparticles from such systems [81]. However, due to the COVID-19 situation, the university could not acquire the desired amount of ethanol within a reasonable time. Nonetheless, the reservoir tank and the DASC itself were dismantled for a more comprehensive cleaning with a sponge and regular dish soap. Extra caution was taken to remove all remains of soap so that the new nanofluid would not be contaminated and become unstable. Despite the effort, there was still visible contamination of nanoparticles in the tubes, which is shown in Figure 3.9b. Nevertheless, since the system has run with water and the isopropanol/water solution for a longer period, the remaining particles are believed to have adhered to the tubes. One can therefore assume that these particles do not present a high risk of contamination in a new circulating nanofluid.

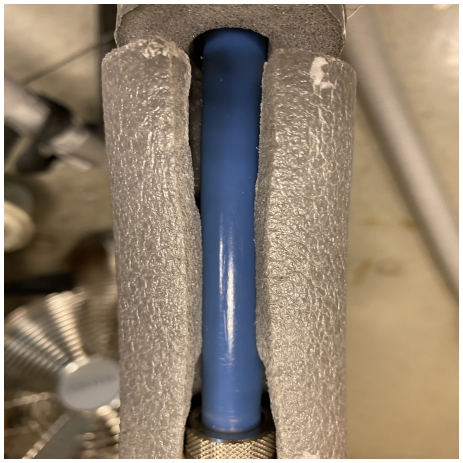

(a) Before cleaning.

(b) After cleaning.

(c) Unused plastic tube.

Figure 3.9: Comparison of nanoparticle contamination in plastic tubes.

3.3 Thermometers

A PT-104 Platinum Resistance Data Logger was used to measure the temperature through four platinum resistance thermometers (called PRTs or Pt100s). The data logger provides a given resolution of 0.001°C and accuracy of 0.015°C [82]. The PicoLog 6 data logging software was used to acquire the measured data from the data logger.

Pt100 elements use platinum as the sensing material, and with perfect calibration, it has 100 Ohm resistance at 0°C. The relationship between temperature and resistance is nearly linear over a small temperature range. Documentation provided by the manufacturer indicates an 0.03°C uncertainty for the sensors [83]. Even though the Pt100 sensor offers excellent accuracy, there is a slight risk of self-heating due to the current going through the sensor. The data logger can therefore report an artificially high temperature if the sensor element is unable to dissipate this heat to its surroundings.

Before application, the four Pt100 temperature sensors were tested through the ice point calibration method [84], [85] to examine if there was any noticeable offset in the temperature measurements. The defined ice melting point (273.16K = 0.01°C at 1 atm) provides a useful checkpoint in verifying the condition of the sensors, as it is an intrinsic standard consisting of liquid water and solid water in thermal equilibrium. Also, by regularly checking the sensors by the ice point calibration method, a traceability chain is obtained, and potential drift in the temperature measurements can be observed.

The ice bath calibration procedure:

1 Preparation of an ice bath: The laboratory beaker was loaded with ice and tap water was filled about 80% to the top, to occupy the intervening spaces between the ice. An extra layer of ice was then added to the top to create a thermal buffer. When the ice started to melt, excess water was poured off, and new ice was placed on top. The ice bath was given sufficient time for the temperature to stabilise.

2 The Pt100 sensor was placed in the middle of the ice bath, as illustrated in Figure 3.10. For measuring the proper temperature, it was important for the sensor not to touch either the walls or the bottom of the container.

3 The temperature was recorded during the whole process from the sensor was inserted to thermal equilibrium with the ice bath.

4 The procedure was repeated for all four Pt100 temperature sensors.

The recorded data was processed after performing the ice bath calibration procedure for all four temperature sensors. Sensor 1 and 2, used for the DASC outlet and inlet temperature respectively, showed less than +0.04°C offset from the ice melting point after stabilisation. Sensor 3 (ambient temperature) showed $\sim$ 0.00°C, while sensor 4 (reservoir tank temperature) showed less than +0.05°C offset. No correction factors were applied to the sensor temperatures since the appropriate values would have been almost equivalent to the given uncertainty of the sensors. Nonetheless, the offsets can originate from several potential error sources, e.g. cables, connectors, and electrical conductors. Also, the temperature

Figure 3.10: Illustration of Pt100 thermometer verification procedure.

could have been unevenly distributed in the ice bath as a result of limited stirring during measurements.

During the experiments, sensor 1 and 2 were mounted on the system by a custom made insulating plastic cap and silicone in a tee-pipe section. The plastic cap covered the sensing part of the temperature sensors, and they were installed such that they would not absorb any radiation directly from the halogen lamp.

3.4 Laboratory irradiation source

For the laboratory setup, a Cotech 400W / 230 V floodlight halogen lamp with an Osram 400W /230 V R7S light bulb [86] simulated the solar irradiation of 2 Sun per m^2 during the experiments. To measure the radiative intensity (heat flux) of the beam in W/m^2, an LS122 Infrared Power Meter was used [87]. This particular instrument is limited to infrared radiation of spectral length $\lambda \in [1000, 1700]$ nm, which means that it may understate the total radiative intensity from the halogen lamp.

It is also useful to know to what degree the shorter wavelengths emitted from the halogen lamp correspond to the solar spectrum, $\lambda \in [250, 2500]$ nm. The previous research by Ulset [78] is illustrated in Figure 3.11, where the wavelength spectrum measured by a Ramses AAC-VIS radiometer from TriOS is compared to data received from Osram and the AM 1.5 standard spectrum. The Ramses radiometer detects radiation within $\lambda \in [280, 950]$ nm. By numerical integration of the values presented in Figure 3.11, it was found that the halogen lamp radiates 52.5% of short wavelengths to that of the Sun.

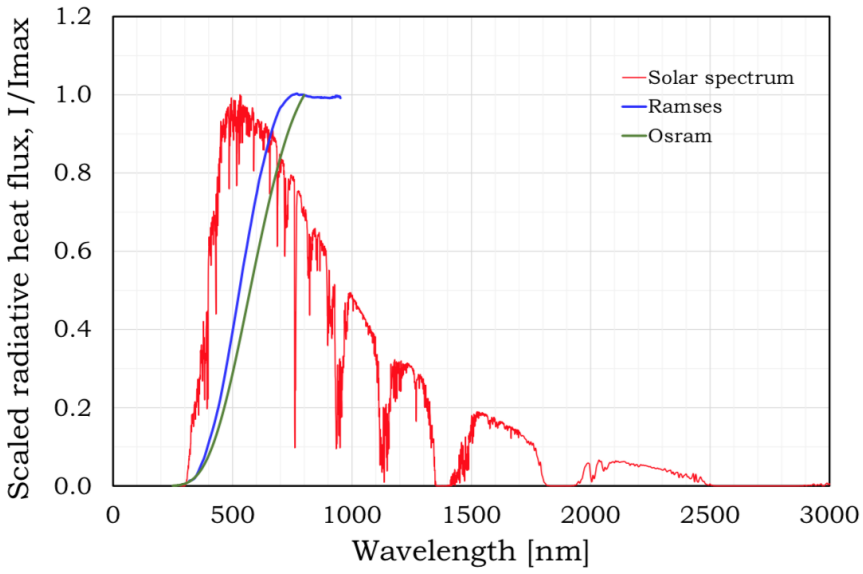

Figure 3.11: The solar spectrum compared to data from Osram and measurement by a Ramses radiometer [78].

A simple characterisation of the halogen lamp in question was done prior to the experiments. As revealed in Figure 3.12, the intensity of the beam was found to be unevenly distributed across the illuminated area. Consequently, the total radiative intensity on the DASC surface is expected to be lower than the value measured at the centre of the beam. To examine the lamps intensity distribution on the DASC surface, a paperboard was formed in the dimensions of the DASC surface on which three rows with five points were marked and carved out such that the LS122 Infrared Power Meter could measure the radiative intensity at each hole. The lamp was fixed 21 cm from the paperboard, delivering ~ 2000 W/m^2 at the centre of the beam. An average value was calculated based on three

separate measurements for each position.

For efficiency, a reduced number of measurements were carried out. Thus an extrapolation of the data was done to find the residual values at the surface edges. Figure 3.12 shows the estimated irradiation intensity distribution on the DASC. However, there are several potential error sources in this estimate, such as human error and inconsistency, as well as the uncertainty in the LS122 Infrared Power Meter instrument. It was therefore decided not to use this estimate in further calculations, though it is included in this thesis for illustration purposes. For simplicity, a heat flux of 2000 W/m^2 is therefore assumed at a distance of 21 cm from the halogen lamp frame (21.8 cm from the glass). The heat flux was measured with the LS122 Infrared Power Meter at the centre of the divergent beam.

The following procedure was used to centre the lamp underneath the DASC:

1. A paperboard was made in the dimensions of the DASC surface
2. The lamp frame dimensions were drawn on the centre of the paperboard
3. Two plumb lines were used on the DASC diagonal to mark the floor at its location. The paperboard was then taped to the floor.
4. The same procedure as in step 3 was used to fix the lamp position underneath the DASC.

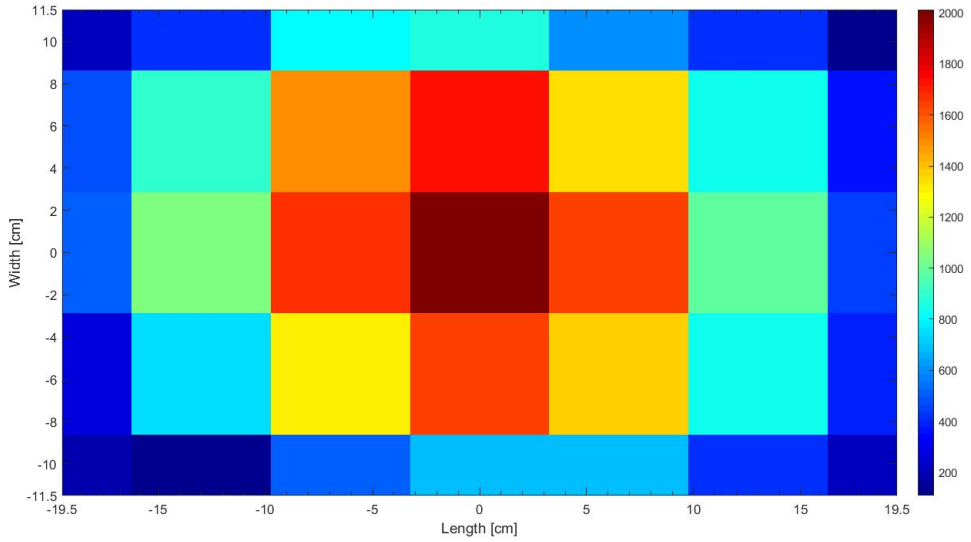

Figure 3.12: Diagram showing the intensity distribution in [W/m^2] on the DASC at a distance of 21 cm from the halogen lamp frame.

A custom bracket for the halogen lamp was mounted on the DASC frame, shown in Figure 3.13a. The purpose of the bracket was to make sure that the lamp always would be parallel to the DASC when fixing its tilt angle (turning the wheel on the left side of the green frame). The tilt angle is given as the angle between the direction of gravity, $\vec{g}$, and the

centerline of the collector. A digital protractor from Limit [88] was used to measure the angle of both the DASC and lamp before each experiment. The same digital protractor was also used to position the DASC on the green frame making sure that all corners of the DASC had the same angle relative to the floor.

(a) 15° tilt angle. (b) 180° tilt angle.

Figure 3.13: DASC laboratory experimental setup.

3.5 Experimental procedure

As previously discussed, the fluid (water or nanofluid) was continually circulated through the system prior to the experiments for two main reasons. It was done primarily to heat the system to a point near thermal equilibrium with its surroundings, and secondarily to diminish air bubbles in the system. The irradiation source (halogen lamp) was turned on right after the temperature logging was started.

During the experiments, all temperatures were sampled every 60 s, until the DASC inlet- and outlet temperature had achieved a steady-state condition. After stabilisation, the recording was continued for roughly 100 samples, as this provides adequate statistics for each experiment. The various experiments were only performed once if not otherwise is stated.

The calculated inlet- and outlet temperature difference was found from the relationship $\Delta \mathrm{T} = T_{outlet} - T_{inlet}$. Afterwards, the system was cooled to near-equilibrium temperature with the surroundings. The new experimental tilt angle or flow rate was then set, and the measurement process repeated.

3.6 Surrounding experimental environment

Due to the COVID-19 outbreak during the spring of 2020, the university campus was temporarily closed for both employees and students. The experimental setup was therefore moved from the laboratory at UiB to a smaller room in an office building as a contingency measure for the surface collector experiments. The spacing and ventilation conditions in the building in question were less than optimal, which increased the temperature changes in the ambient surroundings while experiments were performed.

The ambient temperature was prone to be affected by modest changes in the environment due to the small room size. The sun, heating the room through the window, local heating by the halogen lamp and the DASC, as well as variation in ventilation power, left observable effects on the temperatures during an experiment. As a consequence, the system was, at times, not able to reach the desired steady-state condition as expected. However, this is not critical for the collector performance, considering the inlet- and outlet temperature difference was more or less constant.

The setup was returned to the laboratory at UiB prior to the DASC experiments with water and nanofluid. The laboratory was larger than the office room. Thus, the ambient temperature displayed increased stability during the latter experiments. Due to the significant amount of heat being dissipated from the system during operation, the ambient held a near-constant temperature of 28°C while in equilibrium with the DASC system.

3.7 Nanofluid preparation

Several recent studies have highlighted the favourable characteristics of CB nanoparticles for harnessing solar energy [13], [89], [90], such as excellent absorption in the whole wavelength of sunlight. Even a minuscule weight percentage of the particles, like 0.05wt%, has proven to absorb nearly all incident radiation for a film thickness of 9 mm [91]. Experimental data regarding thermal properties of CB nanofluids also show a near-linear correlation between nanofluid thermal conductivity and an increase in the amount of CB nanoparticles [13]. In this thesis, nanofluids infused with 0.05wt.% Timcal 350G Carbon Black were used to investigate DASC efficiency and performance, related to the previously discussed benefits in Chapter 2.1.1. These particles were within the range [15, 95] nm with an average size of 51.1 $\pm$ 17.0 nm [78], found by a SEM and TEM characterisation.

Distilled water was chosen as the preferable base fluid because of its favourable properties such as high heat capacity and low viscosity. 10% ethanol was added [10] to lower the freezing point of the nanofluid and allow potential outdoor utilisation in cold environments. In a study of carbon-based nanofluid optical properties, Gan and Li [89] observed satisfactory suspension stability for nanofluids where ethanol served as the base fluid. Moreover, as discussed in Chapter 2.1.2, the addition of SDS to nanofluids results in a stronger electrostatic repulsion between the nanoparticles, which reduces the development of particle agglomerates and thus bolsters stability. The amount of SDS used in this project is based on previous experimental research by Taylor et al. [19] and Hwang et al. [92]. They showed that 1 wt.% SDS improves the stability of carbon nanofluids. A small quantity, 0.0002 wt.%, of copper(II)Sulphate ($CuSO_4$) was also added to reduce the risk of algae or moulds formation in the nanofluid [10]. 0.5wt% FoamStop [93] from Kärcher was later found to be a necessary component to prevent the production of foam in the reservoir tank, an issue that is discussed further in Chapter 4.3.3. A summary of the different nanofluid components is found in Table 3.4.

Table 3.4: Summary of nanofluid components.

Component	Producer	wt.%
Ensaco 350G Carbon Black	Timcal	0.05
Distilled water	-	88.4498
Ethanol 96 % vol	VWR	10
SDS	Sigma Aldrich	1
FoamStop	Kärcher	0.5
$CuSO_4$	-	0.0002

Due to its straightforward procedure, 10 kg of nanofluid was prepared using the two-step method, as presented in chapter 2.1.1. Each component was measured by mass percentage using a Sartorius CPA 324S balance. The components were carefully stirred before sonication in a Branson 3510 Ultrasonic cleaner for 1 hour to deagglomerate particle

clusters and to obtain a homogenous suspension. Previous studies [92] have shown that there is no appreciable change in suspended particle morphology with more than 1 hour sonication time. Due to the ultrasonic bath volume limitation, the nanofluid had to be sonicated in batches of equal concentration and subsequently mixed in a larger container and then sonicated for 1 hour afterwards, to mix the smaller batches sufficiently.

Moreover, since the nanofluid consist of nearly 99wt.% base fluid (distilled water + ethanol), it can be argued that the remaining mass, consisting of nanoparticles, SDS, and $CuSO_4$, has an insignificant contribution to resulting nanofluid density and specific heat. Accordingly, these nanofluid properties are assumed to be equal to that of the base fluid when later calculating volumetric heat generation efficiency of the solar collector using the formulas provided in Chapter 2.5. The thermophysical properties, specific heat and density, are calculated as mean values for the actual temperatures of the collector, given for three different cases:

(i) Surface collector + water with operating temperature interval [28,35]°C

(ii) DASC + water with operating temperature interval [41,45]°C

(iii) DASC + nanofluid with operating temperature interval [46,52]°C

The operating temperature intervals are found and generalised from the temperature history plots which are presented in Appendices C, D, and E.

3.8 Evaluation of nanofluid stability

A simple evaluation of the nanofluid stability was necessary, considering uncertainty related to the extra step when subsequently mixing several smaller batches, as in the preparation method presented in the previous chapter. The particle size distribution (PSD) of a diluted solution can be obtained by the method of static light scattering (SLS). Fundamentally, SLS is a technique based on the relationship between particle size and the angle and intensity of scattered light. For example, light scatters more intensely and at smaller angles off larger particle sizes. A review of nanofluid stability by Chakraborty and Panigrahi [94] supports that PSD acquired at different time intervals over a long period has been successfully used to indicate nanoparticle agglomeration tendency. Therefore, SLS analysis can reveal an increase in particle size with time due to agglomeration, and thus act as an indication of instability. In combination with the PSD, a visual inspection of the nanofluid container bottom surface can reveal possible sedimentation of nanoparticles.

The SLS device used in this work is the Malvern Mastersizer 2000 with an Analysette NanoTec Fritsch 22 laser. The instrument can detect particle sizes within the range [0.01, 2100] µm. Mastersizer 2000 applies Mie theory to predict the scattering of what is presumed to be spherical particles. The prepared nanofluid samples were dispersed in filtered tap water and kept in suspension by a mechanical stirrer. A cover protected the dilution from being contaminated by dust in the air.

Even though performing an SLS measurement is a rather straightforward method, some minor disturbances and issues can influence the results significantly. As a result of sonication or cavitation within the circuit, bubbles circulating among the particles can occur. These bubbles may contribute to the scattering of the incident radiation and be interpreted as particles which distort the resulting PSD. As an effort to limit bubble formation, the stirrer speed and the internal pumping power were controlled carefully. A numerical study by Lo and Zhang [95] found that bubbles in such a flow occur in millimetre-scale. Nanoparticles, however, are unlikely to be of such sizes, even those of agglomerates [30]. Thus limitation of the PSD size range can effectively solve this problem. Nevertheless, this approach must be chosen with great caution, as not to exclude actual particles. Moreover, the model dependency, when calculating the PSD from the scattering data, is another potential issue that must be noted. For instance, some models are based on assumptions of particle characteristics such as opacity and shape [30], which is very likely to influence the accuracy of the results.

For the nanofluid stability analysis, three reference nanofluid samples were prepared according to the composition presented in Table 3.4. $CuSO_4$, however, was not added because of the small mass associated the total sample size of 50 - 100 g. It must be noted that when performing the SLS analysis, the method for calculating the PSD uses only the refractive index for water as the carrier fluid, and does not consider 10wt.% ethanol. As previously mentioned, the nanofluid is highly diluted in water before examining the PSD, which makes the ethanol a minor component and its referactive index impact minimal.

The SLS analysis was performed immediately after sonication of the three samples. After that, samples 2 and 3 were mixed, sonicated for an additional hour, and finally analysed

by SLS once more. When performing an SLS analysis, three measurements were done each time, so that the PSD results presented in Chapter 4.3 are based on a calculated average. The process was repeated for the final two samples (1 and 2+3) after one day, and finally after one week.

Two nanofluid samples were also collected from the reservoir tank of the same nanofluid. Sample TANK1 was collected before operation of the DASC and analysed by SLS shortly after, and a second time after seven days. In addition, a sample, TANK2, was collected after seven days of operation. It is estimated that the nanofluid in the reservoir tank was subjected to repeated heating around ten times when sample TANK2 collected.

To summarise, the method objective was to investigate if nanofluids behave differently and become unstable if they are subject to mixing, circulation and heating. The PSD measurement results are presented either as volume or number frequencies. For most nanoparticles, the sizes are normally distributed and presented as a differentiated function $f(d)$:

$$f_n(d) = \lim_{\Delta d \to 0} \frac{\bar{f}_{n(d)}}{\Delta d}, \tag{3.2}$$

where $\bar{f}_n(d)$ is the frequency of particles with diameter d. In terms of volume frequency, $\bar{f}_n(d)$ is the volume fraction of particles with diameter $d \in [d_i, d_{i+1}]$. It must be noted that the larger particles in the distribution dominate PSD based on the volume frequency. A large abundance of small particles will, therefore, be less dominant as they occupy a relatively small amount of space despite being numerous. As a result, the PSD may not give an accurate impression of the actual size distribution. For this reason, the PSD results are this current work is presented in terms of number frequency.

Chapter 4

Results and Discussion

This chapter presents the results from three experimental cases related to collector efficiency, followed by a comparison of the various data, and a short review of complications related to the DASC construction. Finally, an analysis of nanofluid stability is performed and discussed.

The experimental data are best visualised through linear or polynomial equations to provide the characteristic performance parameters of the collector for different volumetric flow rates and tilt angles. The obtained trend line can provide useful predictions about DASC behaviour past the current boundaries for this study. It must be noted that the trend line is given as an illustration only and that it might deviate from experiments with high numbers of data samples and smaller uncertainty numbers. Error bars for data points are also shown in the figures displaying the calculated efficiencies. Tables presenting all the calculated experimental results are found at the end of each respective sub-chapter. The uncertainty equations are presented in Appendix A.

4.1 Surface collector experiments

As the laboratory experiments for the surface collector were taking place in a small office location, the hallway door had to be kept open. A small fan - directed so that it would not blow directly at the DASC - circulated the air in an attempt to minimise the rise in the ambient temperature during the experiments. Despite these efforts, it was apparent from the initial measurements that the halogen lamp, as well as the DASC itself, was heating the small room. This became evident by a continuous increase in the ambient temperature during the experiments. This effect can be easily be spotted in several of the recorded temperature history plots, which are found in Appendix E. The surface collector experiment with 45° tilt angle and flow rate of 2.3 L/min was conducted twice. The first result showed a very sudden change in efficiency for a rather small change in flow rate, which could indicate some disturbance of the collector during the experiment. Nevertheless, both results confirmed the same trend and are included in the final result discussion.

As an effort to minimise the rise in ambient temperature, trials were conducted with windows open. However, wind gusts caused fluctuation in all temperature records, which can be seen in Figure 4.1. Even though wind gusts might be more akin to the normal working conditions of a solar collector, the current work did not aim to replicate such an environment. Hence, it was decided to have the window closed during the subsequent experiments to produce consistent data under repeatable and predictable conditions.

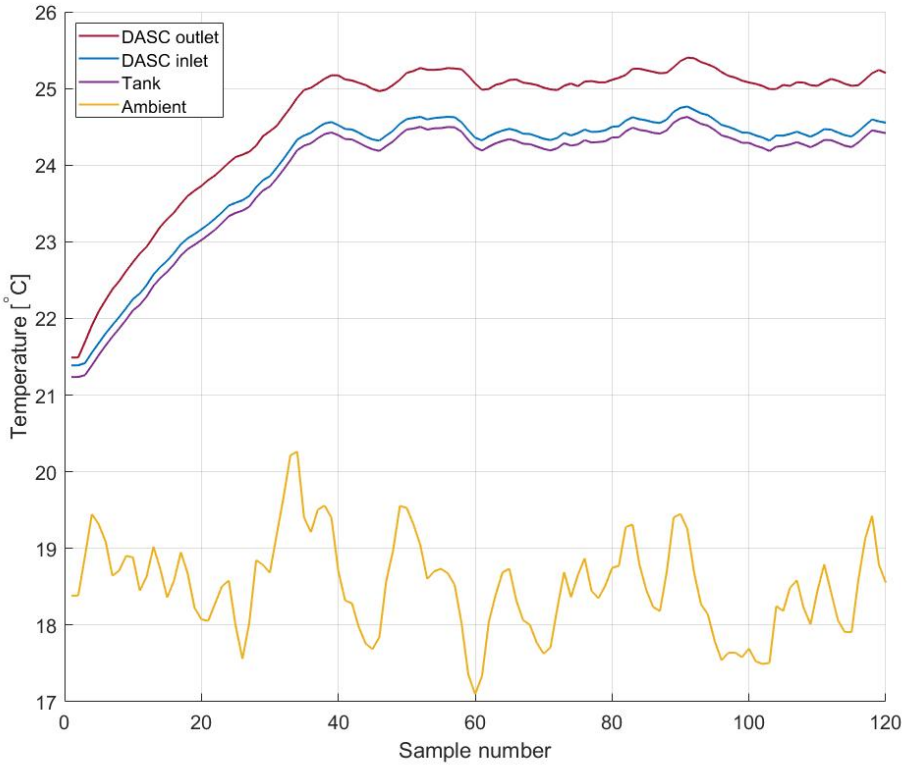

Figure 4.1: Temperature history plot for the surface collector affected by wind gusts.

4.1.1 Effect of flow rates

In theory, higher fluid velocities (volume flow rates) in a solar collector system usually lead to increased convective heat transfer. Higher flow rates cool the collector walls and surface effectively, thus reducing heat loss to the surroundings. In addition, Zhou et al. [96] explain that for surface collectors, higher inlet flow rates will also enhance the heat transfer coefficient between the absorber plate and the working fluid. On the other hand, lower flow rates promote the absorption of heat from the hot surface. The increased fluid residence time within the collector increases the temperature at the collector outlet. However, minimal flow rates lead to overheating of the collector surface, thermal layering of the flow, and increased heat loss to the surroundings [27]. To summarise; an optimal flow rate is achieved when the absorption of heat by the fluid volume is balanced with

minimum heat loss from the surface, hence maximum collector efficiency.

As discussed in Chapter 3.2.1, the range of flow rates to be investigated for the surface collector experiments was limited due to restricted pumping power and tube dimensions. Consequently, the optimum flow rate could not be expected to be within the experimental conditions for the surface collector. Ideally, all experimental cases should have had the same conditions so that the respective collector performance can be compared over the whole range of flow rates. Moreover, the difference in the fluid inlet and outlet temperature was expected to decrease with increasing flow rates. The experimental results at all four tilt angles, 0°, 15°, 45°, and 180°, presented later in Table 4.1, are all consistent with this theory.

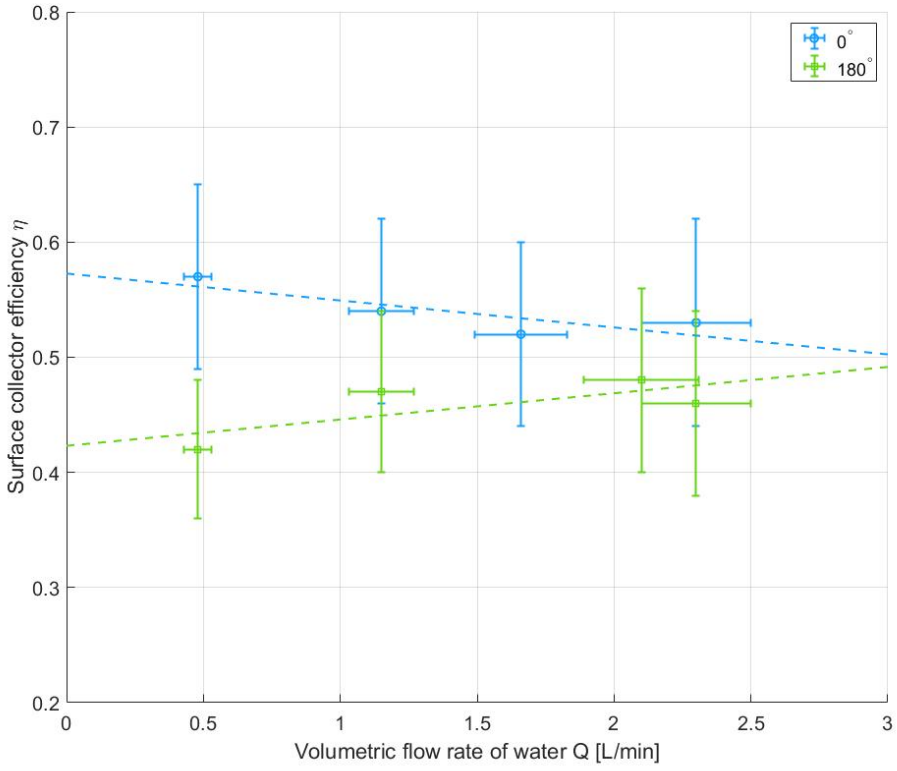

Figure 4.2: Experimental efficiency of surface collector with tilt angle of 0° and 180°.

Contrary to the anticipated effect of higher flow rates in solar collectors, Figure 4.2 suggests that there is a slight decrease in the efficiency for rising flow rates when the surface collector is oriented with an incline of 0° relative to the horizontal. Considering that the heat loss is caused by large temperature gradients between the collector and the surroundings, smaller or moderate temperature gradients may benefit from lower flow rates. The value of increased absorption time inside the collector may surpass the effect of the heat loss to the surroundings. From the figures in Appendix C it can be seen that the system's

operating temperature is barely (∼ 6-8°C) higher than the ambient temperature, which is contrasts to the high operating temperatures that will be discussed later for the water and nanofluid DASC system. Furthermore, the trend line for 0° tilt angle in Figure 4.2 may give a misleading impression of a decrease in efficiency at higher flow rates. If one considers the error margins of the results, rising flow rates can also result in a positive effect or no effect at all on the final efficiency of the surface collector for this case. Due to a high degree of uncertainty, it is not possible to come up with an unambiguous conclusion.

The higher efficiency can be explained by the convection effects that are present in the fluid. The heat transfer within the fluid occurs mainly by combined natural and forced convection. The natural convection is due to the temperature gradient within the fluid, while the circulation by the pump causes forced convection. For lower flow rates, the effect of natural convection is more significant due to increased heat exchange with the surface. However, as the flow rate increases slightly, the forced convection surpasses the natural convection effects and the heat exchange with the surface absorber are somewhat reduced.

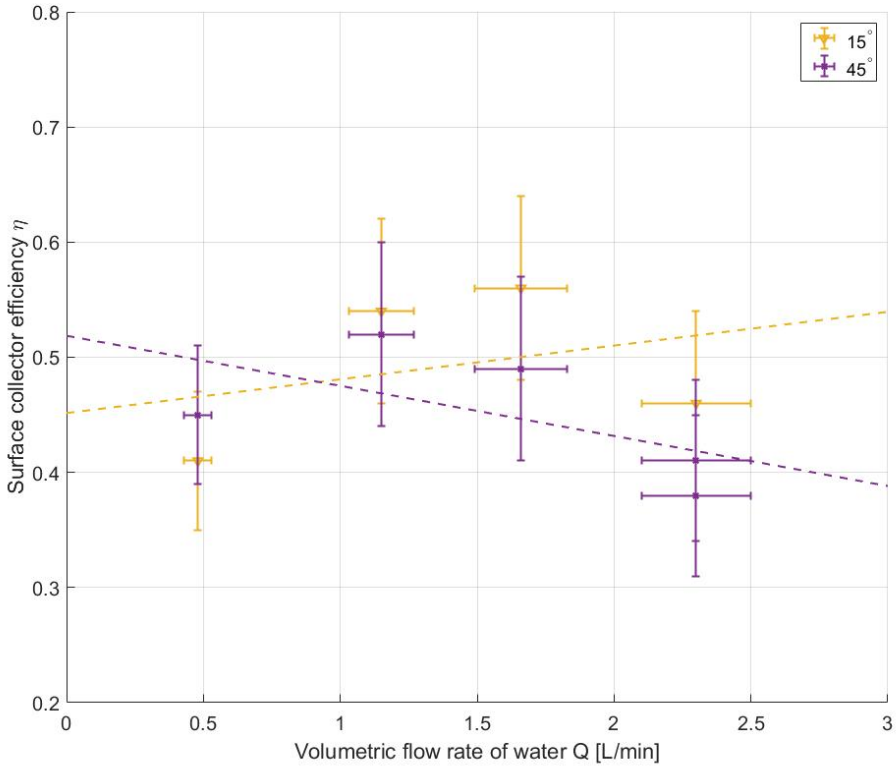

Figure 4.3: Experimental efficiency of surface collector with tilt angle of 15° and 45°.

A final element that should be considered is the natural convection arising from the halogen lamp. This heated air may be 'trapped' underneath the horizontal DASC when it is tilted at a 0° angle, which then in combination with the absorbed radiation overheats the surface.

As a consequence of the trapped hot air, the energy loss from the heated surface may almost be eliminated. Thus, lower flow rates might become more advantageous for such cases due to the increased absorption at the hot surface. The trapping of the heated air is absent when the surface collector is oriented with a 180° tilt angle. Hence, it is reasonable to expect lower efficiencies for this angle compared to other angles. This outcome can be seen in Figure 4.2, where a 0° tilt angle consistently achieves higher efficiency at each flow rate compared to 180°.

The efficiency change of the surface collector operating with 15° and 45° tilt angle does not follow the anticipated rise for higher flow rates at either tilt angle. A possible reason is that the optimum flow rate exists within the examined range of flow rates. Thus the efficiency will start to decrease when passing the ideal flow rate, which can be observed in Figure 4.3. For such cases, the predicted linear increase in flow rates by the trend line will be misleading. On the other hand, since the entire range of studied flow rates is limited, the efficiency behaviour may shift and start to increase for higher values.

4.1.2 Effect of tilt angles

Figure 4.11 summarises the surface collector efficiency achieved at each tilt angle for the various flow rates in one plot. The results show that 0° is the most beneficial surface collector tilt angle for heat generation efficiency, followed by a 15° tilt angle. 45° and 180° is the least advantageous tilt angles, possibly due to reduced or absent additional natural heat convection from the halogen lamp. Additionally, when the hot surface absorber is located underneath the bulk fluid, the natural convection inside the fluid is elevated due to gravity. The heated fluid which is in contact with the surface absorber will move upwards naturally and diffuse into the cooler layers of water located above. This effect decreases when the hot surface is located above the fluid. Consequently, the natural convection effects within the bulk fluid are expected to be at a maximum for when the solar collector is oriented at 0° tilt angle.

Though similar in behaviour, a different slope describes the collector efficiency when the flow rate increases for 15° and 45° tilt angles. This can be seen in Figure 4.3. However, the collector generally achieved higher efficiency at when oriented at 15° tilt angle compared to 45° tilt angle, which can be seen in Figure re. Sekhar et al. [97] found that a variation in tilt angle from 20-60° had an insignificant impact on the top loss coefficient, which is a measure of the radiative and convective heat loss from absorber plate to the surroundings. It can therefore, be argued that 15° tilt angle achieved higher efficiencies mainly due to the increased trapping of the heated air from the halogen lamp.

4.1.3 Design analysis

Figure 4.5 displays an image taken by a FLIR E8 infrared camera and shows the temperature of the surface collector under an experimental case with 0° tilt angle and a flow rate of 0.48 L/min. The temperature appears to be higher on the baffle located at the centre of the collector. The baffle itself or the underlying plate may have a local height variation which makes room for a small amount of water to be trapped, which then becomes

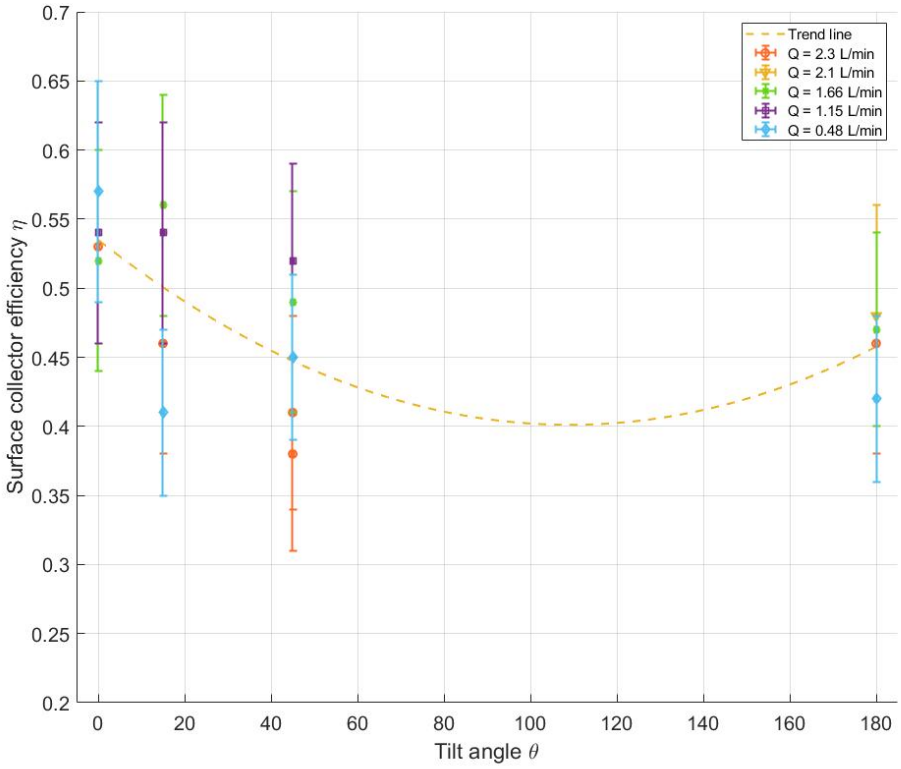

Figure 4.4: Experimental efficiency of the surface collector with varying tilt angle.

extensively heated when illuminated. A higher temperature can also be observed on the aluminium outer box and its edges, which is natural due to the extremely high thermal conductivity of aluminium. Furthermore, there can be observed some thin horizontal yellow lines. These lines are possibly due to poor thermal contact between the tape and the glass, or perhaps some overlap between the parallel layers of tape.

Lastly, the performance of the surface collector used in this experimental study is compared to that of a commercial surface collector [98]. Figure 4.6 shows the efficiency of the two surface collectors plotted against the reduced temperature, $T_m^* = (T_f - T_a)/G$ where T_f is the fluid temperature, T_a is the ambient temperature, and G is the solar irradiance. The relationship $(T_f - T_a)$ for the surface collector in this experimental study was 6-7°C. The commercial surface collector is predicted to operate with very high efficiency due to the low temperature gradient to its surroundings. However, a large gap can be observed between the commercial and the experimental surface collector efficiency. This indicates that the method described in Chapter 3.1 was not adequate to obtain the desired surface collector performance. Also, as described above, the efficiency may be affected by poor thermal contact between the duct tape and the glass.

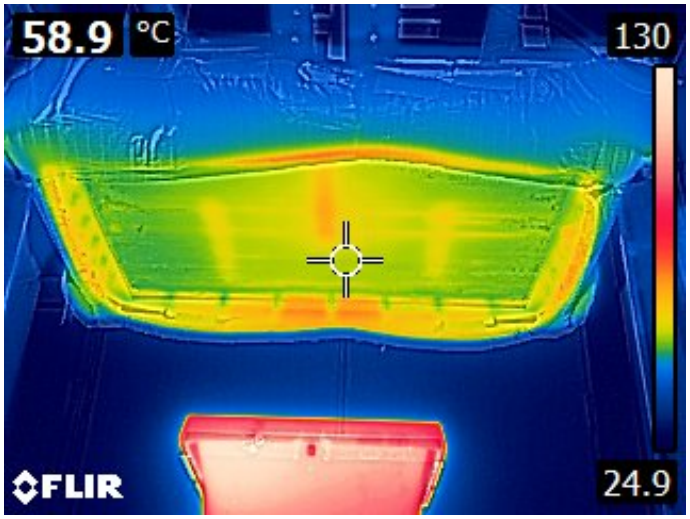

Figure 4.5: FLIR infrared photo of surface collector with 0° tilt angle and $Q = 0.48$ L/min.

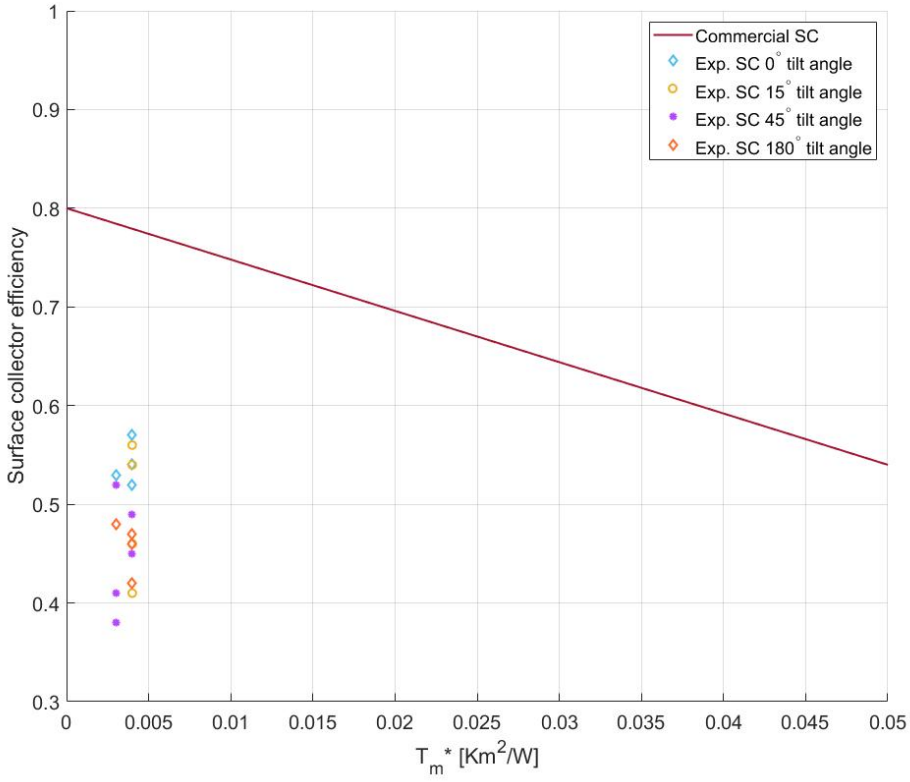

Figure 4.6: The experimental results for the surface collector compared to the efficiency of a commercial surface collector [98].

Table 4.1: Summary of experimental results for surface collector.

Tilt angle 0°

Volumetric flow rate Q [L/min]	SD of the mean ΔT [°C]	Efficiency η	Mean ambient T [°C]
0.48	3.085 ± 0.002	0.57 ± 0.08	22.8
1.15	1.217 ± 0.008	0.54 ± 0.08	23.9
1.66	0.819 ± 0.012	0.52 ± 0.08	23.5
2.3	0.591 ± 0.008	0.53 ± 0.09	23.9

Tilt angle 15°

Volumetric flow rate Q [L/min]	SD of the mean ΔT [°C]	Efficiency η	Mean ambient T [°C]
0.48	2.232 ± 0.008	0.41 ± 0.06	24.4
1.15	1.213 ± 0.017	0.54 ± 0.08	24.8
1.66	0.870 ± 0.006	0.56 ± 0.08	25.1
2.3	0.515 ± 0.006	0.46 ± 0.08	24.5

Tilt angle 45°

Volumetric flow rate Q [L/min]	SD of the mean ΔT [°C]	Efficiency η	Mean ambient T [°C]
0.48	2.445 ± 0.003	0.45 ± 0.06	25.4
1.15	1.165 ± 0.002	0.52 ± 0.08	24.3
1.66	0.759 ± 0.012	0.49 ± 0.08	23.5
2.3	0.417 ± 0.008	0.38 ± 0.07	25.8
2.3	0.455 ± 0.004	0.41 ± 0.07	24.3

Tilt angle 180°

Volumetric flow rate Q [L/min]	SD of the mean ΔT [°C]	Efficiency η	Mean ambient T [°C]
0.48	2.247 ± 0.002	0.42 ± 0.06	25.7
1.66	0.726 ± 0.005	0.47 ± 0.07	24.2
2.1	0.597 ± 0.004	0.48 ± 0.08	25.0
2.3	0.515 ± 0.012	0.46 ± 0.08	27.1

4.2 DASC experiments with nanofluid and water

One of the main objectives of this study was to investigate how the orientation of the nanofluid column in the field of gravity influences the DASC performance. The efficiency of the DASC operating with both water and nanofluid at equal tilt angles are plotted in the same figures to provide a simple visual comparison. A discussion of various challenges encountered during the experiments is also given. The figures displaying the temperature history plot under the different experimental cases for both nanofluid and water can be found in Appendix D and E. The ambient temperature is omitted due to graph scaling in order to highlight the inlet- and outlet difference.

The tilt angles were investigated sequentially so that all flow rates for the 0° tilt angle were investigated first, then 15°, 45°, and finally 180°. The last experiment with nanofluid with a 180° tilt angle and a flow rate of 4 L/min was not conducted due to permanent incapacitation of the heat exchanger. All experiments with water were completed before converting to nanofluid in the setup. Since the tested temperatures of the fluids never exceeded 60°, vapour formation was unlikely to form in the experiments. This minimises the risk of vapour distorting the optical properties of the nanofluid.

4.2.1 Effect of flow rates

Similar to the surface collector, increasing the flow rate of water in a DASC system generally leads to higher efficiency since it reduces the heat loss from the system to the surroundings. However, this effect is somewhat mitigated due to the volumetric absorption principle. For a volumetric absorber, the heat is released within the fluid volume. Eggers et al. [27] explain that most of the incident radiation absorbed by the fluid volume is transformed into enthalpy (sum of internal energy and the product of pressure and volume) close to the walls, where the average flow rate is lower than in the centre of the collector. This results in a temperature spike near the walls. Higher flow rate leads to higher Reynolds number and thus increased turbulence in the system. Increased flow rate and turbulence will enhance the heat transfer as well as improve the equalisation of temperature among the absorber walls. However, since this system operates over a range of relatively low flow rates (i.e. laminar flow is anticipated), turbulence effects are assumed to be limited.

On the other hand, very low flow rates leads to temperature layering by natural convection effects. This is unwanted, as it would result in higher temperatures at the surfaces and increased heat loss. From another frame of reference, the rate of heat transfer within the nanofluid is also enhanced by increased relative flow rate between the nanoparticles and the base fluid [46]. Secondary effects, such as particle agitation and mixing, are also expected to make an additional contribution to the collector efficiency when the flow rate is increased.

The results in Figure 4.7 and Table 4.2 suggest a slight increase in efficiency when the flow rate rises from 2-3 L/min for the nanofluid DASC when oriented with a 0° tilt angle. However, the flow rate is constant in the intervals between 1-2 L/min and 3-4 L/min. It

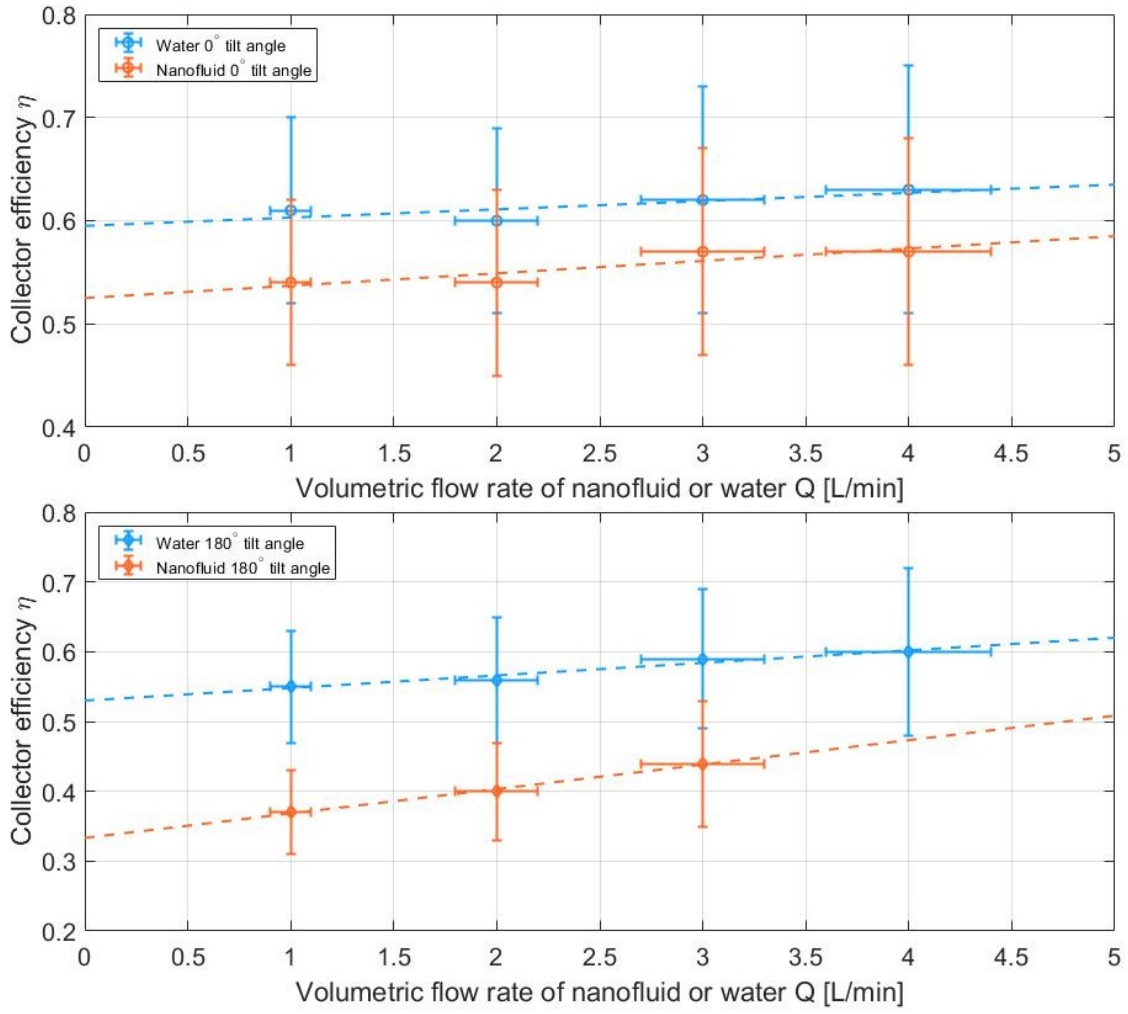

Figure 4.7: Experimental efficiency of the DASC with 0° tilt angle on the upper plot, and with 180° tilt angle on the lower plot.

is therefore reasonable to either predict a somewhat positive, or neutral behaviour, for further increasing flow in this case when considering the uncertainties of the results.

The steepest incline in collector efficiency for rising flow rate is observed in Figure 4.7 for the nanofluid DASC with 180° tilt angle. This can possibly be credited to a significant reduction of heat loss from the DASC when the flow rate rises, as well as increased forced convection within the nanofluid. Since the collector is oriented with the transparent surface facing upwards, larger heat loss is expected due to natural convection. Therefore, when the flow rate is increased, the heated fluid will pass the surface (which is exposed to the ambient temperatures) more quickly, thus reducing the heat loss efficiently. Furthermore, nanoparticle deposits were observed on the transparent surface during these experiments (which will be discussed in more detail later). This may have altered the volumetric absorption properties in the DASC to behave as a surface collector with indirect absorption,

which is detrimental for collector efficiency, especially at lower flow rates. Finally, the efficiency for the DASC with water also increases with rising flow rate for both 0° and 180° tilt angle, which was expected due to reduced heat loss.

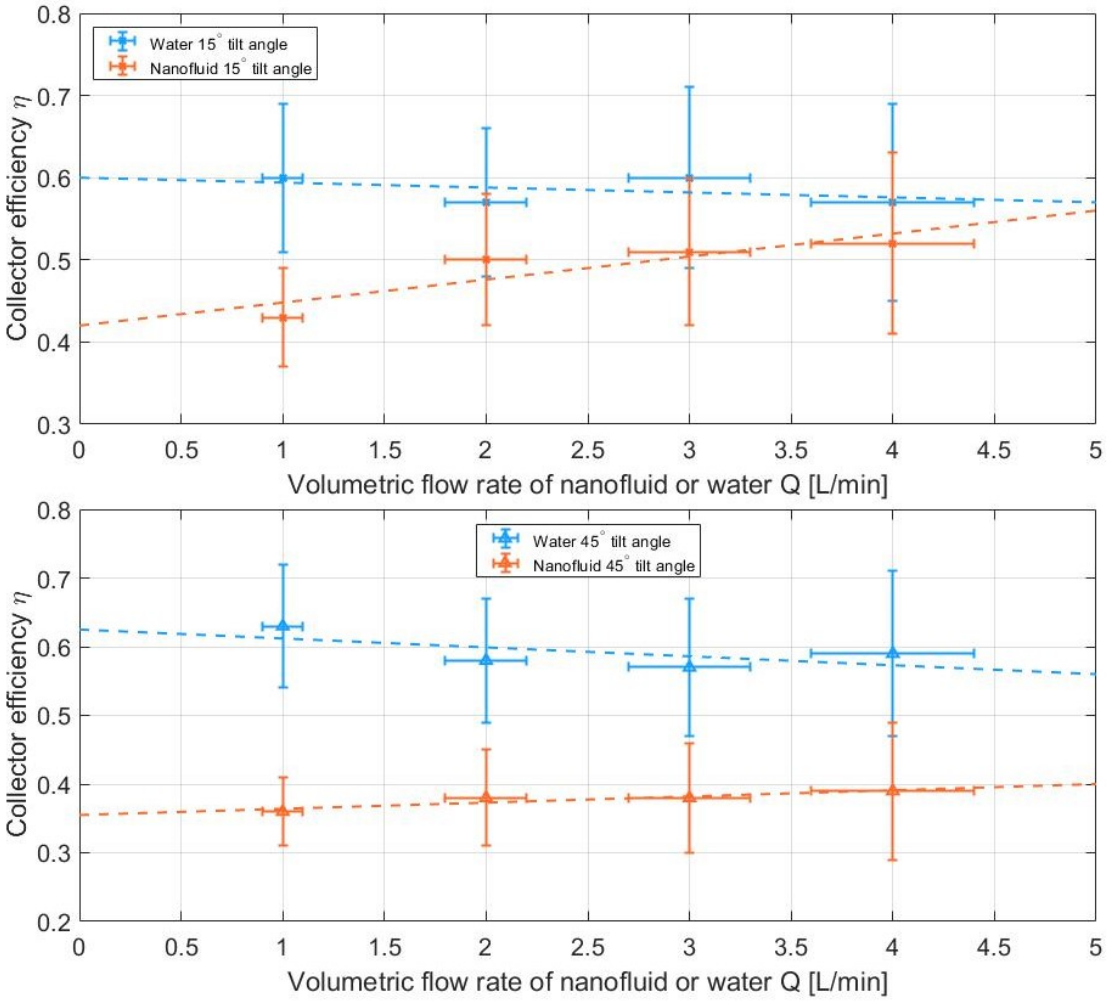

Figure 4.8: Experimental efficiency of the DASC with 15° tilt angle on the upper plot, and with 45° tilt angle on the lower plot.

Figure 4.8 shows that the collector efficiency increases with rising flow rate for nanofluid DASC, when oriented with both 15° and 45° tilt angle. The most noticeable jump in collector efficiency ($\sim 7\%$) was observed when adjusting the nanofluid flow rate from 1-2 L/min for the 15° tilt angle. Moreover, the increase in efficiency is very modest for the nanofluid DASC 45°. This is similar to the result when oriented with a 0° tilt angle. The DASC with water at 15° or 45° tilt angle, however, showed slightly different behaviour than for the nanofluid. When oriented with 15° tilt angle, the increased flow rate resulted in a somewhat fluctuating performance of the collector. Also, the 45° tilt angle gave a concave-like trend for the collector efficiency, with a minimum at 3 L/min. This is opposed

to the linear fit that was predicted in the plot. Nonetheless, since the variation in efficiency is very small for both of the above cases for water, it is difficult to predict a definitive behaviour of the collector past the measured flow rates.

The temperature difference between the DASC inlet and outlet increases with decreasing flow rates for each tilt angle, for both nanofluid and water. This can be seen in Tables 4.2 and 4.3. This is due to prolonged residence time within the DASC, i.e. a given fluid volume will have increased time to absorb radiation from the halogen lamp. However, the temperature difference is much more prominent for water than for nanofluid. The water achieved considerable higher temperatures at the collector outlet than what the nanofluid did for all cases.

To summarise, the results in Figures 4.7, and 4.8 indicate that the DASC efficiency increases with an augmentation in flow rate for all tilt angles. Furthermore, this effect is more prominent for nanofluid compared with the results for the same system with water. This corresponds to the behaviour observed by both Eggers et al. [27] and Gupta et al. [74] in their studies concerning the influence of nanofluid flow rate in a DASC system.

4.2.2 Effect of tilt angles

Figure 4.9 displays the variation of thermal efficiencies achieved for the nanofluid DASC at the different tilt angles. The curves suggest that the highest efficiency is obtained when the DASC is oriented with an 0° tilt angle, also referred to as a case of reverse illumination. These results are in good agreement with previous research done by Balakin et al. [28] and Wang et al. [29]. Both papers suggest that the enhanced efficiency of the reversed illuminated DASC can be expected due to a phenomenon called Rayleigh-Bérnard convection. Rayleigh-Bérnard convection is buoyancy-driven natural convection. When the fluid is heated from below, a pattern of upwards floating force is formed. The nanoparticles are then forced to move upwards, and macroscopic convection within the nanofluid is created. An illustration of this event, Figure 1.7, has been presented in Chapter 1.2.

Furthermore, Balakin et al. propose that an increasing tilt angle will reduce the convective pattern until a minimum is reached at around 90°. This seems to be consistent with the concave-shaped trend line in Figure 4.10, which approaches a minimum efficiency approximately at a 90° tilt angle. However, it is difficult to be definitive since there are no experimental data points for this study for tilt angles in the range between 45-180°. Moreover, a difference can be seen for the behaviour after the 90° threshold. In the study by Balakin et al., the collector efficiency increases to a point where 180° tilt angle is preferred compared to 45°. This distinction is less noticeable in the current results, as seen in both Figure 4.9 and 4.10. Finally, the authors found that the 0° tilt angle gave a ∼9% higher efficiency compared to the 180° tilt angle. In this experimental study, however, the gap in efficiency between the two cases was ∼16%. On the other hand, it must be noted that the error margins are quite large and that the above value is based on a calculated trend line. Hence the gap could be smaller, or even more significant, in reality.

The differences mentioned above may be explained by an unstable nanofluid, where the

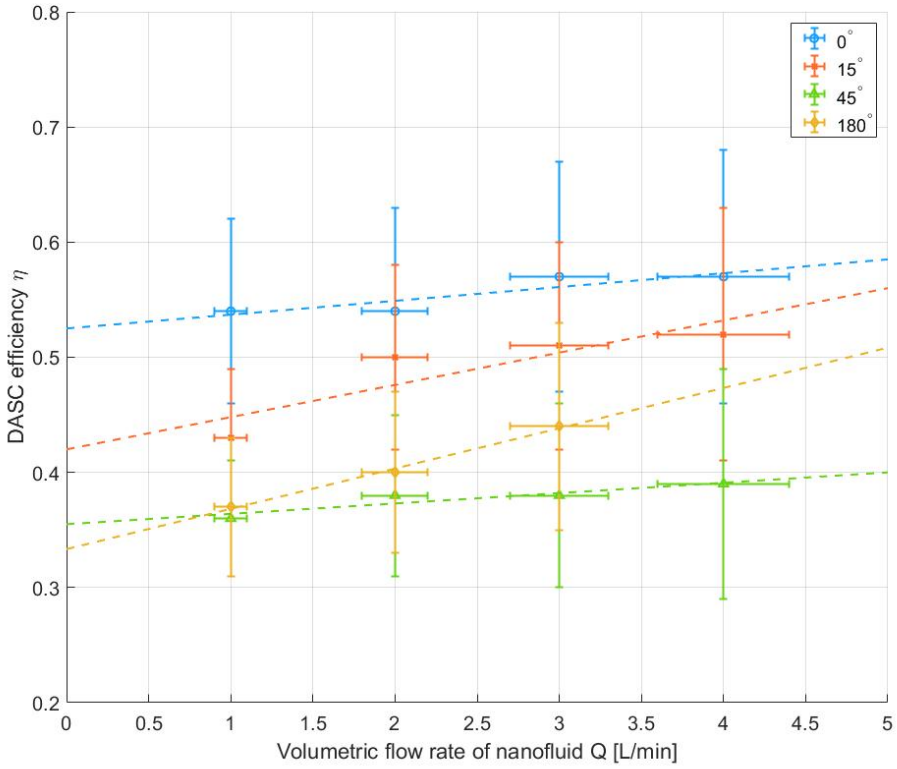

Figure 4.9: Experimental efficiency of nanofluid DASC with varying volumetric flow rate.

particle concentration is declining with time, or possibly by the leakage from the DASC. The leakage for the setup worsened progressively for each experiment, especially for higher flow rates, as seals became untight. Therefore, the quantity of nanofluid leaking from the DASC during an experiment was more significant for the final experiments with the 180° tilt angle, than for the earlier experiments. Consequently, these final experiments were subject to a more substantial disturbance. This problem is discussed further in Chapter 4.2.3.

The general heat generation efficiency of the DASC with water is barely above 60% when oriented with an 0° tilt angle. The change in efficiency when increasing the tilt angle up to 45° is only minimal. At 180° tilt angle, however, the efficiency is slightly reduced to right below 60%, which can be seen in Figure 4.11. Nonetheless, these changes are very small and are most likely a result of the increased heat loss from the DASC surface. However, were it not for the absence of particles within the fluid, these results would probably be more like those observed in Figure 4.10, which shows that the different tilt angles affect the convection between the nanoparticles and the base fluid. For water, such additional convection effects are not present.

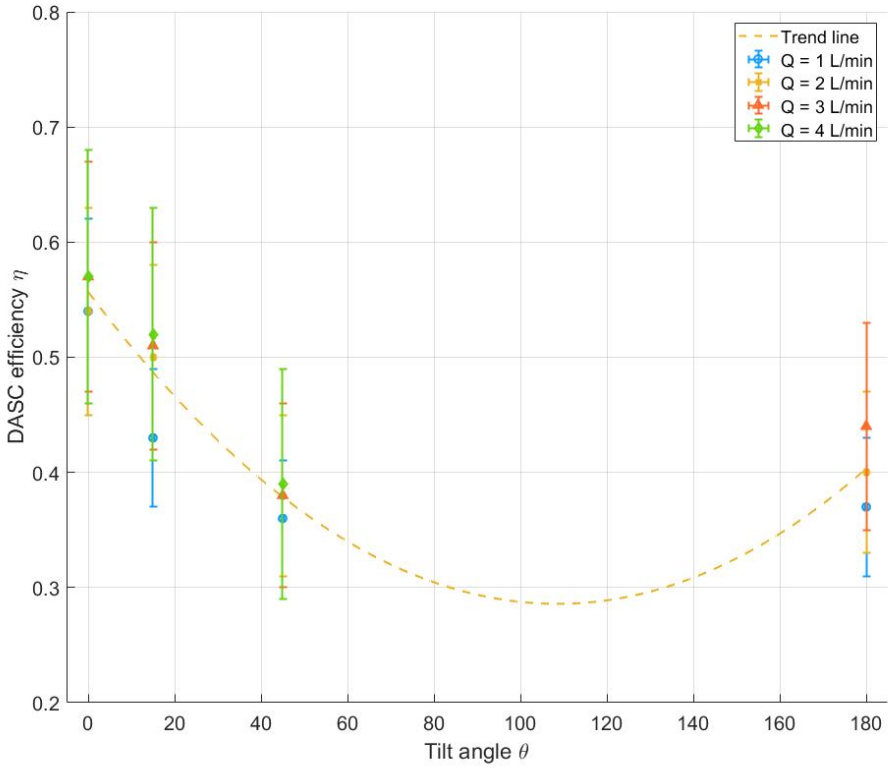

Figure 4.10: Experimental efficiency of nanofluid DASC with varying tilt angle.

4.2.3 DASC design analysis

The enhanced thermal and optical properties of nanofluids have received a great deal of attention from the scientific community. Many researchers [20], [21] have suggested that nanofluids can be the solution to overcome low photothermal efficiencies currently associated with solar collectors. The results from this study, however, presents an additional perspective that requires attention before DASCs with nanofluids can be commercialised. The prevailing trend in the experimental results, in previously presented Figures 4.7 and 4.8, suggests that water is the superior choice of working fluid in the DASC for every flow rate.

There may be several possible reasons why the DASCs in these experiments yields such low efficiency for the nanofluid. As both the properties of the nanofluid and the various design choices of the DASC might affect the flow rate, both must be considered as possible sources of flaw. During the initial experiments with water, a leakage occurred from the rear of the DASC where the bracket to attach the solar concentrator in future experiments, was located. This leakage was caused by screws piercing through the rear of the aluminium box. An illustration of the attached bracket causing leakage was shown previously in Figure 3.3. Naturally, a generous amount of sealing, that can withstand both heat and fluid was

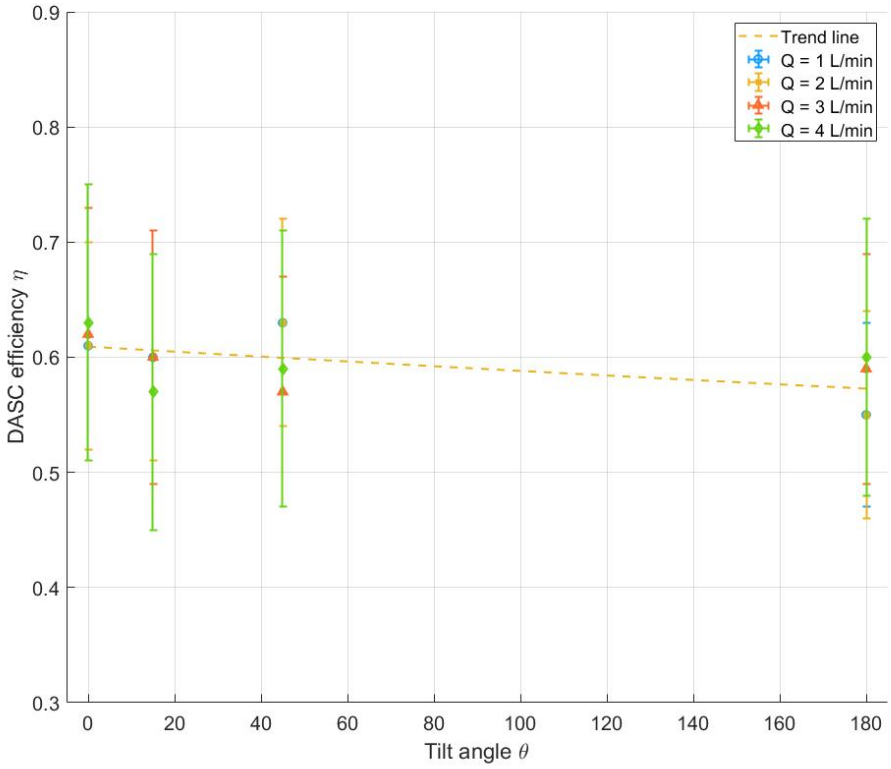

Figure 4.11: Experimental efficiency of water DASC with varying tilt angle.

applied to the screw holes and through the blocks. Regardless, this arrangement was not able to sustain the heat and high pressure associated with the continuous operation of the DASC. In hindsight, great care should be taken when using screws. Optimally, for future experiments, the outer aluminium box should have been constructed so that there are no areas vulnerable for potential leakages at higher pressures, e.g. by welding.

The COVID-19 lockdown of the University lead to the technical staff being temporarily unavailable. Repairs and improvements to the DASC within this study's timeframe were therefore not feasible. Nevertheless, experiments were continued as it was not an option neither to repair nor to terminate the experiments. However, one should be aware that the disturbance resulting from the leakage increases the uncertainty of the performance results. As a consequence, it is reasonable to question whether the results obtained with the leakage are representative of a fully functioning DASC system.

It should be noted that a minor leakage was visible already during the initial DASC experiments with water. Even though the leakage was minuscule, air bubbles were observed in the DASC during the experiments. In later experiments, the air bubbles were most prominent for the cases with nanofluid in the system, which might suggest that there could be a correlation between the leakage and the air bubbles. However, some other factors could

have caused air to enter the system. Cavitation may have caused small bubbles to occur in the pump house due to areas of reduced pressure around the impeller. Additionally, local boiling in the pump can also happen, as well as heating effects due to mechanical work and friction force in the fluid as a result of the impeller rotating.

Figure 4.12: Air bubbles inside the DASC under operation. The left photo is of a water DASC experiment with 180° tilt angle. The right photo is of a nanofluid DASC experiment with 45° tilt angle.

The most extreme result was observed with a 45° tilt angle when nearly fifty per cent of the DASC volume was covered by a large air bubble. This is possibly caused by gravity directing the nanofluid to accumulate at the bottom rather than spreading on the glass surface. This is illustrated to the right in Figure 4.12. Smaller bubbles were also observed for the other tilt angles, such as under an experiment with a 180° water DASC illustrated to the left in Figure 4.12. It must be expected that both significant and lesser volumes of air inside the DASC will decrease its efficiency, considering that the surface area of the collector is inversely proportional to its efficiency, which is shown previously in Equation (2.12).

Figure 4.13 displays two FLIR infrared photos of the nanofluid DASC, with a 0° tilt angle to the left, and 45° to the right. These photos shows that the air bubbles, in a smaller and larger scale, contributes to a heterogeneous heat distribution within the DASC. The area with bubbles is characterized by a region of higher temperature since the air becomes overheated. Ideally, the heat should be evenly distributed for optimal DASC performance.

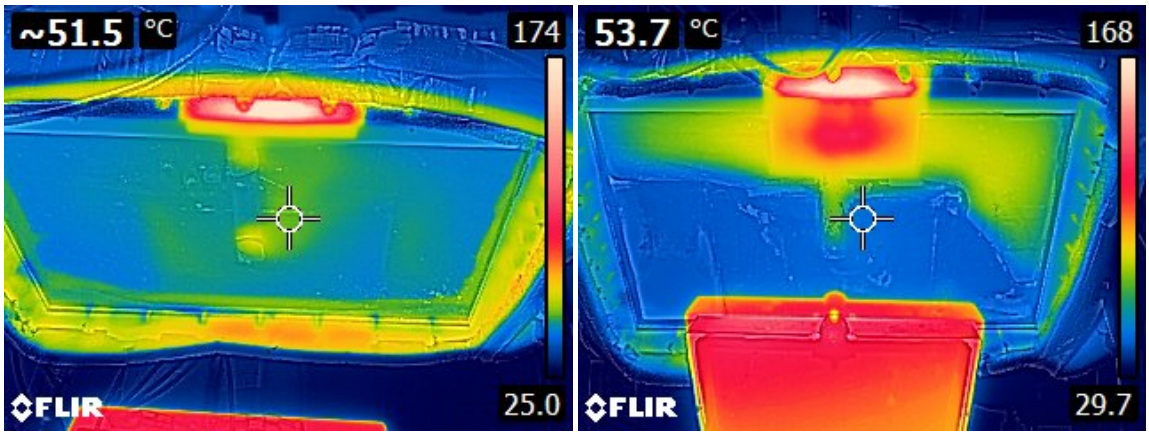

Figure 4.13: FLIR infrared photos of nanofluid DASC with 0° tilt angle to the left, and 45° to the right.

To give a representation of what influence an air bubble of the size observed to the right

in Figure 4.12 can have on the collector heat generation efficiency, an estimate was done with an effective exposed surface area reduced by fifty per cent. The result for nanofluid is plotted in comparison to the real experimental values for all cases shown in Figure 4.14. By halving the surface area, the collector efficiency doubles for all flow rates. When the DASC operates with a flow rate of 4 L/min and 45° tilt angle, the efficiency is increased from 38% to 77%. This estimate is considered to be somewhat exaggerated since it is difficult to measure the exact area in the DASC occupied by the air bubble. Nonetheless, the estimate points to the destructive effect air bubbles can have in such a system.

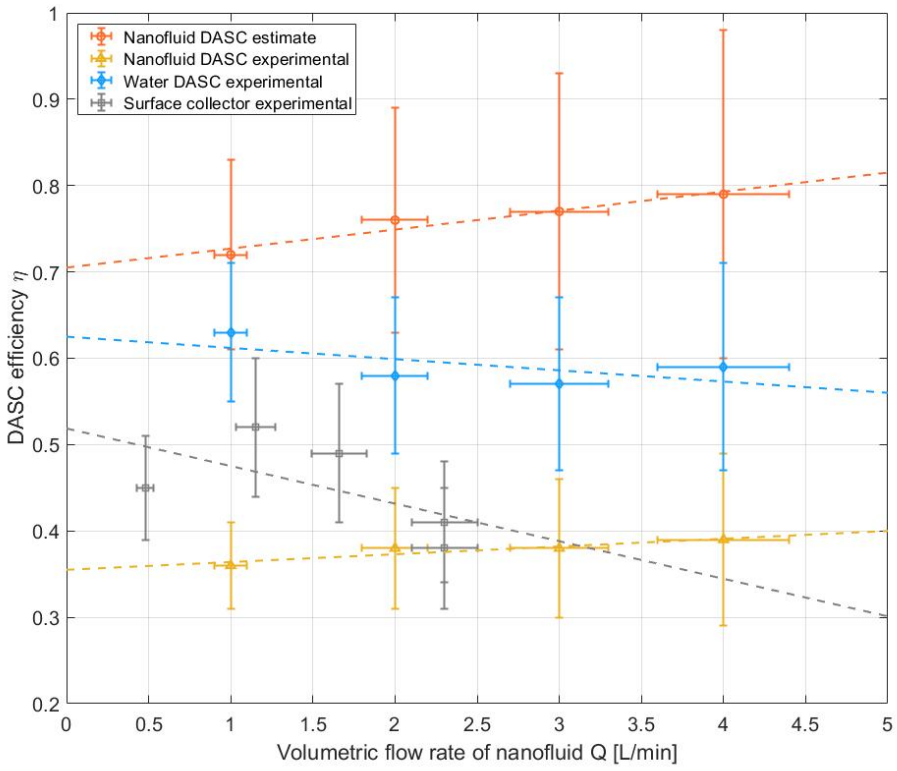

Figure 4.14: Experimental efficiency and estimated efficiency of nanofluid DASC with 45° tilt angle.

Finally, one cannot rule out the possibility that air bubbles were starting to be amassed even while the surface collector experiments were conducted. As the surface was covered by duct tape, neither visual nor infrared camera confirmation of potential air bubbles were possible. However, as the leakage became apparent after the initial experiments were conducted, one can assume that any accumulation of air would not be as prominent as from the later stages of the project. Conclusively, the possible assemblage of air bubbles within the solar collector presents an additional uncertainty to the final results.

4.2.4 Nanofluid properties

An evaluation of the properties of this specific nanofluid is also essential since it is directly related to the efficiency of the collector. The introductory theory about nanofluids in Chapter 2.1.1 states that a prerequisite for utilising nanofluids for enhancing solar collectors is that the particle concentration is high enough, allowing most of the incident sunlight to be absorbed. Even though a nanofluid containing 0.05wt% CB nanoparticles has been experimentally confirmed to fit the above criteria [91], the results in this research indicate otherwise.

Two reasonable theories may explain why the particle concentration turned out to be inadequate in this study. Firstly, the concentration may have been lower than anticipated from the start. The ultrasonic bath has proven to very effectively break up soft agglomerates in a nanofluid. However, it is possible that some hard agglomerates, which do not break up easily, have been present in the nanofluid. These agglomerates may not have been adequately dispersed by the sonication process. Thus, they may have separated from the suspension and settled at the bottom of the reservoir tank shortly after the fluid was poured into the reservoir tank.

The second issue is that the nanoparticles may have aggregated in the nanofluid and been deposited on the upper and lower collector surfaces, as well as elsewhere in the system. Examples of particle deposition in the tubes were previously shown in figure 3.9. There was also clear evidence of particle deposition on the DASC surface during the last experiments with 180° tilt angle (see Figure 4.24). Such conditions may result in higher temperature gradients at the surface and a drop in the effective particle concentration within the nanofluid. This problem is discussed in more detail later in Chapter 4.3.2.

4.2.5 Comparison to the surface collector

Although the range of investigated flow rates differs between the surface collector and the DASC, it is possible to compare the collector performances for a flow rate of 1 L/min (1.15 L/min for the surface collector) for 0°, 15°, and 45° tilt angles. The efficiency values from Tables 4.1, 4.3 and 4.2 show a prevailing trend where the water DASC achieves higher efficiency than both the surface collector and the nanofluid DASC at all three tilt angles. The surface collector efficiency is equal to the nanofluid DASC at a 0° tilt angle. For the remaining tilt angles, the surface collector operates with much higher efficiency than the nanofluid DASC.

There are several underlying properties which can explain why the DASC with water performed better than both nanofluid and the surface collector. Firstly, there is less heat loss associated with a transparent surface, than for surface absorber which the surface collector utilises. This surface absorber leads to significant convective and radiative heat loss since the emitted radiative energy from a surface is equal to the fourth power of its temperature (as shown previously in Equation (2.7)). For the DASC with water, however, the radiative heat loss will be much lower due to the transparent surface. The convective heat loss, associated with the temperature gradient between the DASC and the surroundings, is also lower since the transparent surface does not hold high temperatures to the

degree the surface absorber do.

The internal DASC bottom surface was painted matte black to achieve absorptive behaviour. It can be assumed that the absorptive bottom has caused the temperature of the fluid in its vicinity to rise significantly. Thus, the bulk fluid achieves a higher mean temperature due to more homogenous and efficient heating compared to when the fluid is heated from the surface only. Delfani et al. [99] also experienced increased DASC efficiency due to an absorptive bottom surface when using base fluid as working fluid. However, Gutapa et al. [74] found that for low concentration nanofluids, the same effect led to increased emissive losses and hence lower collector efficiency. Whether the emissive losses are increased due to the black bottom surface in this study is not evident. However, this could be investigated in future experiments by varying the particle concentration in the nanofluid.

Table 4.2: Summary of experimental results for nanofluid DASC.

Tilt angle 0°

Volumetric flow rate Q [L/min]	SD of the mean ΔT [°C]	Efficiency η	Mean ambient T [°C]
1.0	1.377 ± 0.005	0.54 ± 0.08	27.3
2.0	0.682 ± 0.007	0.54 ± 0.09	27.4
3.0	0.480 ± 0.002	0.57 ± 0.10	26.5
4.0	0.357 ± 0.012	0.57 ± 0.11	26.6

Tilt angle 15°

Volumetric flow rate Q [L/min]	SD of the mean ΔT [°C]	Efficiency η	Mean ambient T [°C]
1.0	1.080 ± 0.020	0.43 ± 0.06	28.3
2.0	0.630 ± 0.020	0.50 ± 0.08	28.6
3.0	0.427 ± 0.007	0.51 ± 0.09	27.5
4.0	0.326 ± 0.003	0.52 ± 0.11	27.9

Tilt angle 45°

Volumetric flow rate Q [L/min]	SD of the mean ΔT [°C]	Efficiency η	Mean ambient T [°C]
1.0	0.909 ± 0.005	0.36 ± 0.05	28.0
2.0	0.477 ± 0.005	0.38 ± 0.07	28.0
3.0	0.321 ± 0.003	0.38 ± 0.08	28.3
4.0	0.248 ± 0.009	0.39 ± 0.10	28.0

Tilt angle 180°

Volumetric flow rate Q [L/min]	SD of the mean ΔT [°C]	Efficiency η	Mean ambient T [°C]
1.0	0.947 ± 0.012	0.37 ± 0.06	28.4
2.0	0.503 ± 0.003	0.40 ± 0.07	27.8
3.0	0.370 ± 0.006	0.44 ± 0.09	28.3
4.0	-	-	-

Table 4.3: Summary of experimental results for water DASC.

Tilt angle 0°

Volumetric flow rate Q [L/min]	SD of the mean ΔT [°C]	Efficiency η	Mean ambient T [°C]
1.0	1.435 ± 0.006	0.61 ± 0.09	26.4
2.0	0.704 ± 0.009	0.60 ± 0.09	26.3
3.0	0.487 ± 0.006	0.62 ± 0.11	25.9
4.0	0.370 ± 0.005	0.63 ± 0.12	26.7

Tilt angle 15°

Volumetric flow rate Q [L/min]	SD of the mean ΔT [°C]	Efficiency η	Mean ambient T [°C]
1.0	1.417 ± 0.003	0.60 ± 0.09	26.8
2.0	0.671 ± 0.008	0.57 ± 0.09	26.8
3.0	0.472 ± 0.011	0.60 ± 0.11	26.7
4.0	0.330 ± 0.030	0.57 ± 0.12	26.6

Tilt angle 45°

Volumetric flow rate Q [L/min]	SD of the mean ΔT [°C]	Efficiency η	Mean ambient T [°C]
1.0	1.489 ± 0.005	0.63 ± 0.09	26.9
2.0	0.680 ± 0.005	0.58 ± 0.09	26.8
3.0	0.446 ± 0.013	0.57 ± 0.10	26.2
4.0	0.344 ± 0.003	0.59 ± 0.12	26.7

Tilt angle 180°

Volumetric flow rate Q [L/min]	SD of the mean ΔT [°C]	Efficiency η	Mean ambient T [°C]
1.0	1.302 ± 0.007	0.55 ± 0.08	26.5
2.0	0.654 ± 0.002	0.56 ± 0.09	27.0
3.0	0.460 ± 0.003	0.59 ± 0.10	27.2
4.0	0.353 ± 0.003	0.60 ± 0.12	27.2

4.3 Nanofluid stability analysis

The nanofluid stability analysis is performed by SLS, as explained in Chapter 3.8. Firstly, the PSD results for the reference nanofluids are summarised and discussed, followed by an analysis of the two samples collected from the reservoir tank. Finally, a brief review of nanofluid instability related to foam generation is presented.

4.3.1 Stability of reference nanofluid

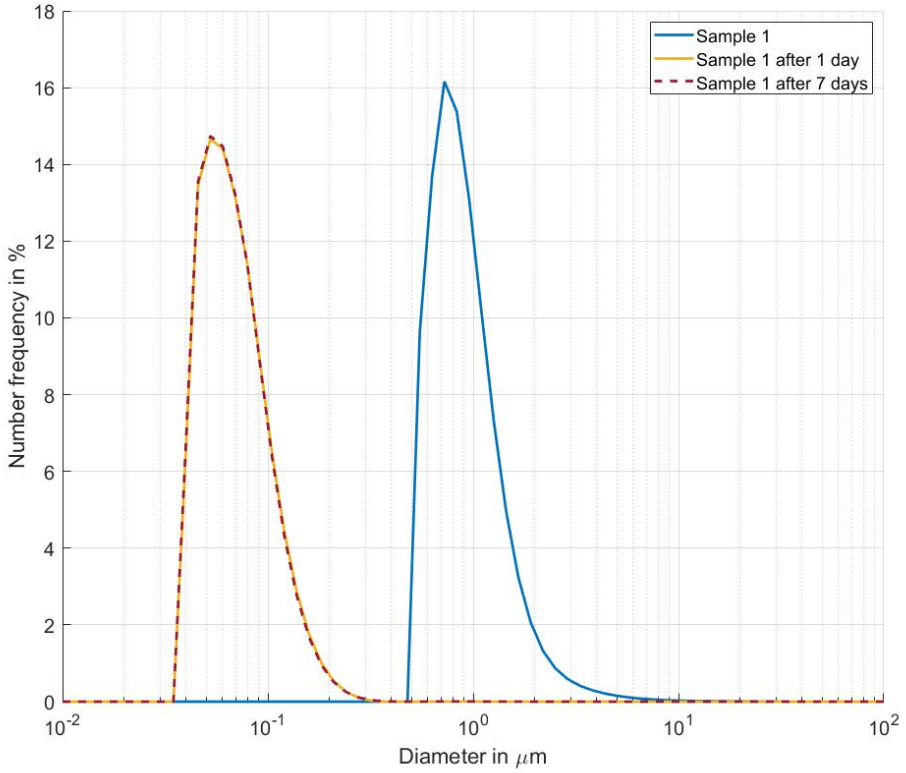

Figure 4.15: Particle size distribution of sample 1.

Figure 4.15 shows a comparison of the PSD for the nanofluid sample 1 right after sonication, after one day, and after seven days. As easily spotted in Figure 4.15, the peak of the PSD curve shifts from near microscale right after sonication to nanoscale the next day, which also nearly overlaps with the curve obtained after seven days. The peak in number frequency after one day and seven days is at 52.4 nm, which corresponds well to previously specified average particle size of Ensaco 350G Carbon Black particles, 51.1 $\pm$ 17.0 nm [78].

The sudden reduction in particle sizes contradicts to previous research and expectations, but may be explained with an analysis of the surfactant behaviour. Cosgrove [47] explains that the equilibrium surface tension is not achieved instantaneously for any surfactant

solution. The surfactants molecules must have time to diffuse from the bulk fluid to the particle surface, then absorb, whilst also achieving the correct orientation. Accordingly, a freshly formed interface of a surfactant solution has a surface tension close to that of the solvent, which will then decay over a certain time to the equilibrium value. According to Cosgrove [47], the relaxation process can range from milliseconds to days, depending on both surfactant type and concentration. It is reasonable to assume that this process was completed within 24 hours after sample 1 was prepared since the PSD curve does not change significantly in the next seven days. An additional element to consider is that some of the visible sediments from the left photo in Figure 4.16 were fluidized in the nanofluid right after sonication. Thus, some larger particles have deposed on the container bottom within 24 hours, and the SLS analysis will detect a reduced amount of these larger particles in the nanofluid the next day.

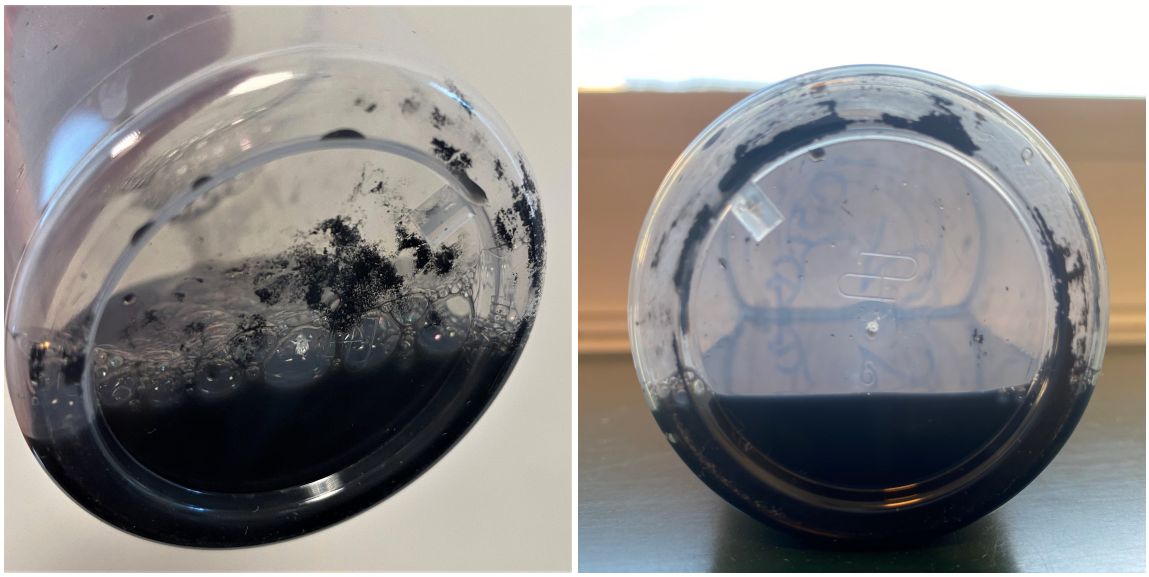

Figure 4.16: Sedimentation on container bottom of reference nanofluid samples after seven days. Sample 1 to the left, and sample 2+3 to the right.

As discussed in Chapter 3.8, minimal changes in the PSD over time may indicate excellent long-term stability of the nanofluid, especially in combination with minimal amounts of visible sedimentation or fall out of nanoparticles. Sample 1 exhibit similar behaviour, since the PSD curves for both sample 1 after one day and seven days are almost identical, which implies that there is only a limited change in the number frequency of the particles at each size in the nanofluid. Only a slight amount of particles can be spotted on the sample container bottom, shown to the left in Figure 4.16. It is also possible that some of the sedimented particles never were dispersed adequately in the fluid during sonication, hence they would remain at the bottom of the container from the start.

A comparable PSD curve development can be recognised for sample 2+3 in Figure 4.17. As seen in Figure 4.15 for sample 1, the PSD curves are almost identical after one day and after seven days. Further inspection reveals that after mixing sample 1 and 2, the PSD

curve shifted slightly to the right towards smaller particle sizes, possibly due to the extra hour of sonication. The increased sonication time may have broken up some remaining agglomerates or particle clusters. For future research, a more extensive characterisation of the influence of additional sonication time for such a nanofluid could be of great interest since this result goes contrary to findings by Hwang et al. [92] as discussed in Chapter 3.7.

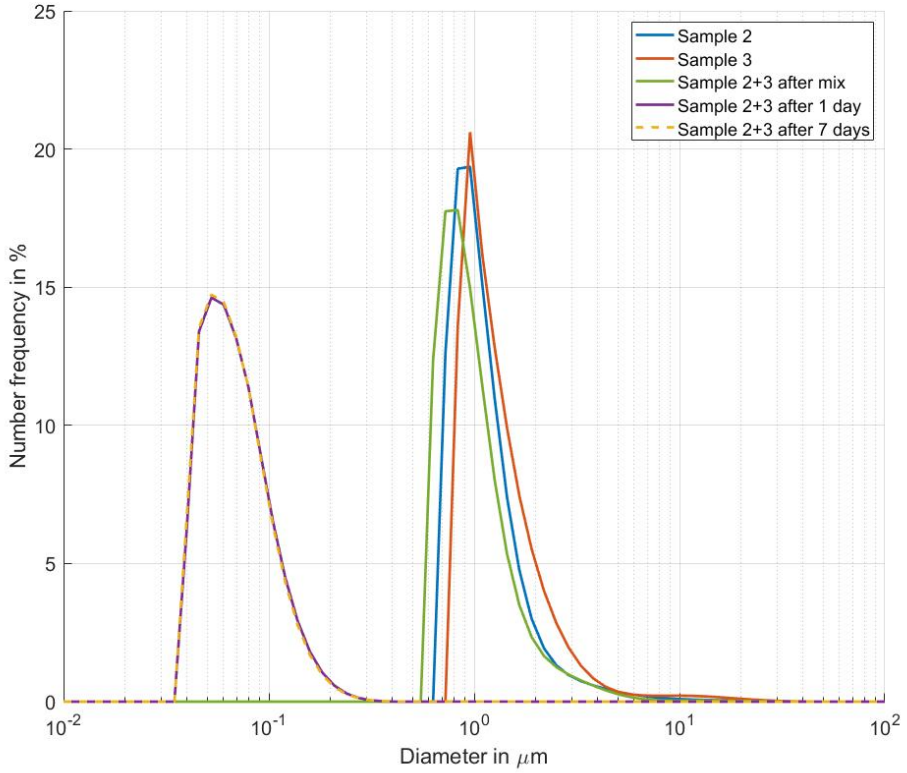

Figure 4.17: Particle size distribution of sample 2, 3 and 2+3.

In light of the reasons discussed above, it can be concluded that there is not a noteworthy change in the nanofluid stability associated with mixing two different samples of equal composition. Additional evidence can be found to the right in Figure 4.16, which shows only small remains of nanoparticle deposits on the container bottom of sample 2+3 after seven days at rest. The photo is taken immediately after tilting the container to limit the potential sediments from slipping into the fluid. Visual observation of the container was also performed before tilting.

4.3.2 Stability of the reservoir tank nanofluid

The PSD analysis of the samples from the reservoir tank is presented in Figure 4.18. Sample TANK1 was collected from the reservoir tank before the nanofluid was circulated though the system, while sample TANK2 was collected from the same nanofluid, but after seven days of operation. Sample TANK1 obtained PSD curves after seven days which were almost identical as the initial analysis right after collection. This suggests that there is very little difference in the sizes of the particles in the nanofluid, which imply a limited occurrence of particle agglomeration. Furthermore, the left photo in Figure 4.20 show that only minimal amounts of sediments can be spotted on the bottom of the container after seven days. These observations support the findings in Figure 4.17, which demonstrated that mixed nanofluids could obtain great stability. It is therefore, logical to conclude that such stability can also be expected for even larger volumes of mixed nanofluid.

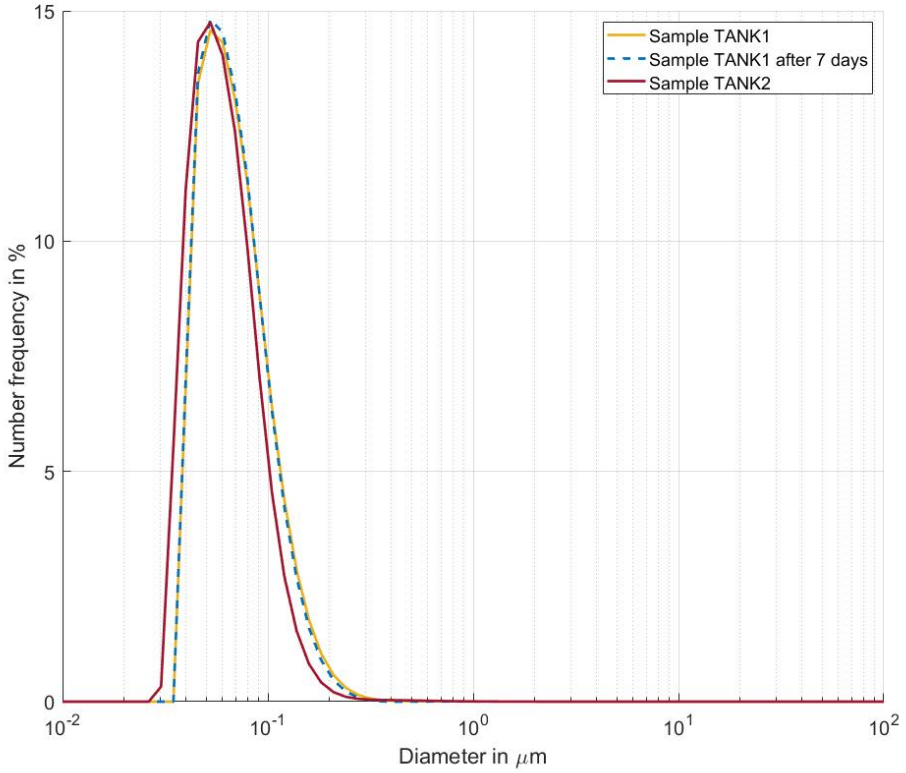

Figure 4.18: Particle size distribution of nanofluid samples taken from the reservoir tank.

An interesting observation is that the PSD curve of sample TANK2 has a slight shift to the right, which indicates that there has been an increase in smaller particle sizes in the nanofluid after the DASC has been operating for seven days. Periodic irregularities of the Malvern 2000 apparatus or other uncertainties with this particular PSD analysis method (see Chapter 3.8) might be the reason for such a small variation since one would

expect the PSD to be near equal or shift towards larger sizing with time. In this regard, further investigation was necessary to rule out the possibility of an unstable nanofluid. Visual inspection for sedimentation or depositions on containers was therefore done. The left photo in Figure 4.19 shows sample TANK2 right after collection compared to sample TANK1 seven days at rest after collection. The photo shows that sample TANK2 is a somewhat more translucent nanofluid, which can be interpreted as evidence of a decreased concentration of carbon black nanoparticles in suspension. Moreover, the right photo in Figure 4.19 exposes a highly unstable nanofluid after seven days. The colour-gradient from the bottom sediment to the nearly transparent upper layer of the nanofluid indicates a heterogeneous suspension.

Figure 4.19: Nanofluid samples collected from the reservoir tank. The left photo shows TANK1 after seven days, and TANK2 to the right after collection. The right photo shows sample TANK2 after seven days.

The discrepancy between the two reservoir samples comes from TANK2 having been exposed to heating and circulation numerous times during operation of the DASC, whereas TANK1 have not. As mentioned in Chapter 2.1.2, heating nanofluids to high temperatures can damage the bonding between the surfactant and the nanoparticles, thus making the nanofluid unstable. However, the PSD curves do not indicate agglomeration of dispersed particles in the fluid. A possible explanation is that gravity has caused the unstable particles, agglomerates, and clusters to fall out and settle elsewhere, such as on reservoir bottoms or in the tube systems. The photos in Figure 4.20 shows the difference in sedimentation on the sample container bottom of TANK1 and TANK2 after seven days at rest. As predicted, a more substantial amount of sediments can be observed for sample TANK2. The left photo in Figure 4.21 shows how nanoparticles have adhered to the reservoir tank wall during operation of the DASC. There was also visible depositions of nanoparticles inside fittings and tubes, which is illustrated to the right in Figure 4.21, and previously in Figure 3.9a, possibly due to local conditions such as constrictions, roughness and changes in diameters.

When assessing the stability issue, it is necessary to consider two particular components and their influence on the nanofluid. Firstly, the added surfactant, SDS, which is sensitive to heating needs to be evaluated. Although this current nanofluid DASC system operated

Figure 4.20: Sedimentation in nanofluid samples from the reservoir tank after seven days at rest. Sample TANK1 to the left, and sample TANK2 to the right.

at a maximum measured temperature of 52°C, local temperatures in the nanofluid may have been even higher. Thus, surpassing the SDS stability threshold of $\sim$ 60°C [45]. Repeated heating and operation over days may also have caused the surfactant to become unstable.

Moreover, the addition of FoamStop to the nanofluid also needs to be discussed. FoamStop turned out to be the solution to the troublesome foam generation issue, which is addressed later in Chapter 4.3.3. Only a minimal amount of research and testing [30] has been done with this type of chemical in nanofluid, and its effect on nanofluid stability is, therefore, uncertain. The results concerning sample TANK1, however, suggest that the FoamStop is not destructive for nanofluid stability when not heated since the sample exhibited excellent stability over time.

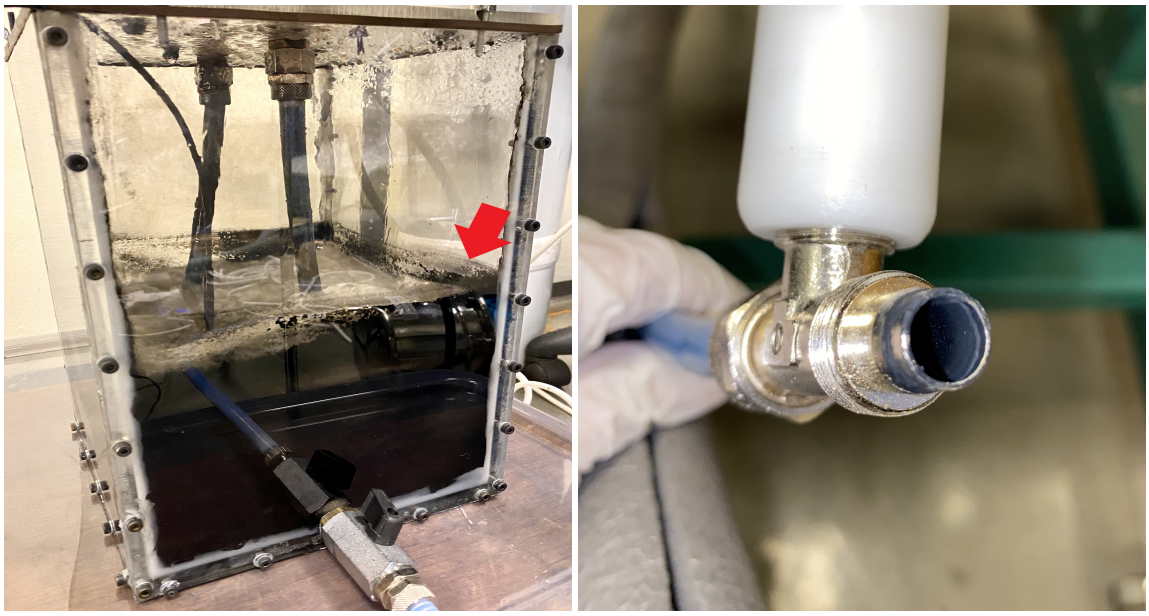

Figure 4.21: Deposition of nanoparticles in the reservoir tank wall to the left, and in a t-pipe joint to the right.

4.3.3 Foam generation in the reservoir tank

During the initial experiment with a nanofluid in the DASC system, it was observed that a considerable amount of foam was continuously generated. This is shown in Figure 4.22. There was only a small layer of liquid nanofluid visible in the bottom part of the reservoir tank. Even though the reservoir output valve was placed at the bottom part where the liquid was observed, it was apparent that foam was also circulated through the system. The flow meter displayed abnormally low flow rates since the instrument has not been calibrated for such modest fluid densities. The foam was also easily observed in the DASC.

Even smaller volumes of foam are expected to reduce the efficiency of the DASC since the properties of the nanofluid will change [100]. The foam is most likely caused by the SDS surfactant in the nanofluid, and possibly by cavitation in the pump. As pointed out in Chapter 2.1.2, some surfactants produce foams. Since SDS is a commonly used surfactant in nanofluids [100], such problems were not expected to appear to this extent in these experiments. However, some situations must be mentioned. Otanicar et al. [21] experienced foam generation in the nanofluid due to SDS during their experiments with the micro-solar thermal collector. They solved the issue by degassing the nanofluids in a vacuum chamber prior to charing the collector with nanofluid. Ulset [78] observed the formation of foam in the CB nanofluids during boiling, which was credited to the SDS, reducing the surface tension of the liquid. However, it was not expected to reach such temperatures required for boiling in this study. To conclude, this proves that extra caution must be taken when implementing experiences and results from characterisation and small-scale experimental studies, as the product may not be applicable for larger systems.

In an attempt to reduce the amount of foam created, Antifoam B Emulsion [101], an aqueous-silicone emulsion from Sigma Aldrich, was added to the system. Information provided by Sigma Aldrich states that this type of antifoam is effective in the concentration of 1-100 ppm. Firstly, a proportionate amount of nanofluid ($\sim$ 0.2 kg) was retrieved from the reservoir tank, and a small amount (1 g, equal to $\sim$ 100 ppm for 10 kg of nanofluid) of antifoam was mixed in with the nanofluid and afterwards returned to the reservoir tank. Then the solution was stirred to create a homogenous mixture in the reservoir tank. The pump was started afterwards to circulate the nanofluid through the system. The foam production rate was significantly slower after 1 g of antifoam was added to the nanofluid. Despite the inclusion of the antifoam agent, the foam managed to build up in the reservoir tank when continuously circulating through the system. The amount of antifoam was, therefore, increased sequentially to observe if it was possible to overcome the foam generation in this current batch of nanofluid. However, with no observable difference between the quantity of 1-50 g, the nanofluid was flushed from the system as the initial qualities of the nanofluid must be considered to be compromised due to the high volume of antifoam agent.

It must be noted that the Antifoam B Emulsion had a shelf date that passed a couple of months before these experiments were conducted. The antifoam was nevertheless tested as

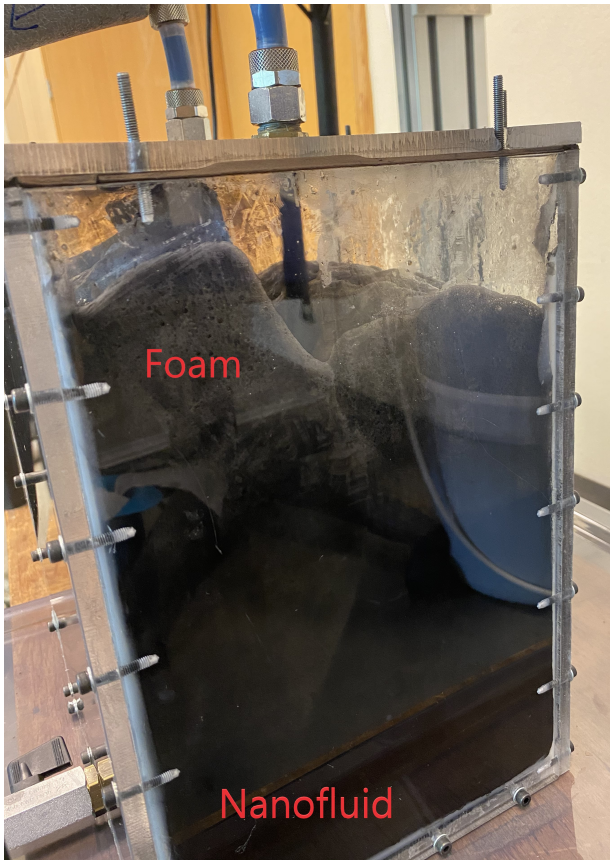

Figure 4.22: Illustration of the foam generation in the reservoir tank.

it was not possible to acquire a fresh defoaming agent under the prevailing circumstances quickly. The date is likely to have had some impact on anticipated foam destruction abilities. Furthermore, it is reasonable to assume that this antifoam would have affected the long-term nanofluid stability since it was not properly mixed in, i.e. with the use of an ultrasonic bath.

For the next experiments, the system was cleaned following the same process as described in Chapter 3.2.3, and a new nanofluid had to be prepared. A nanofluid without antifoam would be preferable as there is a lack of research regarding the use of antifoam solution in nanofluids. As an alternative to the SDS, a sample with 0.5wt% Triton X-100 was prepared with no antifoam. The sample was first shaken to see if any foam was generated inside the container. Unfortunately, the shaking produced enough foam to dismiss Triton X-100 as an option. The result can be seen in Figure 4.23.

Finally, a nanofluid containing both SDS and 0.5wt% FoamStop [93] from Kärcher was prepared. The FoamStop was added prior to the initial sonication in the ultrasonic bath. It must be noted that the optical properties of FoamStop are unknown and that characterisation of a nanofluid containing this component would be advantageous for future experiments. Nonetheless, with FoamStop added, the initial experiments showed no sig-

Figure 4.23: Foam generated by shaking a nanofluid sample containing Triton X-100.

nificant volume of foam generation. However, during the final experiments with nanofluid, a smaller volume of foam could be observed in the DASC and the reservoir tank, shown in Figure 4.24. This foam is possibly a result of the progressively more unstable nanofluid, as discussed earlier in this chapter. In conclusion, future investigations of various nanofluid compositions are recommended to determine whether SDS needs to be replaced with another suitable surfactant, or if a different type of defoaming agent must be added to the nanofluid.

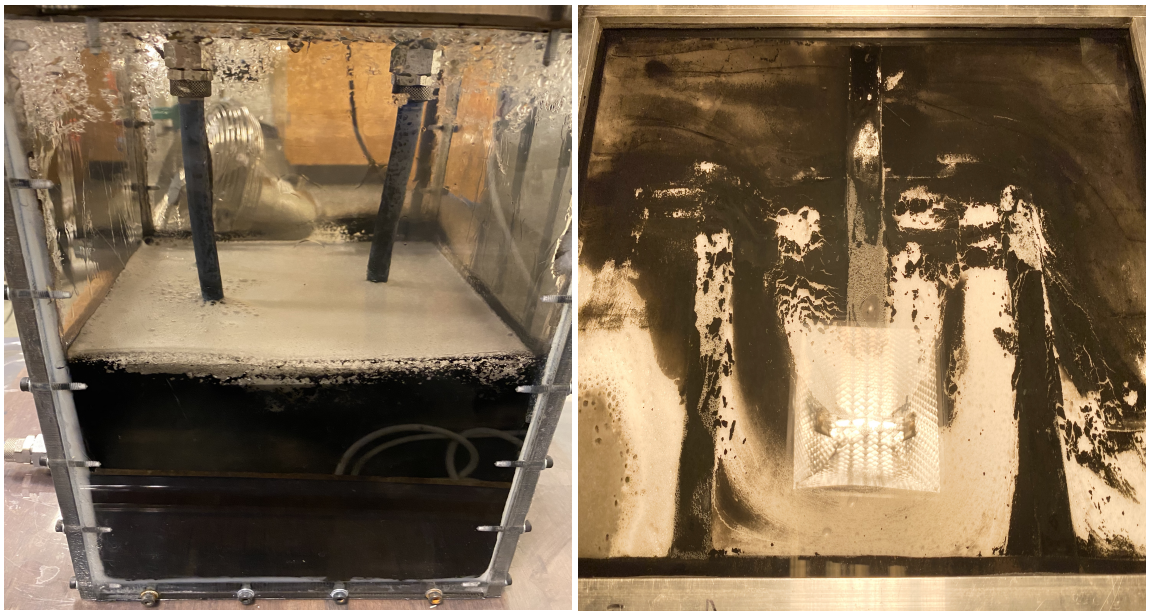

Figure 4.24: Foam in the reservoir tank and DASC during the final nanofluid experiments.

Chapter 5

Concluding Remarks

The purpose of this study was to develop an experimental setup for investigating the volumetric heat generation efficiency of DASC with nanofluid. A DASC design was proposed, constructed, and studied under laboratory conditions. The volumetric absorption by 0.05wt.% carbon black nanofluid (51.1 ± 17.0 nm average particle size) was compared to both water and to a conventional surface collector.

The influence of two parameters on collector efficiency was studied, namely the DASC tilt angle and the fluid flow rate. The DASC tilt angle was altered between 0°, 15°, 45°, and 180°, to investigate the influence of gravity on the nanofluid column. Furthermore, at all tilt angles, the flow rate through the system was varied in the range 1-4 L/min, giving a total of four experiments per tilt angle.

The volumetric heat generation efficiency of the nanofluid DASC was found to closely correspond to rising flow rate through the system, due to increased forced convection within the fluid bulk. For all three cases (nanofluid/water DASC and surface collector), the collector achieved the highest efficiency when oriented with a 0° tilt angle. For the nanofluid case, this can be credited to the Rayleigh Bérnard convection effects within the nanofluid. For other tilt angle orientations (15°, 45°, and 180°), the Rayleigh-Bérnard convection effect is very reduced, or nearly absent, which leads to lower collector efficiency. For the DASC with water and the surface collector, the slightly higher efficiency at 0° tilt angle may be attributed mainly to two factors. Firstly, decreased heat loss from the collector surface and secondly heating effects by natural convection from the halogen lamp. Finally, among the three collector cases, the DASC with water as working fluid performed at a superior level for all examined conditions, which does not correspond to initial expectations based on experiments described in literature.

The results from this study also address various challenges to the technical DASC design, operation conditions and the nanofluid itself, which are recommended to be properly examined in future DASC experiments.

Particle sedimentation and deposition were observed in the reservoir tank, DASC, and the tube system. This will likely cause a less efficient particle concentration in the nanofluid

during operation than what could be expected. Too low particle concentration can be detrimental for the DASC efficiency since the nanofluid is not capable of absorbing all the incident radiation. This emphasises the importance of experimental studies, especially on a larger scale, since they reveal practical problems that are not necessarily encountered in analytical studies.

Several challenges related to nanofluid stability under operation with the DASC were identified. Firstly, the SDS surfactant generated a problematical amount of foam in the reservoir tank when the nanofluid was circulated through the system. This issue was resolved using an antifoam agent mixed in with the other nanofluid components before sonication. Secondly, the nanofluid showed poor stability over time when repeatedly heated. During the final experiments, smaller volumes of foam were observed within the DASC and the reservoir tank, as well as increased deposition of particles on the DASC surface. On the other hand, the same nanofluid showed excellent stability over a period of seven days when not heated. Further investigation is needed to clarify whether it was instability in the bonding between the SDS and the nanoparticles, or the defoaming agent, that caused the nanofluid to become unstable.

During the DASC experiments with water and nanofluid, leakages from the DASC, connectors and tubings became a disturbance. Furthermore, an increasing amount of air bubbles in the collector was observed during the later experiments for both types of fluid. In summary, it is reasonable to assume that the efficiency results for the nanofluid in this study are lower than what could be expected for the same DASC design without the previously mentioned problems.

Chapter 6

Future Work

The utilisation of nanofluids in DASCs presents many opportunities for future work. This study aimed to construct a functional DASC design, which later could be used in combination with a solar concentrator. The collector has been tested under various parameters, based on variations in tilt angle and flow rate. Suggestions for future work are listed below.

1. DASC experiments
    - Analyse the collector efficiency at flow rates past the 4 L/min achieved in this study.
    - Investigate the impact of changing the number of baffles, i.e varying residence time within the collector.
    - Application of CB nanofluids with higher concentrations in the DASC, as well as other types of nanofluids.
    - Examine the effect of altering the nanofluid film thickness/collector depth.
    - Use the DASC in combination with the solar concentrator, with varying irradiation strength.
    - Investigate tilt angles in the range between 45-180°.
    - Reduce the total experimental uncertainty by using measurement equipment and instruments with higher accuracy, e.g. a flow meter with lower uncertainty.
2. Nanofluid properties
    - Investigate the impact of increased sonication time on nanofluid stability.
    - Study the influence on optical properties and stability of a nanofluid when adding a defoaming agent.

These suggested studies could further improve the understanding of nanofluids while also making use of solar energy even more efficient in the future.

Bibliography

[1] I. E. Agency, *World energy outlook 2019*, 2019. [Online]. Available: https://www.iea.org/reports/world-energy-outlook-2019 (visited on 02/12/2020).

[2] J. Glenza, A. Evans, H. Ellis-Petersen, and N. Zhou, "Climate strikes held around the world – as it happened", *The Guardian*, Mar. 2019. [Online]. Available: https://www.theguardian.com/environment/live/2019/mar/15/climate-strikes-2019-live-latest-climate-change-global-warming#comments (visited on 02/13/2020).

[3] U. Nations, *The paris agreement*, Dec. 2015. [Online]. Available: https://unfccc.int/files/essential_background/convention/application/pdf/english_paris_agreement.pdf (visited on 02/12/2020).

[4] Z. Liu, "Chapter 4 - supply and demand of global energy and electricity", in *Global Energy Interconnection*, Z. Liu, Ed. Boston: Academic Press, 2015, pp. 101–182, ISBN: 978-0-12-804405-6. DOI: https://doi.org/10.1016/B978-0-12-804405-6.00004-X. [Online]. Available: http://www.sciencedirect.com/science/article/pii/B978012804405600004X.

[5] K. Kaygusuz, "Energy for sustainable development: Key issues and challenges", *Energy Sources, Part B: Economics, Planning, and Policy*, vol. 2, no. 1, pp. 73–83, 2007. DOI: 10.1080/15567240500402560.

[6] U. N. D. Programme and W. H. Organization, *The energy access situation in developing countries: A review focusing on the least developed countries and sub-saharan africa*, Feb. 2009. [Online]. Available: https://www.undp.org/content/dam/undp/library/Environment%20and%20Energy/Sustainable%20Energy/energy-access-situation-in-developing-countries.pdf (visited on 02/14/2020).

[7] U. N. D. Programme, *World energy assessment: Energy and the challenge of sustainability*, 2000. [Online]. Available: https://www.undp.org/content/undp/en/home/librarypage/environment-energy/sustainable_energy/world_energy_assessmentenergyandthechallengeofsustainability.html (visited on 02/13/2020).

[8] I. E. Agency, *Installed power generation capacity by source in the stated policies scenario, 2000-2040*, 2019. [Online]. Available: https://www.iea.org/data-and-statistics/charts/installed-power-generation-capacity-by-source-in-the-stated-policies-scenario-2000-2040 (visited on 02/14/2020).

[9] R. Swanson, "Approaching the 29% limit efficiency of silicon solar cells", in *Conference Record of the Thirty-first IEEE Photovoltaic Specialists Conference, 2005.*, IEEE, 2005, pp. 889–894.

[10] M. Alberghini, M. Morciano, L. Bergamasco, M. Fasano, L. Lavagna, G. Humbert, E. Sani, M. Pavese, E. Chiavazzo, and P. Asinari, "Coffee-based colloids for direct solar absorption", *Scientific Reports*, vol. 9, no. 1, p. 4701, 2019.

[11] J. Minardi and H. Chuang, "Performance of a "black" liquid flat-plate solar collector", *Solar Energy*, vol. 17, no. 3, pp. 179–183, 1975.

[12] N. Goel, R. Taylor, and T. Otanicar, "A review of nanofluid-based direct absorption solar collectors: Design considerations and experiments with hybrid pv/thermal and direct steam generation collectors", *Renewable Energy*, vol. 145, pp. 903–913, 2020.

[13] D. Han, Z. Meng, D. Wu, C. Zhang, and H. Zhu, "Thermal properties of carbon black aqueous nanofluids for solar absorption", *Nanoscale Research Letters*, vol. 6, no. 1, p. 457, 2011.

[14] A. Gimeno-Furió, E. Juliá, S. Barison, F. Agresti, C. Friebe, and M. Buschmann, "Nanofluids as direct solar energy absorbers", *Journal of Nanofluids*, vol. 8, no. 1, pp. 17–29, 2019.

[15] T. Yousefi, F. Veysi, E. Shojaeizadeh, and S. Zinadini, "An experimental investigation on the effect of al2o3–h2o nanofluid on the efficiency of elat-plate solar collectors", *Renewable Energy*, vol. 39, no. 1, pp. 293–298, 2012.

[16] M. Mirzaei, S. Hosseini, and A. Kashkooli, "Assessment of al2o3 nanoparticles for the optimal operation of the flat plate solar collector", *Applied Thermal Engineering*, vol. 134, pp. 68–77, 2018.

[17] M. Mirzaei, "Experimental investigation of cuo nanofluid in the thermal characteristics of a flat plate solar collector", *Environmental Progress & Sustainable Energy*, vol. 38, no. 1, pp. 260–267, 2019.

[18] H. Tyagi, P. Phelan, and R. Prasher, "Predicted efficiency of a low-temperature nanofluid-based direct absorption solar collector", *Journal of Solar Energy Engineering*, vol. 131, no. 4, 2009.

[19] R. Taylor, P. Phelan, T. Otanicar, R. Adrian, and R. Prasher, "Nanofluid optical property characterization: Towards efficient direct absorption solar collectors", *Nanoscale Research Letters*, vol. 6, no. 1, p. 225, 2011.

[20] R. Taylor, P. Phelan, T. Otanicar, C. Walker, M. Nguyen, S. Trimble, and R. Prasher, "Applicability of nanofluids in high flux solar collectors", *Journal of Renewable and Sustainable Energy*, vol. 3, no. 2, 2011.

[21] T. Otanicar, P. Phelan, R. Prasher, G. Rosengarten, and R. Taylor, "Nanofluid-based direct absorption solar collector", *Renewable and Sustainable Energy*, vol. 2, no. 3, 2010.

[22] E. Filho, O. Mendoza, C. Beicker, A. Menezes, and D. Wen, "Experimental investigation of a silver nanoparticle-based direct absorption solar thermal system", *Energy Conversion and Management*, vol. 84, pp. 261–267, 2014.

[23] T. Otanicar and J. Golden, "Comparative environmental and economic analysis of conventional and nanofluid solar hot water technologies", *Environmental Science & Technology*, vol. 43, no. 15, pp. 6082–6087, 2009.

[24] A. Lenert and E. Wang, "Optimization of nanofluid volumetric receivers for solar thermal energy conversion", *Solar Energy*, vol. 86, no. 1, pp. 253–265, 2012.

[25] O. Sharaf, D. Kyritsis, A. Al-Khateeb, and E. Abu-Nada, "Effect of bottom surface optical boundary conditions on nanofluid-based dasc: Parametric study and optimization", *Solar Energy*, vol. 164, pp. 210–223, 2018.

[26] M. Karami, S. Delfani, and M. Esmaeili, "Effect of v-shaped rib roughness on the performance of nanofluid-based direct absorption solar collectors", *Journal of Thermal Analysis and Calorimetry*, vol. 138, no. 1, pp. 559–572, 2019.

[27] J. Eggers, E. Lange, and S. Kabelac, "Radiation and energetic analysis of nanofluid based volumetric absorbers for concentrated solar power", *Nanomaterials*, vol. 8, no. 10, p. 838, 2018.

[28] B. Balakin, O. Zhdaneev, A. Kosinska, and K. Kutsenko, "Direct absorption solar collector with magnetic nanofluid: Cfd model and parametric analysis", *Renewable Energy*, vol. 136, pp. 23–32, 2019.

[29] K. Wang, Y. He, A. Kan, W. Yu, D. Wang, L. Zhang, G. Zhu, H. Xie, and X. She, "Significant photothermal conversion enhancement of nanofluids induced by rayleigh-bénard convection for direct absorption solar collectors", *Applied Energy*, vol. 254, 2019.

[30] H. Thon, "Photothermal boiling and characterization of nanofluids", Unpublished, Master's thesis, University of Bergen, 2019.

[31] E. Ulset, P. Kosinski, Y. Zabednova, O. Zhdaneev, P. Struchalin, and B. Balakin, "Photothermal boiling in aqueous nanofluids", *Nano Energy*, vol. 50, pp. 339–346, 2018.

[32] S. Siddiqui, P. Unwin, Z. Xu, and S. Kresta, "The effect of stabilizer addition and sonication on nanoparticle agglomeration in a confined impinging jet reactor", *Colloids and Surfaces A: Physicochemical and Engineering Aspects*, vol. 350, no. 1-3, pp. 38–50, 2009.

[33] N. Ali, J. A. Teixeira, and A. Addali, "A review on nanofluids: Fabrication, stability, and thermophysical properties", *Journal of Nanomaterials*, vol. 2018, 2018.

[34] R. Taylor, S. Coulombe, T. Otanicar, P. Phelan, A. Gunawan, W. Lv, G. Rosengarten, R. Prasher, and H. Tyagi, "Small particles, big impacts: A review of the diverse applications of nanofluids", *Journal of Applied Physics*, vol. 113, no. 1, p. 1, 2013.

[35] A. Elsheikh, S. Sharshir, M. Mostafa, F. Essa, and M. Ali, "Applications of nanofluids in solar energy: A review of recent advances", *Renewable and Sustainable Energy Reviews*, vol. 82, pp. 3483–3502, 2018.

[36] S. Ahmad, R. Saidur, I. Mahbubul, and F. Al-Sulaiman, "Optical properties of various nanofluids used in solar collector: A review", *Renewable and Sustainable Energy Reviews*, vol. 73, pp. 1014–1030, 2017.

[37] Encyclopedia, *Blackbody radiation*. [Online]. Available: `//www.encyclopedia.com/science/encyclopedias-almanacs-transcripts-and-maps/blackbody-radiation` (visited on 11/22/2019).

[38] G. Jia, H. Wang, L. Yan, X. Wang, R. Pei, T. Yan, Y. Zhao, and X. Guo, "Cytotoxicity of carbon nanomaterials: Single-wall nanotube, multi-wall nanotube, and fullerene", *Environmental Science & Technology*, vol. 39, no. 5, pp. 1378–1383, 2005.

[39] J. Muller, F. Huaux, N. Moreau, P. Misson, J. Heilier, M. Delos, M. Arras, A. Fonseca, J. Nagy, and D. Lison, "Respiratory toxicity of multi-wall carbon nanotubes", *Toxicology and Applied Pharmacology*, vol. 207, no. 3, pp. 221–231, 2005.

[40] S. Klaine, P. Alvarez, G. Batley, T. Fernandes, R. Handy, D. Lyon, S. Mahendra, M. McLaughlin, and J. Lead, "Nanomaterials in the environment: Behavior, fate, bioavailability, and effects", *Environmental Toxicology and Chemistry: An International Journal*, vol. 27, no. 9, pp. 1825–1851, 2008.

[41] J. Lead, G. Batley, P. Alvarez, M. Croteau, R. Handy, M. McLaughlin, J. Judy, and K. Schirmer, "Nanomaterials in the environment: Behavior, fate, bioavailability, and effects — an updated review", *Environmental Toxicology and Chemistry*, vol. 37, no. 8, pp. 2029–2063, 2018.

[42] J. Jeevanandam, A. Barhoum, Y. Chan, A. Dufresne, and M. Danquah, "Review on nanoparticles and nanostructured materials: History, sources, toxicity and regulations", *Beilstein Journal of Nanotechnology*, vol. 9, no. 1, pp. 1050–1074, 2018.

[43] W. Yu and H. Xie, "A review on nanofluids: Preparation, stability mechanisms, and applications", *Journal of Nanomaterials*, 2012.

[44] W. Chamsa-ard, S. Brundavanam, C. Fung, D. Fawcett, and G. Poinern, "Nanofluid types, their synthesis, properties and incorporation in direct solar thermal collectors: A review", *Nanomaterials*, vol. 7, no. 6, p. 131, 2017.

[45] A. Ghadimi, R. Saidur, and H. Metselaar, "A review of nanofluid stability properties and characterization in stationary conditions", *International Journal of Heat and Mass Transfer*, vol. 54, no. 17-18, pp. 4051–4068, 2011.

[46] J. Schwarzkopf, M. Sommerfeld, C. Crowe, and Y. Tsuji, *Multiphase Flows with Droplets and Particles*. CRC press, 2011.

[47] T. Cosgrove, *Colloid Science: Principles, Methods and Applications*. Blackwell Publishing Ltd, 2005. [Online]. Available: `https://ebookcentral.proquest.com/lib/bergen-ebooks/detail.action?docID=284152`.

[48] J. Berg, A. Romoser, N. Banerjee, R. Zebda, and C. Sayes, "The relationship between ph and zeta potential of 30 nm metal oxide nanoparticle suspensions relevant to in vitro toxicological evaluations", *Nanotoxicology*, vol. 3, no. 4, pp. 276–283, 2009.

[49] S. Mukherjee and S. Paria, "Preparation and stability of nanofluids - a review", *IOSR Journal of Mechanical and Civil Engineering*, vol. 9, no. 2, pp. 63–69, 2013.

[50] M. Ghassemi and A. Shahidian, *Nano and Bio Heat Transfer and Fluid Flow*. Academic Press, 2017.

[51] W. McCabe, J. Smith, and P. Harriott, *Unit Operations of Chemical Engineering*. McGraw-hill New York, 1993, vol. 1130.

[52] M. Ahmadi, A. Mirlohi, M. Nazari, and R. Ghasempour, "A review of thermal conductivity of various nanofluids", *Journal of Molecular Liquids*, vol. 265, pp. 181–188, 2018.

[53] S. Acharya, "Single-phase convective heat transfer: Basic equations and solutions", *Handbook of Thermal Science and Engineering*, pp. 363–390, 2018.

[54] M. Davidzon, "Newton's law of cooling and its interpretation", *International Journal of Heat and Mass Transfer*, vol. 55, no. 21-22, pp. 5397–5402, 2012.

[55] R. Saidur, K. Leong, and H. A. Mohammed, "A review on applications and challenges of nanofluids", *Renewable and Sustainable Energy Reviews*, vol. 15, no. 3, pp. 1646–1668, 2011.

[56] W. Ranz and W. Marshall, "Evaporation from drops", *Chemical Engineering Progress*, vol. 48, no. 3, pp. 141–146, 1952.

[57] Y. Cengel, *Heat and Mass Transfer: Fundamentals and Applications*. McGraw-Hill Higher Education, 2014.

[58] W. Commons, *Em spectrum*. [Online]. Available: `https://commons.wikimedia.org/wiki/File:EM_spectrum.svg` (visited on 05/04/2020).

[59] J. Howell, M. Menguc, and R. Siegel, *Thermal Radiation Heat Transfer*. CRC Press, 2015.

[60] D. Ganji, Y. Sabzehmeidani, and A. Sedighiamiri, *Nonlinear Systems in Heat Transfer: Mathematical Modeling and Analytical Methods*. Elsevier, 2017.

[61] J. Meyer, S. Adio, M. Sharifpur, and P. Nwosu, "The viscosity of nanofluids: A review of the theoretical, empirical, and numerical models", *Heat Transfer Engineering*, vol. 37, no. 5, pp. 387–421, 2016.

[62] K. Bashirnezhad, S. Bazri, M. Safaei, M. Goodarzi, M. Dahari, O. Mahian, A. Dalkılıça, and S. Wongwises, "Viscosity of nanofluids: A review of recent experimental studies", *International Communications in Heat and Mass Transfer*, vol. 73, pp. 114–123, 2016.

[63] A. Einstein, "Eine neue bestimmung der moleküldimensionen", *Annalen der Physik*, vol. 324, no. 2, pp. 289–306, 1906.

[64] H. Brinkman, "The viscosity of concentrated suspensions and solutions", *The Journal of Chemical Physics*, vol. 20, no. 4, pp. 571–571, 1952.

[65] G. Batchelor, "The effect of brownian motion on the bulk stress in a suspension of spherical particles", *Journal of Fluid Mechanics*, vol. 83, no. 1, pp. 97–117, 1977.

[66] N. Masoumi, N. Sohrabi, and A. Behzadmehr, "A new model for calculating the effective viscosity of nanofluids", *Journal of Physics D: Applied Physics*, vol. 42, no. 5, p. 055 501, 2009.

[67] D. Udawattha, M. Narayana, and U. Wijayarathne, "Predicting the effective viscosity of nanofluids based on the rheology of suspensions of solid particles", *Journal of King Saud University-Science*, vol. 31, no. 3, pp. 412–426, 2019.

[68] M. Tasumi, *Introduction to Experimental Infrared Spectroscopy: Fundamentals and Practical Methods*. John Wiley & Sons, 2014.

[69] O. Mahian, A. Kianifar, C. Kleinstreuer, M. Al-Nimr, I. Pop, A. Z. Sahin, and S. Wongwises, "A review of entropy generation in nanofluid flow", *International Journal of Heat and Mass Transfer*, vol. 65, pp. 514–532, 2013.

[70] K. Khanafer and K. Vafai, "A critical synthesis of thermophysical characteristics of nanofluids", *International Journal of Heat and Mass Transfer*, vol. 54, no. 19-20, pp. 4410–4428, 2011.

[71] P. Struchalin, Private Communication, Mar. 12, 2020.
[72] M. Karami, M. Akhavan-Bahabadi, S. Delfani, and M. Raisee, "Experimental investigation of cuo nanofluid-based direct absorption solar collector for residential applications", *Renewable and Sustainable Energy Reviews*, vol. 52, pp. 793–801, 2015.
[73] M. Chen, Y. He, J. Zhu, and D. Wen, "Investigating the collector efficiency of silver nanofluids based direct absorption solar collectors", *Applied Energy*, vol. 181, pp. 65–74, 2016.
[74] H. Gupta, G. Agrawal, and J. Mathur, "An experimental investigation of a low temperature al2o3-h2o nanofluid based direct absorption solar collector", *Solar Energy*, vol. 118, pp. 390–396, 2015.
[75] J. Liu, Z. Ye, L. Zhang, X. Fang, and Z. Zhang, "A combined numerical and experimental study on graphene/ionic liquid nanofluid based direct absorption solar collector", *Solar Energy Materials and Solar Cells*, vol. 136, pp. 177–186, 2015.
[76] M. Prieto, N. Solomakhina, and P. de Uribarri, "Multimodal networks and decentralized renewable generation: Network modeling and energy/exergy performance evaluation", in *Urban Energy Systems for Low-Carbon Cities*, Elsevier, 2019, pp. 181–239.
[77] C. Hindle, *Polypropylene (pp)*. [Online]. Available: `https://www.bpf.co.uk/plastipedia/polymers/pp.aspx` (visited on 03/08/2020).
[78] E. T. Ulset, "Utilizing solar vapor energy by use of nanofluids in a direct solar collector", Master's thesis, University of Bergen, Jan. 2018.
[79] J. Bentley, *Principles of Measurement Systems*. Pearson Education, 2005.
[80] S. X. R. I. C. Ltd, *King water pump instructions*. [Online]. Available: `//www.resun-china.com/en/product/detail/id-850.html` (visited on 06/28/2019).
[81] B. Balakin, Private Communication, May 26, 2020.
[82] P. Technology, *Pt-104 platinum resistance data logger*. [Online]. Available: `https://www.picotech.com/download/datasheets/pt-104-prt-data-logger-data-sheet.pdf` (visited on 03/10/2020).
[83] ——, *Pt100 probe specifications*. [Online]. Available: `https://www.picotech.com/accessories/pt100-sensors/pt100-tenth-din-2m` (visited on 03/22/2020).
[84] N. I. of Standards and Technology, *Ice point calibration*, 2014. [Online]. Available: `https://www.youtube.com/watch?v=KYOJayWqB3g` (visited on 03/15/2020).
[85] M. S. L. of New Zealand, *Msl technical guide 1 - the ice point*, 2019. [Online]. Available: `https://www.measurement.govt.nz/resources/#collapse-control-1-4` (visited on 03/15/2020).
[86] Osram. (). Haloline pro 400 w 230 v r7s, [Online]. Available: `https://www.osram.no/ecat/HALOLINE%20PRO-HALOLINE-Halogenlamper-Lamper-Digital%20Systems/no/no/GPS01_1027717/PP_EUROPE_NO_eCat/ZMP_83732/` (visited on 04/11/2020).
[87] S. L. T. C. Ltd, *Ir power meter user manual*. [Online]. Available: `//www.lsmeter.com/product/Proupload.ashx?id=98` (visited on 06/28/2019).
[88] Limit, *Digital level 150*. [Online]. Available: `https://limit-tools.com/product/digital-level-150/` (visited on 04/10/2020).

[89] Y. Gan and L. Qiao, "Optical properties and radiation-enhanced evaporation of nanofluid fuels containing carbon-based nanostructures", *Energy & Fuels*, vol. 26, no. 7, pp. 4224–4230, 2012.

[90] A. Zeiny, H. Jin, L. Bai, G. Lin, and D. Wen, "A comparative study of direct absorption nanofluids for solar thermal applications", *Solar Energy*, vol. 161, pp. 74–82, 2018.

[91] B. Balakin, Private Communication, Mar. 26, 2020.

[92] Y. Hwang, J. Lee, J. Lee, Y. Jeong, S. Cheong, Y. Ahn, and S. Kim, "Production and dispersion stability of nanoparticles in nanofluids", *Powder Technology*, vol. 186, no. 2, pp. 145–153, 2008.

[93] Kärcher, *Foamstop neutral*. [Online]. Available: `https://www.kaercher.com/int/home-garden/cleaning-and-care-agents/home-garden/vacuum-cleaner-with-water-filter-steam-vacuum-cleaner/foamstop/foamstop-neutral-62958730.html` (visited on 06/14/2020).

[94] S. Chakraborty and P. Panigrahi, "Stability of nanofluid: A review", *Applied Thermal Engineering*, p. 115 259, 2020.

[95] S. Lo and D. Zhang, "Modelling of break-up and coalescence in bubbly two-phase flows", *The Journal of Computational Multiphase Flows*, vol. 1, no. 1, pp. 23–38, 2009.

[96] L. Zhou, Y. Wang, and Q. Huang, "Parametric analysis on the performance of flat plate collector with transparent insulation material", *Energy*, pp. 534–542, 2019.

[97] Y. Sekhar, K. Sharma, and M. Rao, "Evaluation of heat loss coefficients in solar flat plate collectors", *ARPN Journal of Engineering and Applied Sciences*, vol. 4, no. 5, pp. 15–19, 2009.

[98] S. P. Forschung, *Collector no. c880 informal result sheet for short test*. [Online]. Available: `http://www.npomash.ru/service/en/suncollector.htm` (visited on 06/28/2019).

[99] S. Delfani, M. Karami, and M. Akhavan-Behabadi, "Performance characteristics of a residential-type direct absorption solar collector using mwcnt nanofluid", *Renewable Energy*, vol. 87, pp. 754–764, 2016.

[100] S. Sharma and S. Gupta, "Preparation and evaluation of stable nanofluids for heat transfer application: A review", *Experimental Thermal and Fluid Science*, vol. 79, pp. 202–212, 2016.

[101] S. Aldrich, "Antifoam b emulsion", [Online]. Available: `https://www.sigmaaldrich.com/catalog/product/sigma/a5757?lang=en&region=NO` (visited on 06/22/2020).

[102] B. V. KF, *Quality of water delivered from the svartediket water treatment plant in 2019*. [Online]. Available: `https://d1pk8xkmonbx0b.cloudfront.net/1583145798/svartediket-2019-hjemmeside.pdf` (visited on 03/10/2020).

Appendices

Appendix A

Uncertainty calculations

The effects that give rise to uncertainty in measurements can be either random or systematic. Random uncertainty is statistical fluctuations in the measured data. Truly random fluctuations average to zero, thus averaging over a large number of measurements is a very effective way of diminishing this type of uncertainty. Systematic uncertainty, however, is inaccuracies that affect the results for repeated measurements, often caused by the instrument or some other type of repeated bias. Calibration standards for instruments are an example of a preventative action to avoid systematic uncertainty.

The major components to the total uncertainty in experimental collector efficiency for this study are the inaccuracy in flow rate measurement, temperature measurement, and solar radiation intensity measurement. All the relevant instrumental uncertainties can be found in Table 3.2, Chapter 3. The following equations were used for uncertainty calculations:

Mean value

The mean value is defined as the sum of all the values divided by the total number of values in a given set. It is also known as the average. The mean value, $\bar{x}$, can be calculated by the following equation:

$$\bar{x} = \frac{x_1 + x_2 + x_3 + ... + x_N}{N} = \frac{1}{N}\sum_{i=1}^{N} x_i, \tag{A.1}$$

where N is the number of values in a data set.

Sample standard deviation

Standard deviation characterises the scatter, or spread, of values in a data set. The sample standard deviation can be calculated by the following equation:

$$S = \sqrt{\frac{1}{N-1}\sum_{i=1}^{N}(x_i - \bar{x})^2}, \tag{A.2}$$

where N is the number of values in a data set (repeated readings).

Standard uncertainty of the mean

The standard deviation S, defined by Equation A.2, provides the random uncertainty estimate for any one of the measurements used to compute S. Intuitively the mean value of the measurements is expected to provide less random uncertainty than any one of the individual measurements. The standard deviation of the mean value (or standard uncertainty of the mean), σ_m, of a data set when all measurements have equal statistical weight, is given by:

$$\sigma_m = \frac{S}{\sqrt{N}} \tag{A.3}$$

Propagation of uncertainties

If the quantity of an experimental result f is calculated by independent variables x, y, z..., i, with corresponding uncertainties S_x, S_y, S_z, ... , S_i, the propagation of the uncertainties yields:

$$S_f = \sqrt{(\frac{\delta f}{\delta x}S_x)^2 + (\frac{\delta f}{\delta y}S_y)^2 + (\frac{\delta f}{\delta z}S_z)^2 + ... + (\frac{\delta f}{\delta i}S_i)^2}, \tag{A.4}$$

where S_f is the uncertainty of the result f, and S_i is the standard uncertainty on the independent quantities i.

All contributing uncertainties should be expressed at the same confidence level by converting them into standard uncertainties. A standard uncertainty is a margin whose size can be thought of as 'plus or minus one standard deviation'. The standard uncertainty tells us about the uncertainty of an average (not just about the spread of values).

Appendix B

Tap water reference data

Tap water quality in Bergen from Bergen Vann KF [102]:

Kvalitet på vann levert fra Svartediket vannbehandlingsanlegg i 2019

Ukentlig analyserte parametre er oppsummert i tabell 1, mer sjeldne i tabell 2

Svartediket forsyner normalt sett til Bergen sentrum
Det forsyner også vestre deler av Bergen sammen med Espeland,
og områdene Kokstad, Hjellestad/Milde og Skjold/Nordås sammen med Kismul og Espeland.

Tabell 1
Analyseresultat fra rentvann ved Svartediket vannbehandlingsanlegg i perioden 1.1.2019 – 31.12.2019
Analysene er utført ved Bergen Vann sitt Vannlaboratorium
**** akseptabel for abonnentene/ ingen unormal endring***
() angir anbefalt nivå, ingen krav i drikkevannsforskriften

Parameter	Enhet	Snitt	Maks	Min	Antall	Drikkevannsforskriftens grenseverdi
Surhet	pH	8,2	8,3	8,0	51	6,5-9,5
Konduktivitet	mS/m	11,3	12,7	10,3	50	250
Turbiditet	FNU	0,1	0,5	0,1	52	(1)*
Fargetall	mg/l Pt	2,3	4,0	2,0	49	(20)*
UV-transmisjon	%	85,3	91,4	78,7	50	
Kalsium	mg/l Ca	17,7	24,0	13,0	49	(15-25)
Alkalitet	mmol/l	0,7	0,9	0,6	48	(0,6-1,0)
Lukt	0-4	0,0	0,0	0,0	49	*
Smak	0-4	0,0	0,0	0,0	49	*
Kimtall 22 °C	ant/ml	7,7	300**	0,0	47	100
Clostridium perfringens	ant/100ml	0	0	0	2	0
Koliforme	ant/100ml	0	0	0	52	0
E. coli	ant/100ml	0	0	0	52	0
Intestinale enterokokker	ant/100ml	0	0	0	50	0

** Kimtallet overskred grensen i drikkevannsforskriften ved en anledning. Samtlige andre parametre viste normale verdier. Dette er en driftsparameter som ikke har helsemessig betydning.

Ofte stilte spørsmål:

Hardhet på vannet:
Kalsiuminnholdet i vannet fra Svartediket hadde i 2019 et gjennomsnittlig innhold på 17,7 mg/l.
Omregnet til tyske hardhetsgrader tilsvarer dette 2 dH°.
Magnesiuminnholdet er svært lavt. Det stilles ikke krav til denne parameteren og det måles ikke rutinemessig.
En sjekk av magnesiuminnholdet i 1994 viste konsentrasjoner under 1 mg/l.

Klor:
Det brukes ikke klor ved vannbehandlingen fra Svartediket vannbehandlingsanlegg.
Kun i meget spesielle situasjoner vil vannet bli klorert.

Innhold av bikarbonat:
Det måles ikke direkte på bikarbonat, men man kan regne på teoretiske verdier. Vi antar at all karbonat foreligger på formen bikarbonat, HCO^-, og at det kun er karbonatsystemet som gir vannet buffer/alkalitet.
Innholdet av bikarbonat vil da være proposjonalt med alkaliteten som måles.
Med en molvekt på 61 g/mol (mg/mmol) gir dette følgende innhold av HCO_3^- i vannet:
Målt alkalitet 0,7 mmol/l * 61 mg/mmol = 43 mg/l HCO_3^-
I virkeligheten foreligger ikke all alkalitet som HCO_3^-, noe foreligger også som CO_3^-, men dette er marginalt.
Det kan også være andre buffersystemer som gir alkalitet, men disse pleier å gi lite bidrag.

Appendix C

Temperature history plots for surface collector experiments

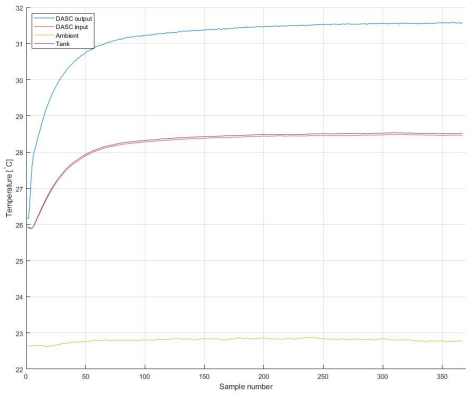

(a) $Q = 0.48$ L/min

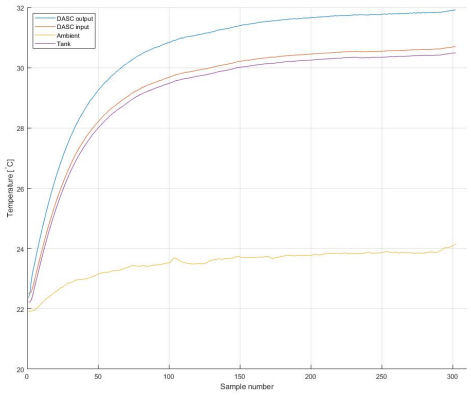

(b) $Q = 1.15$ L/min

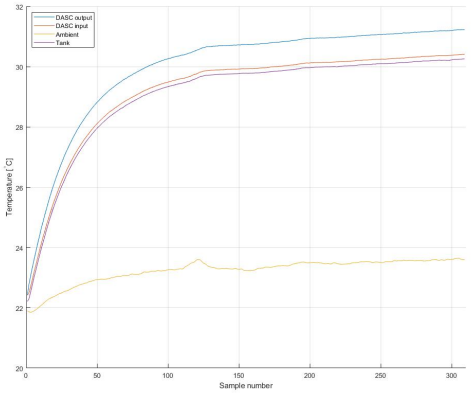

(c) $Q = 1.66$ L/min

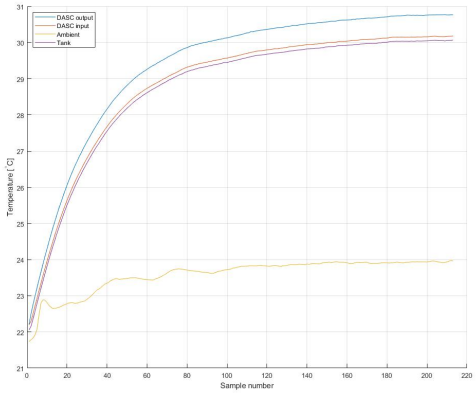

(d) $Q = 2.3$ L/min

Figure C.1: Temperature history plot for surface collector with 0° tilt angle.

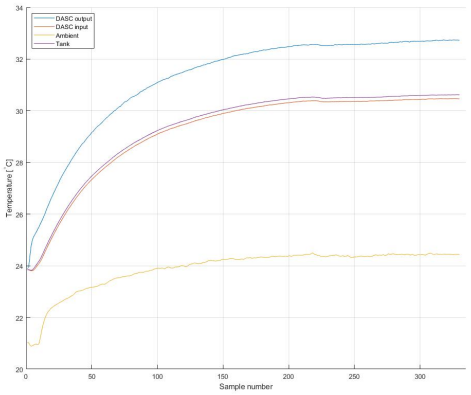

(a) $Q = 0.48$ L/min

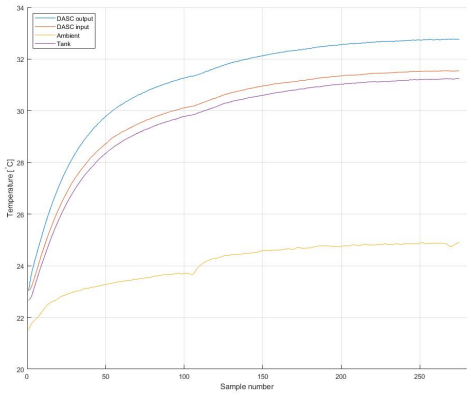

(b) $Q = 1.15$ L/min

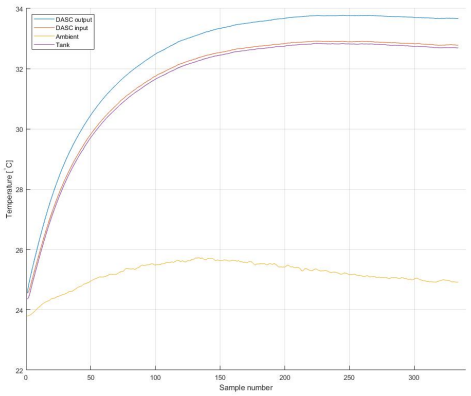

(c) $Q = 1.66$ L/min

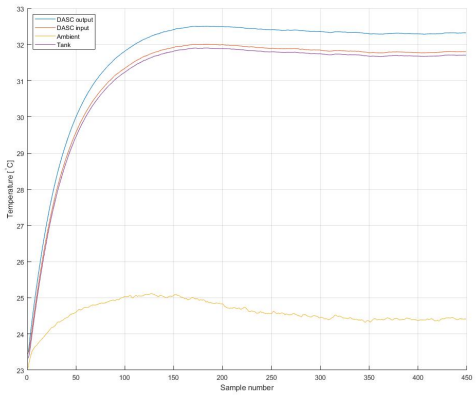

(d) $Q = 2.3$ L/min

Figure C.2: Temperature history plot for surface collector with 15° tilt angle.

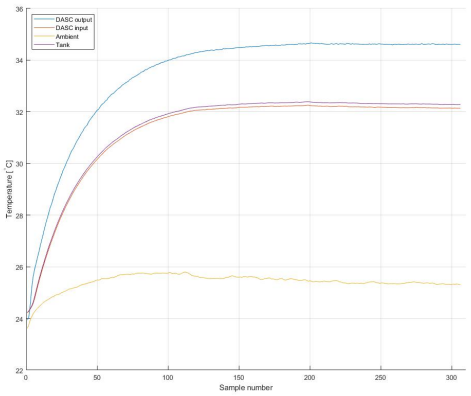

(a) $Q = 0.48$ L/min

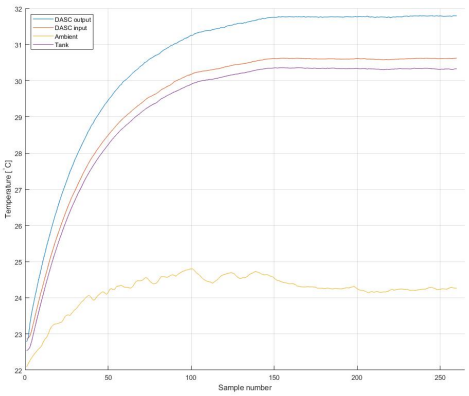

(b) $Q = 1.15$ L/min

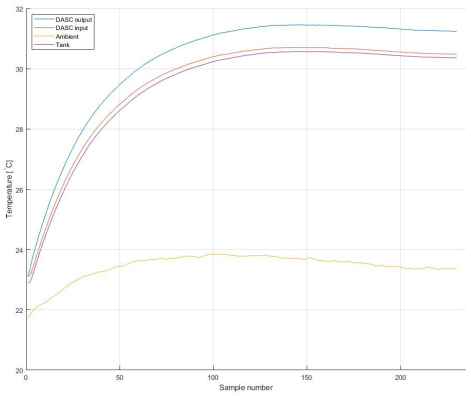

(c) $Q = 1.66$ L/min

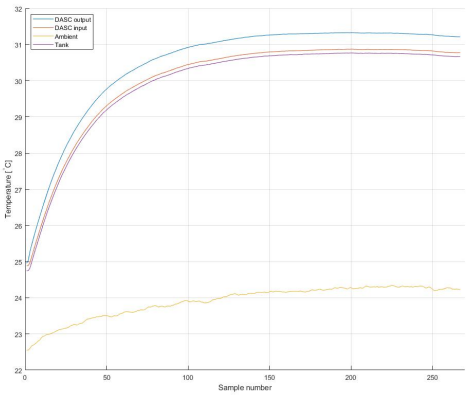

(d) $Q = 2.3$ L/min

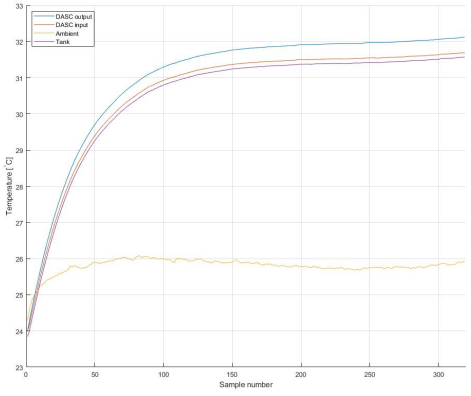

(e) $Q = 2.3$ L/min

Figure C.3: Temperature history plot for surface collector with 45° tilt angle.

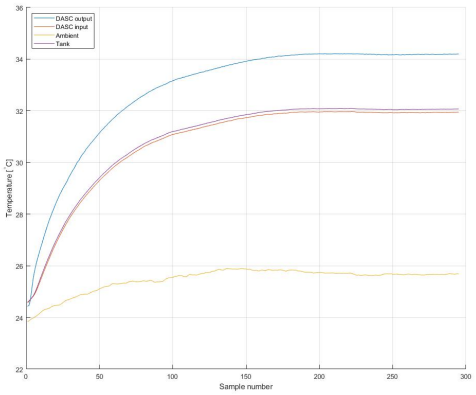

(a) $Q = 0.48$ L/min

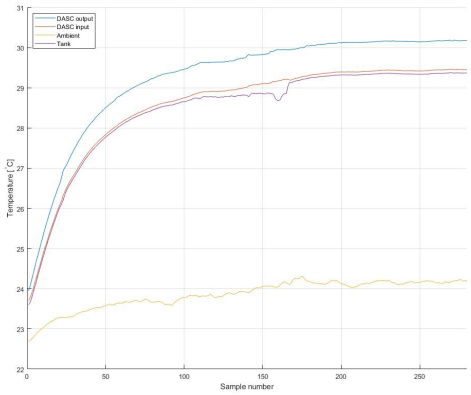

(b) $Q = 1.66$ L/min

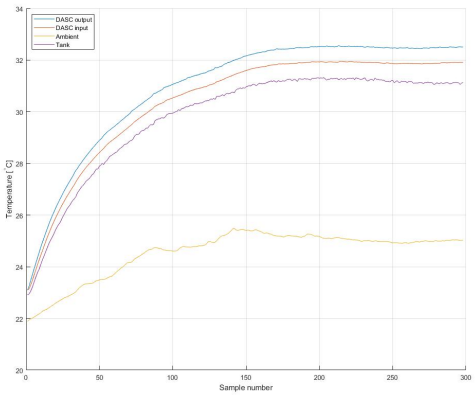

(c) $Q = 2.07$ L/min

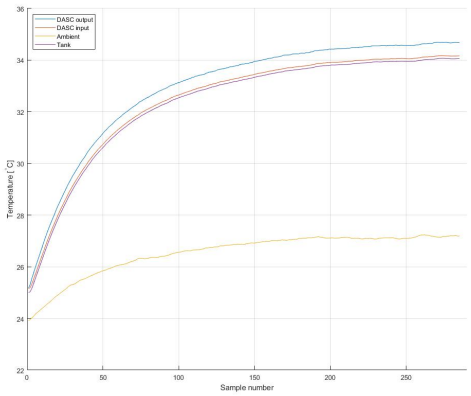

(d) $Q = 2.3$ L/min

Figure C.4: Temperature history plot for surface collector with 180° tilt angle.

Appendix D

Temperature history plots for water DASC experiments

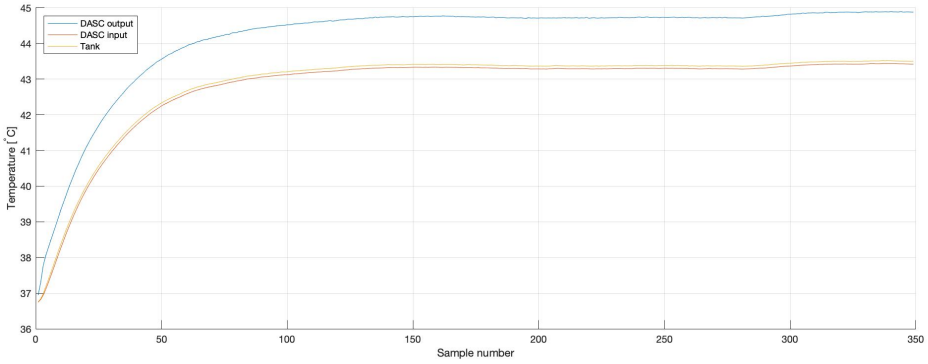

Figure D.1: Temperature history plot for water DASC with 0° tilt angle and $Q = 1.0$ L/min.

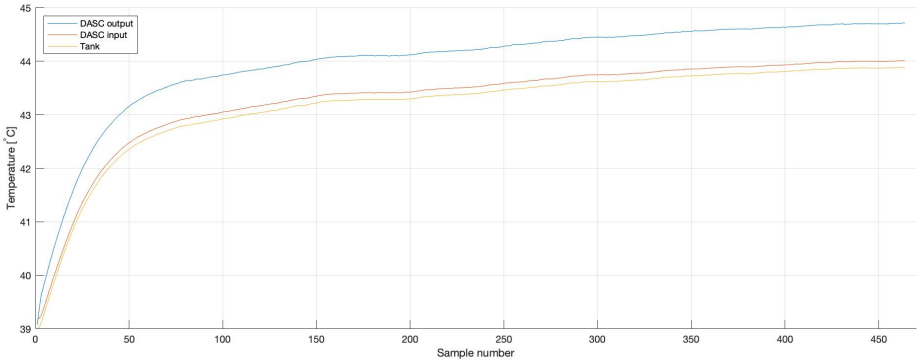

Figure D.2: Temperature history plot for water DASC with 0° tilt angle and $Q = 2.0$ L/min.

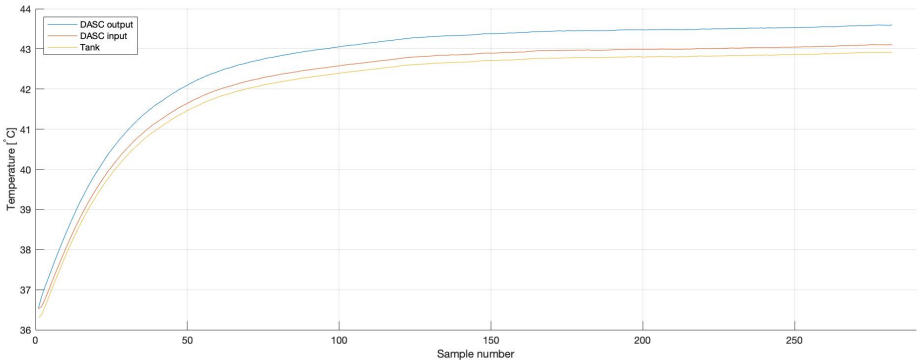

Figure D.3: Temperature history plot for water DASC with 0° tilt angle and $Q = 3.0$ L/min.

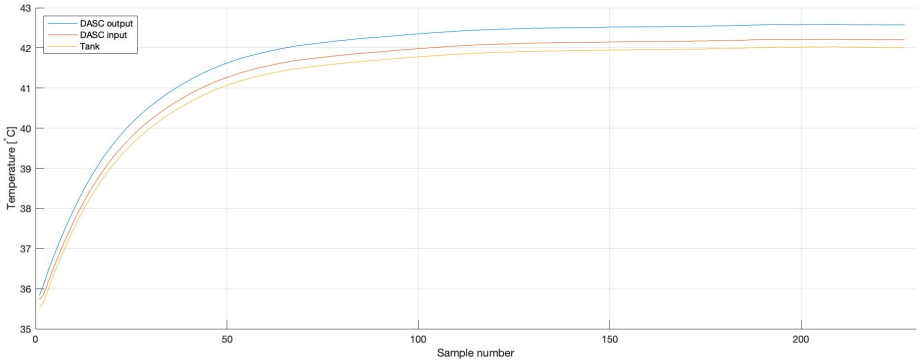

Figure D.4: Temperature history plot for water DASC with 0° tilt angle and $Q = 4.0$ L/min.

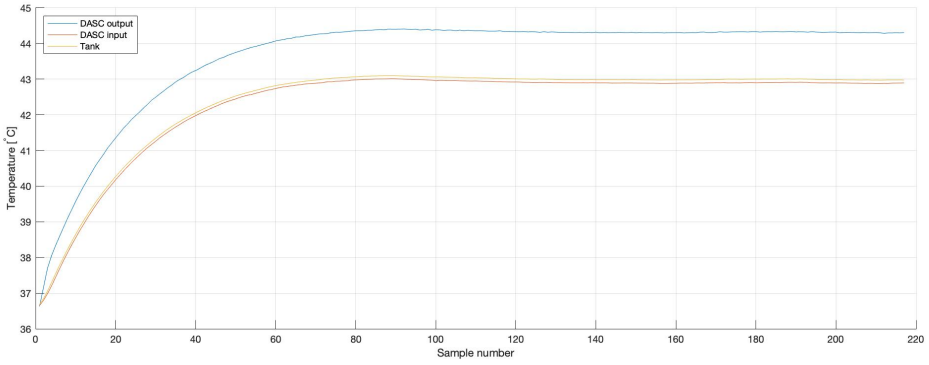

Figure D.5: Temperature history plot for water DASC with 15° tilt angle and $Q = 1.0$ L/min.

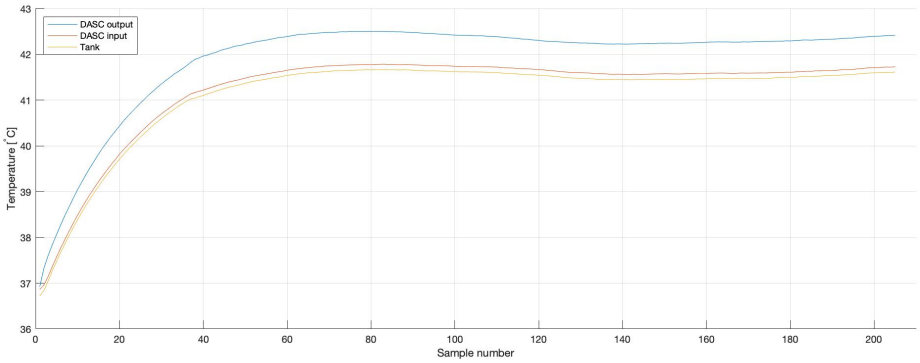

Figure D.6: Temperature history plot for water DASC with 15° tilt angle and $Q = 2.0$ L/min.

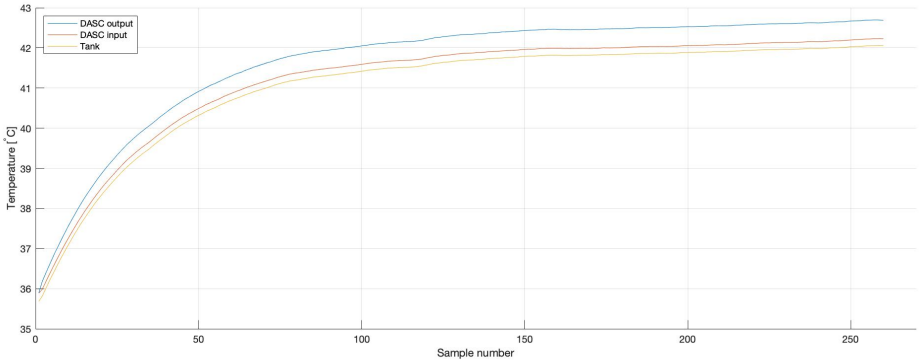

Figure D.7: Temperature history plot for water DASC with 15° tilt angle and $Q = 3.0$ L/min.

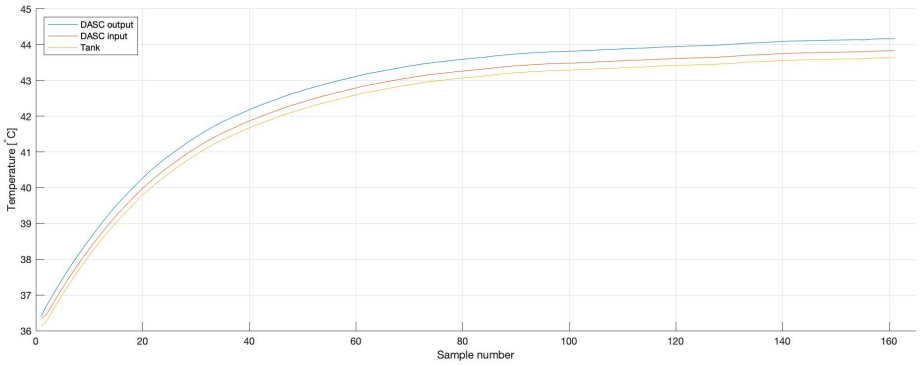

Figure D.8: Temperature history plot for water DASC with 15° tilt angle and $Q = 4.0$ L/min.

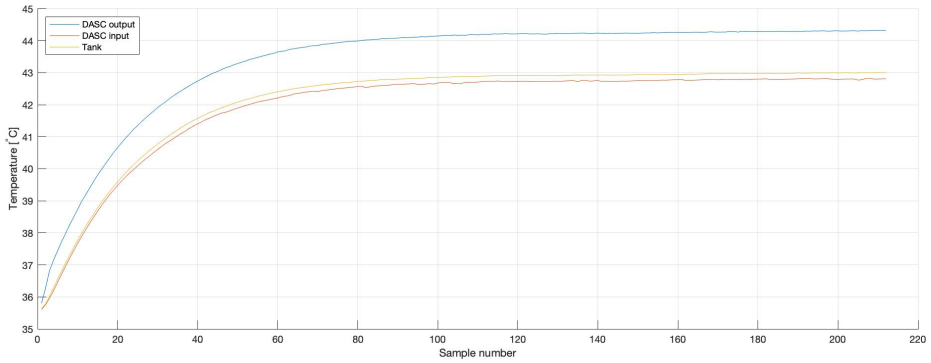

Figure D.9: Temperature history plot for water DASC with 45° tilt angle and $Q = 1.0$ L/min.

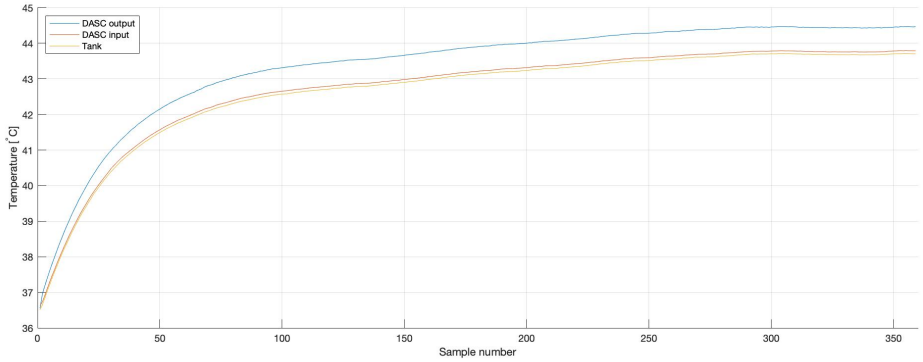

Figure D.10: Temperature history plot for water DASC with 45° tilt angle and $Q = 2.0$ L/min.

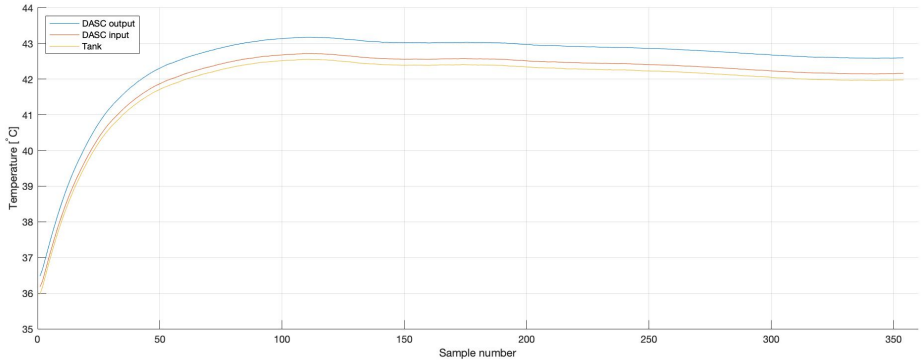

Figure D.11: Temperature history plot for water DASC with 45° tilt angle and $Q = 3.0$ L/min.

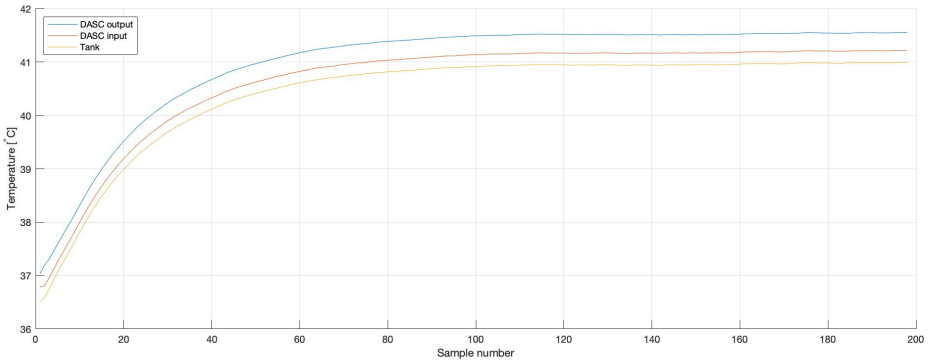

Figure D.12: Temperature history plot for water DASC with 45° tilt angle and $Q = 4.0$ L/min.

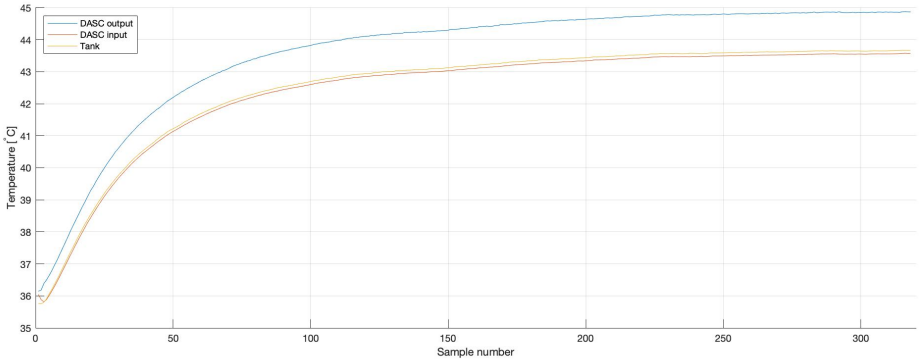

Figure D.13: Temperature history plot for water DASC with 180° tilt angle and $Q = 1.0$ L/min.

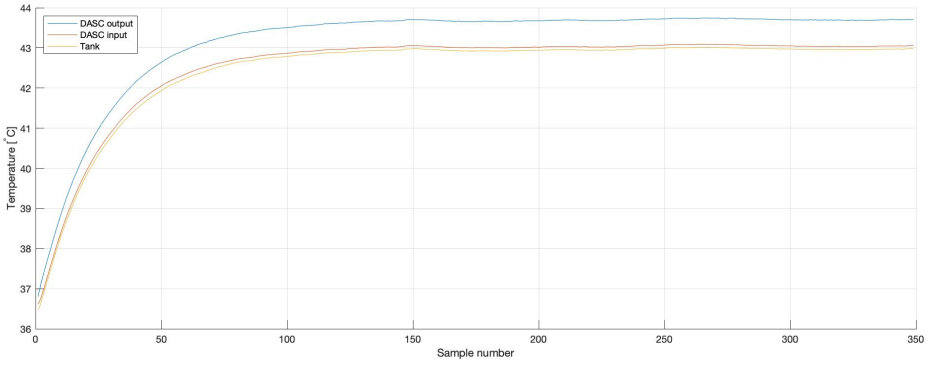

Figure D.14: Temperature history plot for water DASC with 180° tilt angle and $Q = 2.0$ L/min.

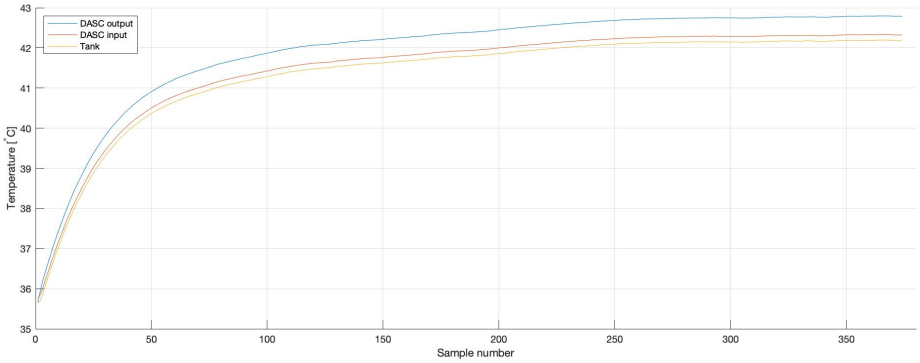

Figure D.15: Temperature history plot for water DASC with 180° tilt angle and $Q = 3.0$ L/min.

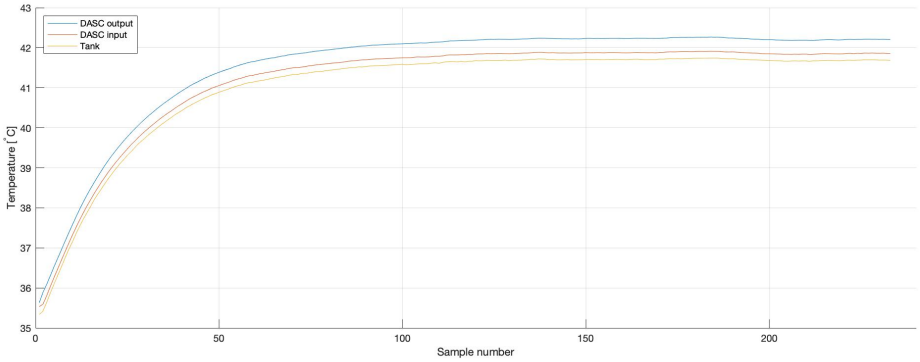

Figure D.16: Temperature history plot for water DASC with 180° tilt angle and $Q = 4.0$ L/min.

Appendix E

Temperature history plots for nanofluid DASC experiments

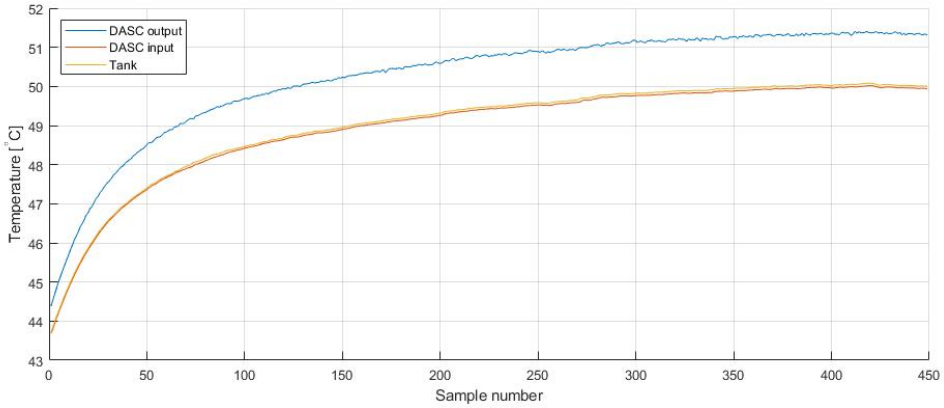

Figure E.1: Temperature history plot for NF DASC with 0° tilt angle and $Q = 1.0$ L/min.

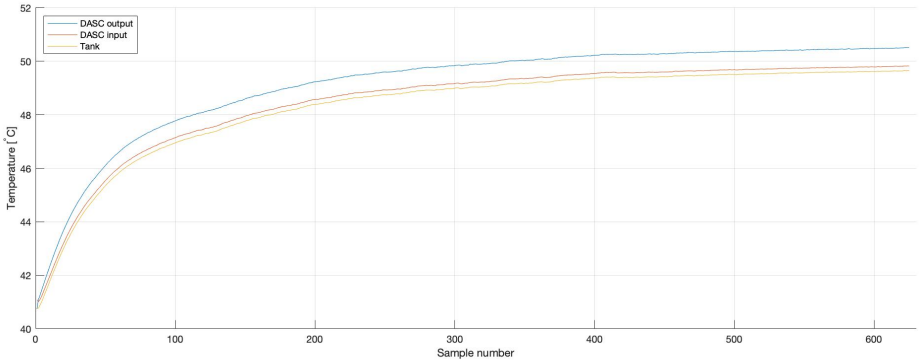

Figure E.2: Temperature history plot for NF DASC with 0° tilt angle and $Q = 2.0$ L/min.

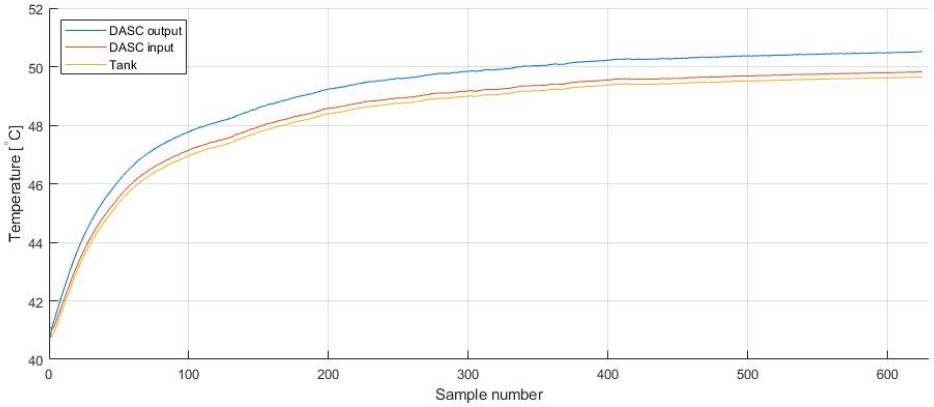

Figure E.3: Temperature history plot for NF DASC with 0° tilt angle and $Q = 3.0$ L/min.

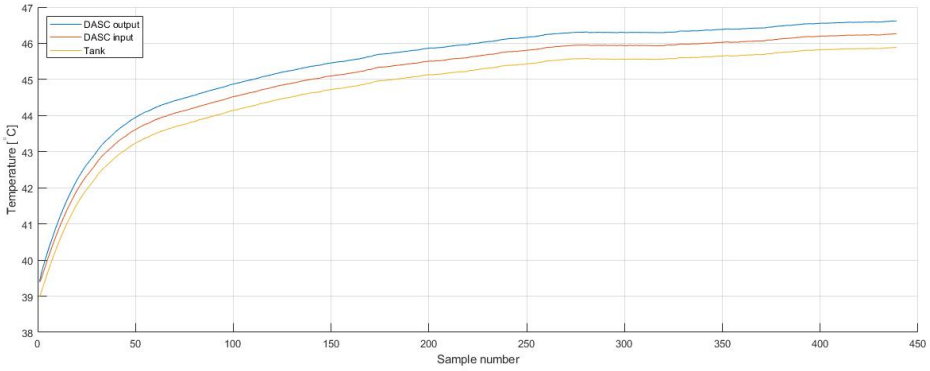

Figure E.4: Temperature history plot for NF DASC with 0° tilt angle and $Q = 4.0$ L/min.

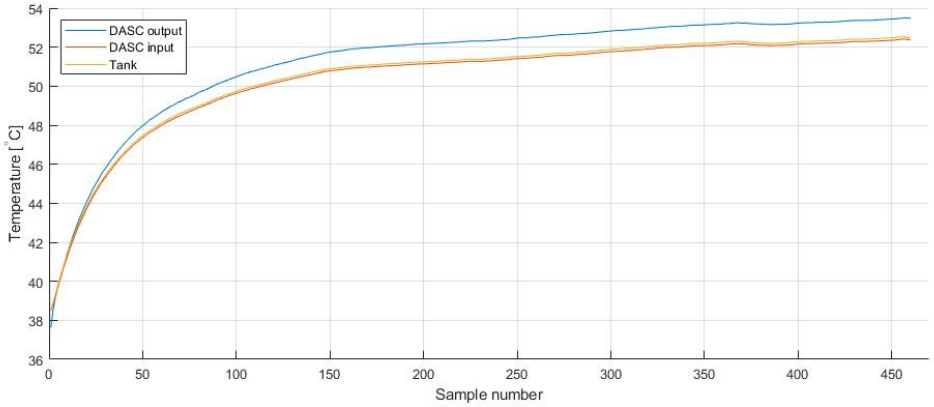

Figure E.5: Temperature history plot for NF DASC with 15° tilt angle and $Q = 1.0$ L/min.

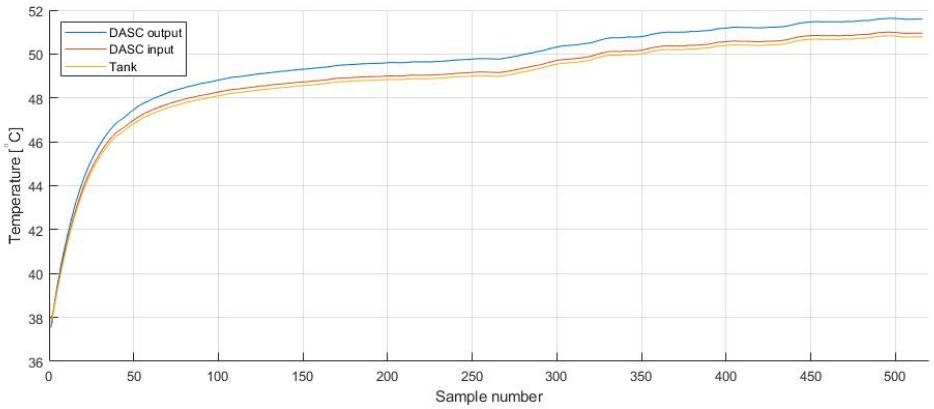

Figure E.6: Temperature history plot for NF DASC with 15° tilt angle and $Q = 2.0$ L/min.

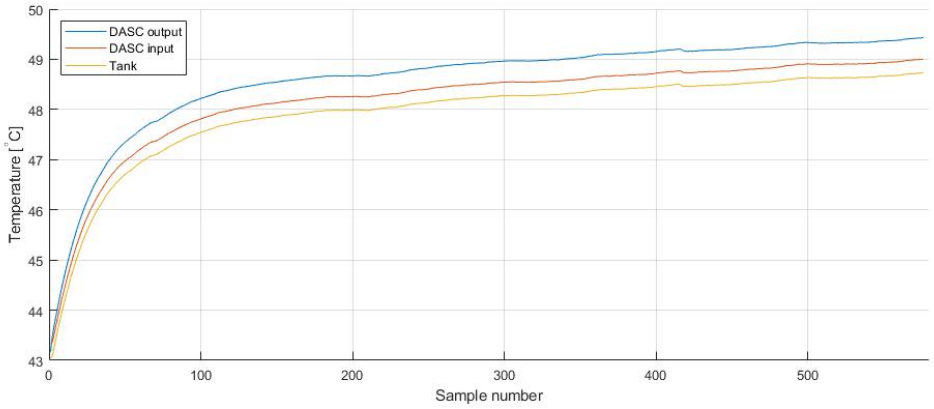

Figure E.7: Temperature history plot for NF DASC with 15° tilt angle and $Q = 3.0$ L/min.

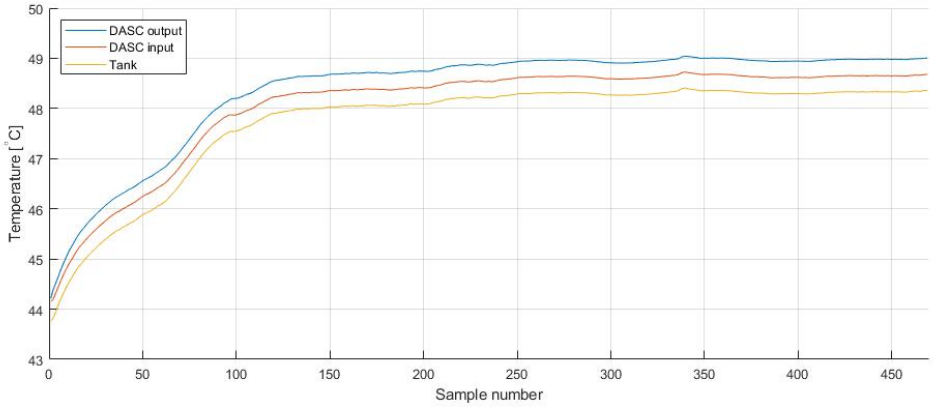

Figure E.8: Temperature history plot for NF DASC with 15° tilt angle and $Q = 4.0$ L/min.

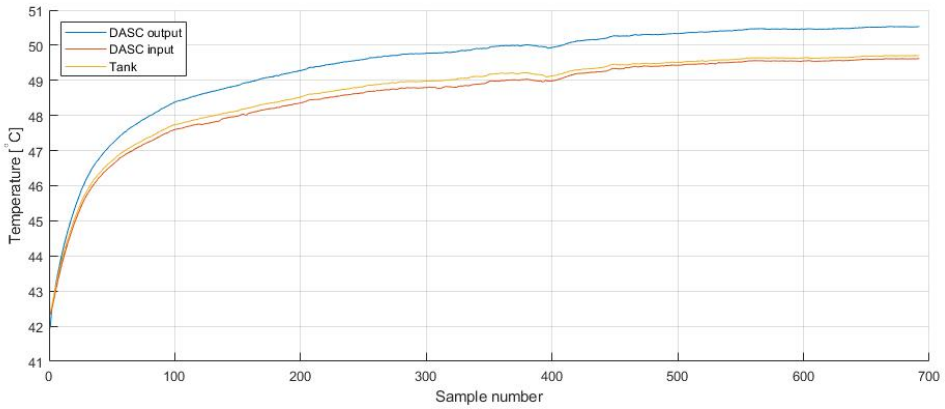

Figure E.9: Temperature history plot for NF DASC with 45° tilt angle and $Q = 1.0$ L/min.

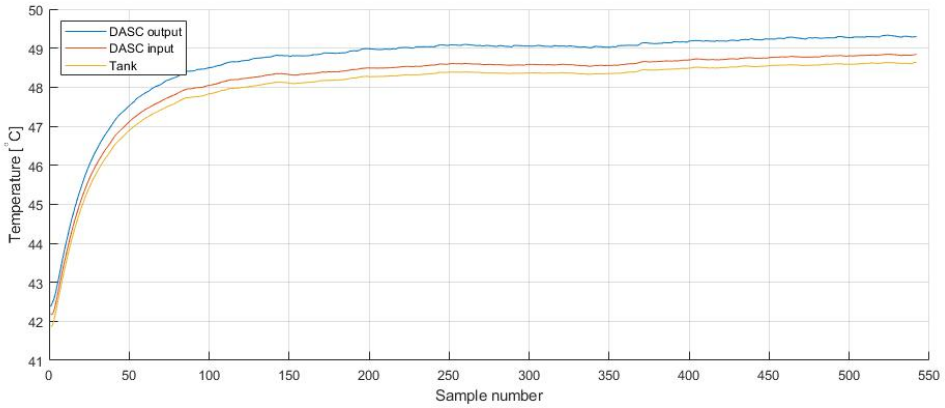

Figure E.10: Temperature history plot for NF DASC with 45° tilt angle and $Q = 2.0$ L/min.

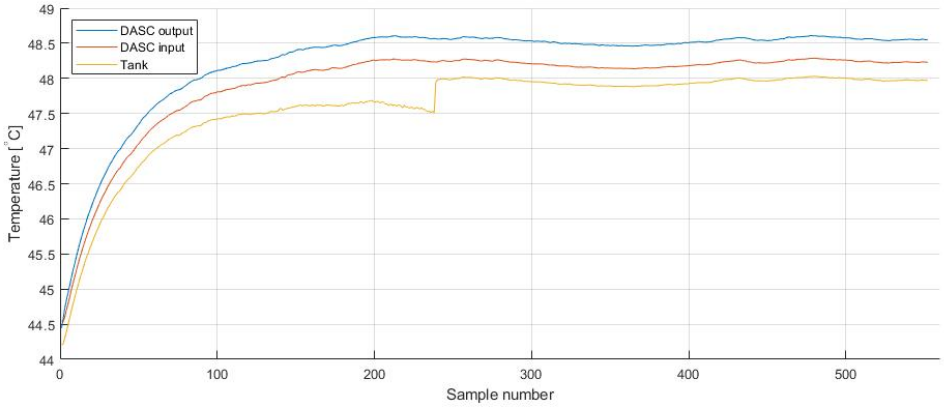

Figure E.11: Temperature history plot for NF DASC with 45° tilt angle and $Q = 3.0$ L/min.

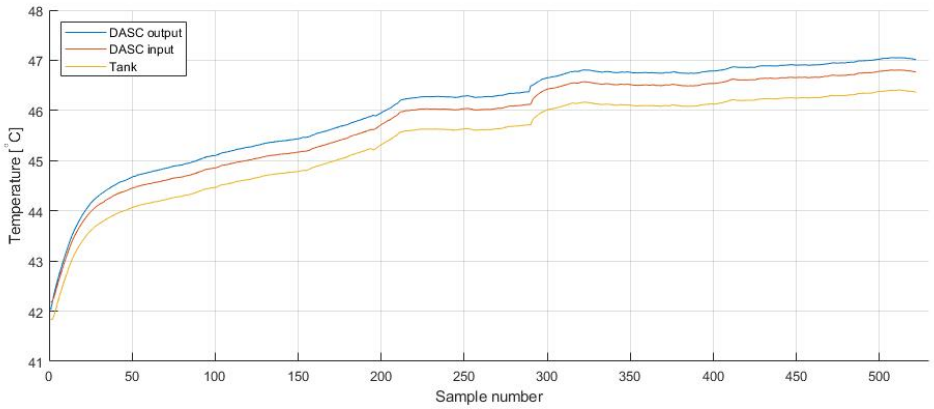

Figure E.12: Temperature history plot for NF DASC with 45° tilt angle and $Q = 4.0$ L/min.

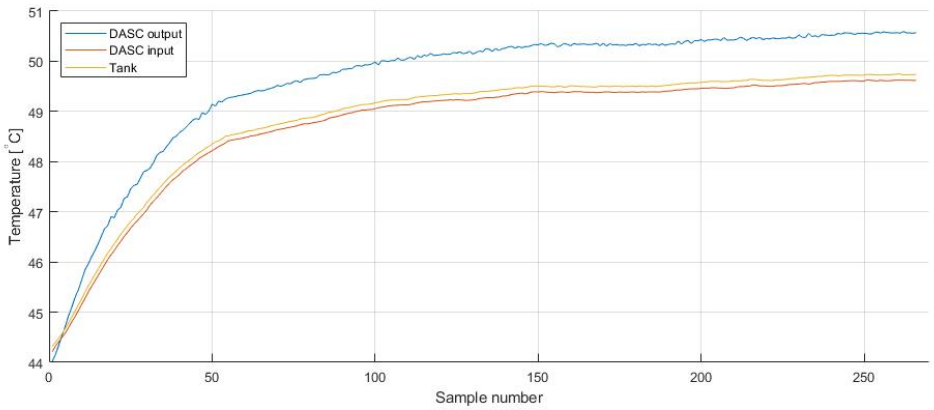

Figure E.13: Temperature history plot for NF DASC with 180° tilt angle and $Q = 1.0$ L/min.

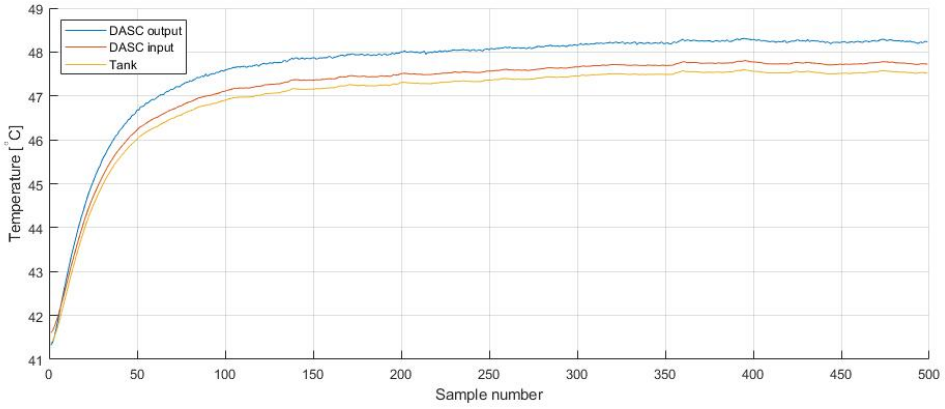

Figure E.14: Temperature history plot for NF DASC with 180° tilt angle and $Q = 2.0$ L/min.

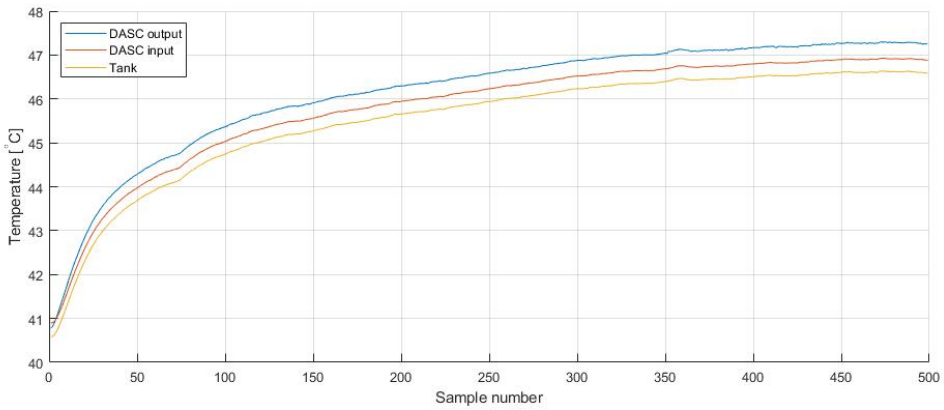

Figure E.15: Temperature history plot for NF DASC with 180° tilt angle and $Q = 3.0$ L/min.